Stony Brook University

Heavy Quarks and Interjet Radiation

A Dissertation Presented

by

Ilmo Sung

to

The Graduate School

in Partial Fulfillment of the Requirements

for the Degree of

Doctor of Philosophy

in

Physics

Stony Brook University

May 2010

Stony Brook University

The Graduate School

Ilmo Sung

We, the dissertation committee for the above candidate for the Doctor of Philosophy degree, hereby recommend acceptance of this dissertation.

George Sterman - Advisor
Distinguished Professor, Department of Physics and Astronomy

Robert Shrock - Committee Chair
Professor, Department of Physics and Astronomy

Xu Du
Assistant Professor, Department of Physics and Astronomy

Hooman Davoudiasl
Associate Physicist, the Physics Department,
Brookhaven National Laboratory

This dissertation is accepted by the Graduate School

Lawrence Martin
Dean of the Graduate School

Abstract of the Dissertation

Heavy Quarks and Interjet Radiation

by

Ilmo Sung

Doctor of Philosophy

in

Physics

Stony Brook University

2010

In the first part of this thesis, we show how properties of Quantum Chromodynamics (QCD) can be used directly or indirectly to discover physics beyond the standard model (BSM) in collider experiments. We introduce new methods to determine the color SU(3) gauge content of BSM resonances from new physics signals by investigating the pattern of soft gluon radiation into specified regions of a detector. We use energy flow, treated by perturbative QCD and factorization, as a tool to analyze properties of new physics. This approach allows the analytical prediction of the distribution of soft gluon radiation into a rapidity region of a detector, reflecting the standard model gauge content of heavy resonances. The results, in general, predict more radiation for singlet than for octet resonances. Especially, for spin-1 resonance production, we show a quite large difference in radiation into a rapidity gap region from color singlet and octet resonances. We also introduce the use of the collinear enhancement in perturbative QCD amplitudes to

distinguish products of highly-boosted massive particle decay from QCD jets whose collinear structure is described by a factorized jet function. At the LHC, events with highly-boosted massive particles such as top, W, Z and Higgs may be a key ingredient for the discovery of new physics. In many decay channels, these particles would be identified as high-p_t jets, and any such signal of definite mass must be disentangled from a large background of QCD jets. We discover that this background far exceeds such signals, and relying solely on jet mass as a way to reject QCD background from signal would probably not suffice in most case. To solve this problem, we find that jets from QCD are characterized by different patterns of intrajet energy flow compared to highly-boosted heavy particle decays. Based on this observation, we introduce several event shapes that could be used to disentangle signals from backgrounds. In the second part of this thesis, we study two-loop anomalous dimension matrices in QCD and related gauge theories for products of Wilson lines coupled at a point. We verify by an analysis in Euclidean space that the contributions to these matrices from diagrams that link three massive Wilson lines do not vanish in general. This differs from the pattern found with massless external lines. We show, however, that for two-to-two processes the two-loop anomalous dimension matrix is diagonal in the same color exchange basis as the one-loop matrix for scattering at ninety degrees in the center of mass.

To Ryumi

Contents

List of Figures

List of Tables

Acknowledgements

First and foremost, I would like to acknowledge George Sterman for the advice, encouragement and superb supervision he has offered me over the course of my PhD. Without George carefully guiding me in the right direction and helping solve my myriad of problems, this thesis would never exist.

Thanks also to all the people who offered me help, either face-to-face or by email. These include Gilad Perez, Jack Smith, Fred Goldhaber, Werner Vogelsang, Gavin Salam, Alex Mitov, Seung Lee, Leo Almeida, Yu-tin Huang, Zuowei Liu, Moises Picon, Joe Virzi, Chee Sheng Fong, Peng Dai, Pat Peiliker and Betty Gasparino. Thanks also go to all the people I have accidently omitted. I would also like to thank the C.N. Yang Institute for Theoretical Physics, for providing a stimulating, enjoyable place to work and for agreeing to fund my PhD study.

Finally, I would like to thank Ryumi for her love and support.

Chapter 1

Quantum Chromodynamics

The topics we will explore in this thesis are rooted in perturbative Quantum Chromodynamics (QCD) and related gauge theories, with an emphasis on the infrared structure of perturbative amplitudes. We mainly develop factorization and resummation formalisms to understand properties that appear in higher order calculations, and study how these properties can be used directly or indirectly to discover physics beyond the standard model (BSM) in collider experiments.

1.1 The theory of the strong force

QCD is our best understanding of the strong force, describing interactions between quarks and gluons, altogether called partons, which are fundamental constitutes of hadrons. In this chapter, we will start by summarizing the development of QCD as the theory of strong interactions. In the development of modern physics, one of the main interests was to find fundamental particles that cannot be broken up further. The success in describing electromagnetism in terms of interactions between its fundamental particles, charged leptons and the photon, naturally suggested the search for fundamental particles inside hadrons such as protons and neutrons. The large number of strong resonances, such as Δ, and mesons (π, K, ϕ, $\cdots$), suggested that hadrons are composite.

In the sixties, Gell-Mann and Zweig introduced models in which all strongly interacting particles are composed of more fundamental particles called quarks [1]. A few years later the results in deeply inelastic scattering (DIS) experi-

ments at SLAC revealed the evidence for a charged substructure in protons and neutrons, which could fit into the quark model. This resulted in boosting the search for a theory of the strong force that explains both DIS experiments at SLAC and the large number of different types of hadrons. Shortly after, Feynman [2] postulated a description of the compositeness of hadrons in terms of partons at very high energies in order to explain the scaling properties of DIS cross sections. This model also explained partons as quarks with spin-1/2 by the Callan-Gross relation [3]. Following the parton model [2, 4], we may write the inclusive cross section for nucleon-electron DIS as

$$\sigma_{eN}(p,Q) = \sum_q \int_0^1 d\xi\, \sigma_{eq}^{(elastic)}(\xi p, Q)\, \phi_{q/N}(\xi)\,, \tag{1.1}$$

where $\sigma_{eq}^{(elastic)}(\xi p, Q)$ is the free, elastic scattering of a quark by an electron, with the parton's momentum given by ξp, $1 > \xi > 0$. Here, the functions $\phi_{q/N}(\xi)$ describe probabilities to find a parton q inside hadron N. This implies that in some sense partons are weekly coupled at high energies, which seemed to contradict the strong force.

This paradox can be explained by the property of asymptotic freedom, discovered in 1973 by Politzer [5] and Gross and Wilczek [6]. It was realized that a local nonabelian gauge theory describes important properties in the parton model where the theory promotes the color SU(3) symmetry in quark models [7, 8] to local, non-abelian Yang-Mill gauge symmetry [9]. As a consequence of the local symmetry, this theory, which we call now QCD, is invariant under the local SU(3) transformation that became a part of the $\mathrm{SU(3)} \bigotimes \mathrm{SU(2)}_L \bigotimes \mathrm{U(1)}$ Standard Model of elementary particle physics; the other sectors correspond to the theory of electroweak interactions.

The Lagrangian density of QCD, including gauge fixing and ghost terms, may be written for arbitrary color N_c as

$$\begin{aligned} \mathcal{L} &= \sum_f \bar{q}_{f,i}(i\partial\!\!\!/\delta_{ij} + i g_s A\!\!\!/_a (T_F^a)_{ij} - M_f \delta_{ij}) q_{f,j} \\ &\quad -\frac{1}{2}\mathrm{Tr}\,(F_{\mu\nu}F^{\mu\nu}) - \frac{1}{2\xi}(\partial \cdot A_a)^2 + \partial_\mu \bar{c}_a (\partial^\mu \delta_{ad} - g_s f_{abd} A_b{}^\mu) c_d\,. \end{aligned} \tag{1.2}$$

Here the quark fields q_f with flavor f ($f = 1, \cdots, n_f$), color i ($i = 1, \cdots, N_c$)

and mass M_f transform in the fundamental representation of the gauge group $\mathrm{SU}(N_c)$. The gluons fields are A_a^μ, $a = 1, \cdots, N_c^2 - 1$, and ghost fields c_a (and antighost $\bar{c}_a$), $a = 1, \cdots, N_c^2 - 1$, in the adjoint representation of $\mathrm{SU}(N_c)$. The T_F^a are the generators of the group $\mathrm{SU}(N_c)$ in the N_c-dimensional defining representation. The field strengths $F^{\mu\nu} \equiv F_a^{\mu\nu} T_F^a$ are given by

$$F^{\mu\nu} = \partial^\mu A^\nu - \partial^\nu A^\mu + i g_s [A^\mu, A^\nu] \,. \tag{1.3}$$

The non-abelian gauge theory is renormalized [10], and the strength of the coupling g_s in Eq. (1.2) thus depends on the renormalization scale μ.

$$\begin{aligned} \frac{\partial}{\partial \ln \mu} g_s(\mu)|_{g_0} &= \beta\left(g_s(\mu)\right) \\ &= -\beta_0 \frac{g_s^3(\mu)}{(4\pi)^2} + \cdots \,, \end{aligned} \tag{1.4}$$

where the bare coupling g_0 held fixed, and where $\beta_0 = (11 N_c - 2 n_f)/3$ at one-loop. The solution to Eq. (1.4) is then

$$g_s(\mu) = \frac{16\pi^2}{\beta_0 \ln\left(\mu^2/\Lambda^2\right)} \,. \tag{1.5}$$

The coupling $g_s(\mu)$, or equivalently "alpha-strong",

$$\alpha_s(\mu) \equiv \frac{g_s^2(\mu)}{4\pi} = \frac{\alpha_s(\mu_0)}{1 + \alpha_s(\mu_0)\beta_0 \ln\left(\frac{\mu^2}{\mu_0^2}\right)} \,, \tag{1.6}$$

describes the property of asymptotic freedom: the coupling charactering the interaction between quarks and gluons decreases as the energy scale μ increases.

It was a great success that QCD described well the basic properties of hadrons in DIS, but there were still steps to take to understand and to describe a full picture of hadronic collisions in perturbative QCD, because our true asymptotic states are not partons but the hadrons. Although there have been several techniques developed to calculate physical quantities directly in strong coupling regimes by using theoretical tools such as chiral perturbation theory [11], lattice gauge theory [12] and QCD instantons [13], we are still

far from fully understudying confinement theory of quarks. To apply QCD as a tool for calculation in high energy hard scattering, we rely on asymptotic freedom supplemented by factorization theorems.

In a naive use of perturbation theory, we face with two major difficulties in an order by order expansion in powers of the coupling constant. Each coefficient beyond lowest order involves calculations of internal loop momenta. At very high values of internal loop momenta, we encounter divergences called Ultraviolet (UV) divergences. UV divergences are systematically removed at each order and to all orders by renormalization [10]. On the other hand, at very low energies we face a different type of divergence due to infrared (IR) regions of soft and collinear momenta. The IR divergences generally appear in calculations that involve at least one on-shell external momentum. These IR divergences can be understood as due to the degenerate states in the limit where particles are soft or collinear. In principle, it is not possible to distinguish soft emissions and collinear splittings from the states that describe the same kinematics without these emissions and splittings. This observation gives a hint on how to handle IR divergences.

Inclusive cross sections, which sum over all indistinguishable states remove IR divergences, although they appear on a diagram by diagram basis. Bloch and Nordesieck showed that IR divergences canceled in QED after the summation over final states with soft photons [14]. The analyses of Kinoshita and of Lee and Nauenberg extended the summation over final state degeneracies to initial states, which produces total transition probabilities that are free from IR divergences [15] in QCD as well as QED. The finiteness of both the soft and collinear limit as criteria for the use of perturbative QCD was first introduced in the work of Sterman and Weinberg on jet cross sections [16–18] for e^+e^- annihilations.

The situation however is somewhat different between QED and QCD. The self-coupling of the gluons of QCD leads to strong interactions in QCD at low energies, which are not present in QED. Although we remove all IR divergences in certain physical quantities, we cannot perform reliable calculations in the regimes of low energies at which perturbatively incalculable mechanisms confine partons. As a result, in order to compare to results in experiments, asymptotic freedom is not enough to obtain physical quantities for processes

with initial states that include hadrons. It was thus necessary to find some relations to link high energy, short distance partonic phenomena in perturbative QCD to the confined states of partons as hadrons which we observe in experiments. Factorization theorems that we will discuss in the next section allow one to separate short and long distance physics in physical quantities [19].

1.2 Factorization and evolution

Factorization is the systematic separation of dynamics associated with long and short distance physics. Factorization can be proven in a rigorous way for certain processes, assuming that the regulated theory has bound states whose formation decouples from short distance dynamics (See reviews in Ref. [19]). We can calculate quantities governed by only short distance physics perturbatively, due to asymptotic freedom introduced in the previous section. We may understand this separation mechanism from Fig. 1.1 for DIS processes. Let us imagine that an electron is colliding with a proton where both particles have very high energy and that there is a comparable momentum transfer Q. In the center of mass frame, the proton is highly Lorentz contracted in the longitudinal direction, while partons in the proton are well separated. We assume that wave functions describing confinement among partons in the proton have fixed interaction times which are an order of Λ^{-1} in Eq. (1.6). This time scale is much longer than the collision time between the wave functions of the two particles of energy Q. The internal interactions of the partons then do not interfere with the collision process, and we may describe the collision incoherently from the confining interactions inside a proton. The collisions and the wave functions can thus contribute multiplicatively in the cross section. That is, they can be factorized.

We emphasize that the collision of Fig. 1.1 can occur when two particles are within a distance $1/Q$ that allows momentum exchange of order Q. This probability is very low, that is about $\left(\frac{1}{R^2\,Q^2}\right)^n$ for collisions of an electron with one hadron, where R is a radius of hadrons and where n is a number of partons that participate in the hard scattering. Following the same logic, for proton-(anti)proton scattering processes, we may effectively describe the collisions as collisions of two partons, one for each (anti)proton. The probability of colliding

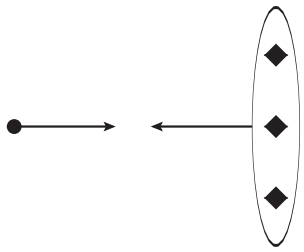

Figure 1.1: Heuristic picture of parton model DIS. Diamond shapes stand for partons inside a protons

two partons in one proton to two partons in another, both with momentum transfer of order Q, is extremely low due to the above reasoning, and we may neglect this possibility.

In summary, collisions of two hadrons at high energies and large momentum transfers can be effectively disentangled into two pieces; collisions of two partons that can be described in perturbative QCD, and the mechanism described by long distance QCD for hadronizing external partons. For example, inclusive cross sections involving dijet production in hadronic collisions can be written in a convolution of functions as

$$\begin{aligned} \sigma_{h_A\, h_B \to J_1\, J_2} \;&=\; \sum_{a,\,b} \int dx_1\, dx_2\, \phi_{f_a/A}(x_1,\,\mu_F) \phi_{f_b/B}(x_2,\,\mu_F) \\ &\qquad \times \hat{\sigma}_{f_a\, f_b \to J_1\, J_2}(x_1, x_2, \mu_F, p_{J_1}, p_{J_2})\,, \end{aligned} \tag{1.7}$$

where μ_F is a factorization scale, and where the sum is over all parton types f_q. Here the functions $\phi_{f_i/A}$ are parton distribution functions (PDFs), describing long distance dynamics, and $\hat{\sigma}_{f_a\, f_b \to J_1\, J_2}$ is the IR safe hard-scattering or short-distance function. The dependence on jet momenta, p_{J_i}, is entirely in the hard scattering function. The distribution functions cannot be determined in perturbation theory but can be obtained by fitting to experimental data [20].

We now may notice that the physical quantities such as $\sigma_{h_A\, h_B \to J_1\, J_2}$ in Eq. (1.7) cannot depend on the factorization scale μ_F that separates short- and long-distance physics. This consistency requirement leads to the "evolution

equations" of PDFs [21–24]

$$\mu \frac{d}{d\mu} \phi_{f_a/A}(x,\, \mu_F) = \sum_{f_b} \int_x^1 \frac{d\xi}{\xi} P_{f_a\, f_b}\left(\xi,\, \alpha_s(\mu_F)\right) \phi_{f_b/A}\left(\frac{x}{\xi},\, \mu_F\right) , \qquad (1.8)$$

where the evolution kernels (or spliting functions) $P_{f_a\, f_b}$ describe the differential probability of finding parton f_a in parton f_b with fractional momentum ξ, and are calculable as a power series in α_s. The evolution equation indicates that measuring a parton density at one scale μ_F allows us to predict the parton density at another scale μ_F' if both scales are much above Λ in Eq. (1.6).

1.3 Outline

Here is an outline of this thesis. Chapters 1 and 2 are devoted to a summary of some of the fundamental ideas of QCD, and provide the reader with some of the tools that are used in the rest of the thesis. We have begun with an introduction to QCD and the use of QCD as perturbation theory including the property of asymptotic freedom, and proceed with a discussion of factorization. In the following, we discuss the refactorization of hard scattering functions. The color mixing matrices of QCD for hadronic collisions are then described, with a sample calculation for a quark process.

In Chap. 3 and 4, we study events with highly-boosted massive particles such as top, W, Z and Higgs at the LHC for the discovery of new physics at very high energies. We explain that in many decay channels these particles would be identified as high-p_T jets, and any such signal of definite mass must be disentangled from a large background of QCD jets. We then show that this background far exceeds such signals, and relying solely on jet mass as a way to reject QCD background from signal would probably not suffice in most cases. In this procedure, we use the collinear enhancement in perturbative QCD amplitudes to distinguish products of high-boosted massive particle decay from QCD jets whose collinear structure is described by a factorized jet function. In addition to this method, we find that jets from QCD are characterized by different patterns of intrajet energy flow compared to highly-boosted heavy particle decays, and we then introduce several event shapes that could be used to disentangle signals from backgrounds. This work has appeared in

Refs. [25, 26].

In Chap. 5, we start from the assumption that we have signals from BSM s-channel resonances, disentangled well from all QCD backgrounds through the above or other techniques. It is then natural to ask if one may determine the SM gauge content of BSM resonances. We introduce a method to determine the color SU(3) gauge content of BSM resonances from new physics signals by investigating the pattern of soft gluon radiation into specified regions of a detector. We present the use of energy flow, treated by perturbative QCD, factorization and color flow introduced in Chap. 1 and 2, as a tool to analyze properties of new physics. Following this method, we find a quite large difference in radiation into certain regions of a detector from color singlet and octet resonances. This work has appeared in Ref. [27].

The theme of Chap. 6 is the soft anomalous dimension matrix for massive external particles at two loops, a quantity that arises from the refactorization of short-distance functions described in Chap. 2. We use an analysis in Euclidean space, showing that the contributions to these matrices from diagrams that link three massive Wilson lines do not vanish in general. This differs from the pattern found with massless external lines [28], where it was discovered that massless soft anomalous dimension matrices at two loops are proportional to their one-loop forms. We find, however, that at ninety degrees in the center of mass the massive anomalous dimension matrix also restores proportionality to their one-loop value. This work has appeared in Ref. [29]

Chapter 2

Refactorization and Color Mixing

2.1 Refactorization and resummation

In addition to the concept of factorization discussed in the previous chapter and illustrated in Eq. (1.7), we can often perform a further factorization on the short distance function $\hat{\sigma}_{f_a\, f_b \to J_1\, J_2}$ in Eq. (1.7) that describes the formation of the final state from partons f_a and f_b. We refer to this procedure as refactorization of the partonic cross section. Since factorization theorems isolate long distance dynamics into PDFs, short distance dynamics can be determined within perturbative calculations if coefficients of the perturbative expansion are small. The coefficients depend on processes we are interested in, and are sometimes enhanced in certain regions of phase space integrations. For fully inclusive cross sections, once PDFs have been factorized there is a complete cancellation between real and virtual infrared and collinear corrections at each order in α_s. On the other hand, for many less-inclusive observables the cancellation between two corrections is incomplete. As a result, the coefficients at each order introduce logarithmic enhancements which could possibly spoil perturbative expansions. To obtain reliable predictions, we should resum these logarithms to all order in a systematic way. This procedure is called resummation, and this is one of main subjects in this thesis.

The logarithms emerge from the uncanceled regimes of soft and collinear phase space integrals. They can be thus further identified by soft gluon emis-

sions at wide angles from jets and by collinear splittings within jets. The separation of the types of these logarithms can be understood by consideration of different energy scales.

The wavelengths of soft gluons emitted at wide angles to a set of collinear partons, called a jet subdiagram (or jet for short), are long enough that it cannot resolve the substructure of the jet. Soft gluon emission depends only on the total color (triplet or octet) of the jet, and its light-like velocity, which we will refer to as β^μ. We can prove this in a rigorous way [19] by using the Ward Identities once we identify the momentum regions of each enhancement by an IR power counting. This procedure leads to the result that IR-regulated partonic amplitudes $|\,\mathcal{M}_{\rm f}\rangle$ can be factorized into functions representing short-distance dynamics, collinear dynamics of external partons, and soft gluon exchange between light and heavy partons,

$$\begin{aligned}\left|\,\mathcal{M}_{\rm f}\left(p_i,\frac{Q}{\mu},\alpha_s(\mu),\varepsilon\right)\right\rangle \;&=\; \prod_i J^{[i]}\left(p_i,\alpha_s(\mu),\varepsilon\right)\\ &\times \mathbf{S}_{\rm f}\left(\beta_i,\frac{Q}{\mu},\alpha_s(\mu),\varepsilon\right)\,\Big|\,H_{\rm f}\left(p_i,\frac{p_i}{\mu},\frac{Q}{\mu},\alpha_s(\mu)\right)\Big\rangle\;. \end{aligned} \tag{2.1}$$

Here we use the notation of Ref. [30], where the ket $|A(\rho,\varepsilon)\rangle$ is defined by

$$|A(\rho,\varepsilon)\rangle = \sum_{L=1}^{C} A_L(\rho,\varepsilon)\;\;(c_L)\;, \tag{2.2}$$

with (c_L) some basis of color tensors linking the parton lines at short distances. In Eq. (2.1), we regularize infrared enhancements in renormalized amplitudes by continuing to D dimensions, where they appear as poles in $\varepsilon = 2-D/2$. The β's in Eq. (2.1) describe the velocities of external partons, and the p_i's their momenta. The jet functions $J^{[i]}$ for incoming and outgoing on-shell partons may be defined, for example, as the square root of the corresponding elastic form factors [31]. The soft matrix $\mathbf{S}_{\rm f}$, which depends only on the velocities and color representation of the jets, describes the infrared behavior of color exchange between the external partons. It remains after the factorization of collinear enhancements into the jet functions, and in general mixes the color components found at short distance. We will study this subject in detail in the next section.

To focus on evolution of the color flow, we will consider cross sections and related observables that are inclusive enough to avoid collinear enhancements, but which have a specific restriction on the energy of gluon emission. One of the observables will be a rapidity gap process where we measure interjet radiation of energy Q_c away from the jets themselves. The associated partonic scattering process for proton and (anti)-proton collisions is

$$\mathrm{f}: \ f_1(p_1) + f_2(p_2) \to Q(p_a) + \bar{Q}(p_b) + \Omega_{gap}(Q_c) + X \,, \tag{2.3}$$

for the production of a heavy quark pair at fixed rapidity difference, $\Delta\eta = \eta_a - \eta_b$. Here the f_i refer to partons that participate in the collision, and we have labeled process (2.3) "f". The corresponding short distance partonic cross section, free from collinear enhancements, can be written, based on Eq. (2.1), as

$$\hat{\sigma}^{(\mathrm{f})}(Q, Q_c, \alpha_s(\mu)) = \sum_{I,\,L} H_{IL}^{(\mathrm{f})}(Q, \alpha_s(\mu)) S_{LI}(Q_c, \alpha_s(\mu)) \,, \tag{2.4}$$

where μ is a refactorization scale which could be different from the factorization scale μ_F in Eq. (1.7), and where color tensors labeled by L and I account for the color flow at the short distance scale. We refer to this as a refactorization of the partonic hard scattering.

As a specific example, in the following we will study factorized and refactorized forms for the inclusive cross section for heavy quark pair production in rapidity gap processes, and perform resummation from evolution equations. We will return to this process in Chap. 5. The same formalism will also be used to study high-p_T jets in Chap. 3 and 4. The inclusive cross section for heavy quark pair production at rapidity difference $\Delta\eta$ with fixed energy flow Q_c is given in standard factorized form by

$$\frac{d\sigma_{AB}}{d\Delta\eta\, dQ_c} = \sum_{f_1, f_2} \int dx_1 dx_2\, \phi_{f_1/A}(x_1, \mu_F) \phi_{f_2/B}(x_2, \mu_F) \frac{d\hat{\sigma}^{(\mathrm{f})}}{d\Delta\eta\, dQ_c} \,. \tag{2.5}$$

Here $\phi_{f_1/A}$ and $\phi_{f_2/B}$ are PDFs, evaluated at the factorization scale μ_F. Below, we generally use the scale $\mu_F = p_T$, the transverse momentum p_T of the produced parton $Q(p_a)$ or $\bar{Q}(p_b)$ of mass m_Q in Eq. (2.3). The partonic scattering

cross section $d\hat{\sigma}^{(\mathrm{f})}/d\Delta\eta dQ_c$ can be expanded in α_s, starting from the lowest order (LO) Born cross section

$$\frac{d\hat{\sigma}^{(\mathrm{f})}}{d\Delta\eta\, dQ_c} = \frac{d\hat{\sigma}^{(\mathrm{f},LO)}}{d\Delta\eta}\delta(Q_c) + \cdots\,, \tag{2.6}$$

where corrections may include potentially large logarithms of p_T/Q_c. Again, the index f denotes the partonic process for heavy quark pair production in Eq. (2.3). Following Ref. [32], we consider the partonic cross sections integrated over the transverse energy, Q_c, radiated into a symmetric, central rapidity gap region of size, Y, up to a fixed value Q_0,

$$\begin{aligned}\frac{d\hat{\sigma}^{(\mathrm{f})}(m_Q, Q_0, \mu_F, \Delta\eta, Y, \alpha_s(\mu_F))}{d\Delta\eta} \\ = \int_0^{Q_0} dQ_c \frac{d\hat{\sigma}^{(\mathrm{f})}(m_Q, Q_c, \mu_F, \Delta\eta, Y, \alpha_s(\mu_F))}{d\Delta\eta\, dQ_c}\,.\end{aligned} \tag{2.7}$$

We note that when Eq. (2.7) is divided by the total cross section, the ratio can be interpreted as the probability for heavy quark pair production with soft gluon radiation into the gap region up to energy flow Q_0.

The partonic cross sections of Eq. (2.7) is now refactorized into a hard scattering matrix $H_{IL}^{(\mathrm{f})}$ and a soft matrix $S_{LI}^{(\mathrm{f})}$ as in (2.6),

$$\begin{aligned}\frac{d\hat{\sigma}^{(\mathrm{f})}}{d\Delta\eta}(M, m_Q, Q_0, \mu_F, \Delta\eta, Y, \alpha_s(\mu_F)) &= \sum_{L,I} H_{IL}^{(\mathrm{f})}(M, m_Q, \mu_F, \mu, \Delta\eta, \alpha_s(\mu)) \\ &\quad \times S_{LI}^{(\mathrm{f})}\left(\Delta\eta, Y, \frac{Q_0}{\mu}, \alpha_s(\mu), m_Q\right)\,,\end{aligned} \tag{2.8}$$

where matrix $H_{IL}^{(\mathrm{f})}$ represents interactions at short distances, independent of soft gluon radiation. Here we have introduced a refactorization scale μ. The soft function $S_{LI}^{(\mathrm{f})}$ describes the radiation of soft gluons up to the scale Q_0, which decouples from the dynamics of the hard scattering.

As noted above the soft function depends on the jet color and velocities only. It can thus be written in terms of products of path-ordered exponentials,

$w_L^{(\mathrm{f})}(x)_{\{b_i\}}$, of the gluon field as [32],

$$S_{LI}^{(\mathrm{f})} = \int_0^{Q_0} dQ_c' \sum_n \sum_{\{b_i\}} \delta(Q_0^{(n)} - Q_c') \times \langle 0|\bar{T}[(w_L^{(\mathrm{f})}(0))_{\{b_i\}}^\dagger]|n\rangle\langle n|T[(w_I^{(\mathrm{f})}(0))_{\{b_i\}}]|0\rangle \,, \tag{2.9}$$

where we sum over all states n whose transverse energy flow into the gap is restricted to equal Q_c' and where color tensors labeled by L and I account for the color flow at the hard scattering. Eikonal multipoint operators, $(w_L^{(\mathrm{f})}(x))_{\{b_i\}}$, with color indices $\{b_i\}$ are written as products of ordered exponentials, tied together by color tensors, c_L,

$$(w_L^{(\mathrm{f})}(x))_{\{b_i\}} = \sum_{\{d_i\}} \Phi_{\beta_b}^{(f_b)}(\infty,0;x)_{b_b,d_b}\Phi_{\beta_a}^{(f_a)}(\infty,0;x)_{b_a,d_a} \times (c_L^{(\mathrm{f})})_{d_b,d_a;d_1,d_2}\Phi_{\beta_1}^{(f_1)}(0,-\infty;x)_{d_1,b_1}\Phi_{\beta_2}^{(f_2)}(0,-\infty;x)_{d_2,b_2} \,, \tag{2.10}$$

where the non-Abelian path-ordered phase operators (Wilson lines), $\Phi_\beta^{(f)}$, are given by

$$\Phi_\beta^{(f)}(\infty,0;x) = P\exp\left[-ig\int_0^\infty d\lambda\beta\cdot A^{(f)}(\lambda\beta+x)\right] . \tag{2.11}$$

Here, β is the four-velocity, and the vector potentials $A^{(f)}$ are in the color representation appropriate to flavor f. At the tree level, Eq. (2.9) reduces to the trace of the product of color tensors.

The product of hard and soft functions in Eq. (2.8) is independent of the refactorization scale, μ. From this, we easily derive for $S_{LI}^{(\mathrm{f})}$ the evolution equation [33]

$$\left(\mu\frac{\partial}{\partial\mu} + \beta(g_s)\frac{\partial}{\partial g_s}\right) S_{LI}^{(\mathrm{f})} = -(\Gamma_S^{(\mathrm{f})})_{LJ}^\dagger S_{JI}^{(\mathrm{f})} - S_{LJ}^{(\mathrm{f})}(\Gamma_S^{(\mathrm{f})})_{JI} \,, \tag{2.12}$$

in terms of a matrix of anomalous dimensions, $(\Gamma_S^{(\mathrm{f})})_{JI}$. The matrix $\Gamma_S^{(\mathrm{f})}(\Delta\eta, Y, \rho)$ depends on kinematics, including the geometric information of the gap region and the heavy quark mass. Solving this equation will enable us to resum the leading logarithms of the soft scale Q_0. In heavy quark pair production, de-

pendence on the quark mass in soft functions will always appear through the parameter ρ, given by

$$\rho \equiv \sqrt{1 + \left(\frac{m_Q}{p_T}\right)^2}\,. \tag{2.13}$$

We will find that the soft function depends on the velocities β_i only through $\Delta\eta$ and ρ.

To obtain the solution to Eq. (2.12), we treat above equation in a basis that diagonalizes $\Gamma_S^{(\mathrm{f})}$,

$$\begin{aligned}(\Gamma_S^{(\mathrm{f})}(\Delta\eta, Y, \rho))_{\gamma\beta} &\equiv \lambda_\beta^{(\mathrm{f})}(\Delta\eta, Y, \rho)\delta_{\gamma\beta} \\ &= (R^{(\mathrm{f})})_{\gamma I}\,(\Gamma_S^{(\mathrm{f})}(\Delta\eta, Y, \rho))_{IJ}\,(R^{(\mathrm{f})^{-1}})_{J\beta}\,, \end{aligned} \tag{2.14}$$

where the eigenvalues $\lambda_\beta^{(\mathrm{f})}$ are given by a series in α_s,

$$\lambda_\beta^{(\mathrm{f})}(\Delta\eta, Y, \rho) = \frac{\alpha_s}{\pi}\lambda_\beta^{(\mathrm{f},1)}(\Delta\eta, Y, \rho) + \cdots\,. \tag{2.15}$$

We can transform the soft and hard matrices in the diagonalized basis

$$\begin{aligned} S_{\gamma\beta}^{(\mathrm{f})} &= [((R^{(\mathrm{f})})^{-1})^\dagger]_{\gamma L}\, S_{LK}^{(\mathrm{f})}\, [(R^{(\mathrm{f})})^{-1}]_{K\beta}\,, \\ H_{\gamma\beta}^{(\mathrm{f})} &= [R^{(\mathrm{f})}]_{\gamma K}\, H_{KL}^{(\mathrm{f})}\, [R^{(\mathrm{f})^\dagger}]_{L\beta}\,. \end{aligned} \tag{2.16}$$

This change of basis uses the transformation matrix $[(R^{(\mathrm{f})})^{-1}]_{K\beta} = (e_\beta)_K$, where e_β are eigenvectors of the soft anomalous dimension matrix.

The solution to Eq. (2.12) gives the dependence of $S^{(\mathrm{f})}$ on the ratio μ/Q_0,

$$\begin{aligned} &S_{\gamma\beta}^{(\mathrm{f})}\left(\Delta\eta, Y, \frac{Q_0}{\mu}, \alpha_s(\mu), \rho\right) \\ &\quad = S_{\gamma\beta}^{(\mathrm{f})}(\Delta\eta, Y, 1, \alpha_s(Q_0), \rho)\exp\left[-E_{\gamma\beta}^{(\mathrm{f})}\int_{Q_0}^{\mu}\frac{d\mu'}{\mu'}\left(\frac{\beta_0}{2\pi}\alpha_s(\mu')\right)\right] \\ &\quad = S_{\gamma\beta}^{(\mathrm{f})}(\Delta\eta, Y, 1, \alpha_s(Q_0), \rho)\left[\ln\left(\frac{Q_0}{\Lambda}\right)\right]^{E_{\gamma\beta}^{(\mathrm{f})}}\left[\ln\left(\frac{\mu}{\Lambda}\right)\right]^{-E_{\gamma\beta}^{(\mathrm{f})}}. \end{aligned} \tag{2.17}$$

We will choose below μ and μ_F to be the hard scale p_T for use in the refactorized partonic cross section (2.8). In Eq. (2.17) the exponents $E_{\alpha\beta}^{(\mathrm{f})}$ are given in terms

of sums of the eigenvalues of Γ_S by

$$E^{(\mathrm{f})}_{\gamma\beta}(\Delta\eta, Y, \rho) = \frac{2}{\beta_0}[\lambda^{(\mathrm{f},1)*}_{\gamma}(\Delta\eta, Y, \rho) + \lambda^{(\mathrm{f},1)}_{\beta}(\Delta\eta, Y, \rho)]\,. \tag{2.18}$$

Equation (2.18) shows that the diagonal exponents, $E^{(\mathrm{f})}_{\alpha\alpha}$, are real. In the second form of Eq. (2.17), we have used the one-loop QCD running coupling in Eq. (1.6). Combining Eqs. (2.8) and (2.17), the resummed partonic cross section, valid to leading logarithm, is then

$$\begin{aligned}\frac{d\hat{\sigma}^{(\mathrm{f})}}{d\Delta\eta} &= \sum_{\beta,\gamma} H^{(\mathrm{f},LO)}_{\beta\gamma}(m_Q, \Delta\eta, \alpha_s(p_T)) \\ &\quad \times S^{(\mathrm{f},0)}_{\gamma\beta}\left[\ln\left(\frac{Q_0}{\Lambda}\right)\right]^{E^{(\mathrm{f})}_{\gamma\beta}}\left[\ln\left(\frac{p_T}{\Lambda}\right)\right]^{-E^{(\mathrm{f})}_{\gamma\beta}}.\end{aligned} \tag{2.19}$$

2.2 Color mixing in QCD

The refactorization properties discussed in the last section will be studied in later chapters to resum logarithmic enhancements by solving evolution equations in Eq. (2.12). As we saw in Eq. (2.17), the solution to evolution equations for a soft function with one-loop anomalous dimension corresponds to the summation of the leading logarithms in loop calculations, after subtracting collinear enhancements, at each order to all orders. This is also the same as the results from the sum of diagrams that dress a gluon one at each order on a pair of external partons in all possible ways, where gluons are ordered in energies or transverse momenta from hard to soft. [1] Also in this picture gluons cannot be crossed in amplitudes because this structure cannot produce leading logarithmic enhancements [17, 18, 34]. In this section, we study these one-loop diagrams, which we will use later to compute the anomalous dimension matrices Γ_S, introduced in the previous section.

For processes involving only two partons such as $e^+\,e^- \to J_1\,J_2$, the exchange of gluons between the outgoing jets does not change the color state of the system. This guarantees that the successive gluon emissions in the leading accuracy always produce the same color factors, C_F, at each order. On the other hand, for dijet production in hadronic collisions, each gluon

[1] The showering mechanism in Monte Carlo simulations follows this picture.

exchange may change the color state in the system. This means that gluon exchanges could bring the different color factors at each order, depending on the color states of the hard and soft functions. The dynamics at each order thus should be classified in the space of possible color tensors that link the outgoing partons, and the summation of the leading logarithmic enhancements can be realized in a matrix form in the space of color tensors which appear in Eq. (2.10). The hard and soft functions for dijet or hadron production in hadronic collisions (2.4) are thus expressed in the basis of color tensors. We will study the mixing of color tensors to leading logarithm.

We consider the color flow of $2 \to 2$ scattering processes,

$$f_A(p_A, r_A) + f_B(p_B, r_B) \to f_1(p_1, r_1) + f_2(p_2, r_2) \,, \tag{2.20}$$

where the index r_i refers to the color of particles i. We label initial state particles A and B, the final state particles 1 and 2. In this notation, the expression of color states for $q\bar{q}$ scattering with a t-channel gluon would then be written as $(T_F^a)_{r_1 r_A}(T_F^a)_{r_B r_2}$ where the T_F^a's are the generators of SU(N_c) in the fundamental representation. In order to decompose the color flow of a matrix element, we need to specify a basis of color tensors, linking external partons, which describe the possible underlying color flows. For example, the process $q\bar{q} \to q\bar{q}$ with any number of gluon exchanges can be decomposed into the basis of color singlet c_1 and octet c_2 tensors,

$$\begin{aligned} c_{1\{r_f\}} &= \delta_{r_A r_1}\delta_{r_B r_2} \,, \\ c_{2\{r_f\}} &= \frac{1}{2}\left(\delta_{r_A r_B}\delta_{r_1 r_2} - \frac{1}{N_c}\delta_{r_A r_1}\delta_{r_B r_2}\right) \,, \end{aligned} \tag{2.21}$$

where r_f is the color index of parton f in Eq. (2.20), and where we have used the color identity, as shown in Fig. 2.1,

$$(T_F^a)_{r_1 r_A}(T_F^a)_{r_B r_2} = \frac{1}{2}\left(\delta_{r_A r_B}\delta_{r_1 r_2} - \frac{1}{N_c}\delta_{r_A r_1}\delta_{r_B r_2}\right) \,. \tag{2.22}$$

Note that the basis tensor c_2 describes the color state for a t-channel gluon exchange. The above scattering amplitude in Eq. (2.1) can then be written in

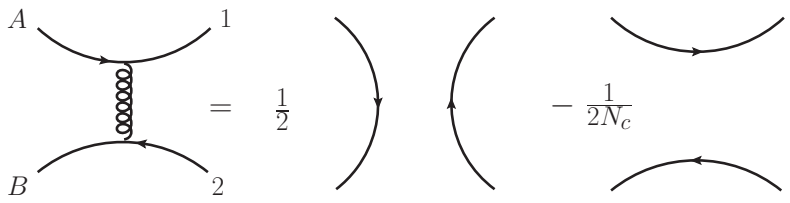

Figure 2.1: Color identity corresponding to Eq. (2.22).

terms of these two tensors as

$$|\mathcal{M}\rangle = \sum_i \mathcal{M}_i \, (c_i)_{\{r_f\}} \,, \tag{2.23}$$

where the $\mathcal{M}_i$ are coefficients determined by the choice of color basis and the results of loop calculations. Therefore if the original basis set is denoted by (c_1, c_2) and if the basis set that results after gluon exchange is denoted by (c_1', c_2'), then

$$\begin{pmatrix} c_1' \\ c_2' \end{pmatrix} = \begin{pmatrix} \mathcal{C}_{11} & \mathcal{C}_{12} \\ \mathcal{C}_{21} & \mathcal{C}_{22} \end{pmatrix} \begin{pmatrix} c_1 \\ c_2 \end{pmatrix} . \tag{2.24}$$

In the following we derive the color factors, $\mathcal{C}_{ij}$, and momentum dependence in the space of associated color basis due to color flow in gluon exchange. The exchange of a gluon mixes the set of color tensors, and the mixing is controlled by the color mixing matrix in Eq. (2.24). As examples, we will consider detailed examples for processes $q\bar{q} \to q\bar{q}$, following Ref. [35].

2.2.1 Color mixing in process $q\,\bar{q} \to q\,\bar{q}$

The color mixing matrix for process $q\,\bar{q} \to q\,\bar{q}$, illustrated in Fig. 2.2, can be constructed by using the color identity in Eq. (2.22). For this process we follow the basis introduced in Eq. (2.21), which describes t-channel singlet and octet exchange. We note that other choices of color basis are possible as long as a set of the color basis spans the entire color space. In this case, the trace of

products of different color basis tensors vanish,

$$\begin{aligned}
\mathrm{Tr}\,(c_1 \times c_2) &= \mathrm{Tr}\left(\delta_{r_A r_1}\,\delta_{r_B r_2}\left(-\frac{1}{2N_c}\delta_{r_A r_1}\delta_{r_B r_2}+\frac{1}{2}\delta_{r_A r_B}\delta_{r_1 r_2}\right)\right)\\
&= \mathrm{Tr}\left(\frac{1}{2}\delta_{r_A r_A}-\frac{1}{2N_c}\delta_{r_A r_A}\,\delta_{r_B r_B}\right)\\
&= 0\,. \qquad (2.25)
\end{aligned}$$

We now begin to dress these bare tensors with a gluon attached to any two of the external legs. This gives six possible attachments. We denote the color tensor as $\left(\mathcal{E}_k^{ij}\right)_{\{r_f\}}$, resulting from the color basis tensor $(c_k)_{\{r_f\}}$ by the gluon exchange between the i and j external partons. We will concentrate on only color factors in this decomposition and leave loop calculations implicit. As illustrated in Fig. 2.2, let us begin with dressing color tensor c_1 with a gluon exchanged between initial partons A and B. We define the result as

$$\begin{aligned}
\left(\mathcal{E}_1^{(AB)}\right)_{\{r_f\}} &= \left(T_F^a\right)_{r_B r_n}(c_1)_{\{r_f\}}\left(T_F^a\right)_{r_m r_A}\\
&= \left(T_F^a\right)_{r_B r_n}\delta_{r_m r_1}\delta_{r_n r_2}\left(T_F^a\right)_{r_m r_A}\,,\\
&= (c_2)_{\{r_f\}}\,, \qquad (2.26)
\end{aligned}$$

which also indicates that $\left(\mathcal{E}_1^{(12)}\right)_{\{r_f\}} = (c_2)_{\{r_f\}}$. By similar calculations we find that

$$\left(\mathcal{E}_1^{(A1)}\right)_{\{r_f\}} = \left(\mathcal{E}_1^{(B2)}\right)_{\{r_f\}} = C_F(c_1)_{\{r_f\}}\,, \qquad (2.27)$$

$$\left(\mathcal{E}_1^{(B1)}\right)_{\{r_f\}} = \mathcal{E}_1^{(A2)} = (c_2)_{\{r_f\}}\,, \qquad (2.28)$$

where we have used

$$\left(T_F^a T_F^a\right)_{r_i r_j} = C_F\,\delta_{r_i r_j}\,. \qquad (2.29)$$

We next consider color mixing for the color state $(c_2)_{\{r_f\}}$. We note that this corresponds to the color structure of one-loop corrections on a t-channel hard

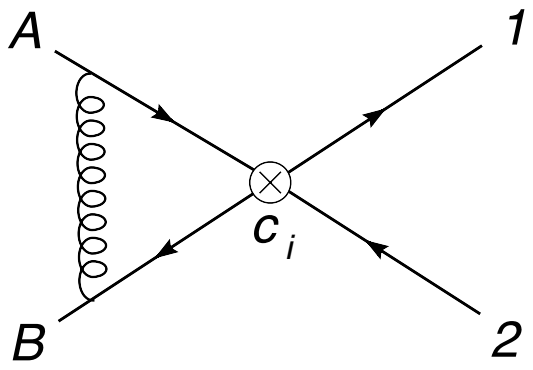

Figure 2.2: The diagram represents a gluon interaction between external partons A and B whose system before the gluon exchange forms the color tensor $(c_i)_{\{r_f\}}$. This diagram is denoted by $(\mathcal{E}_i^{(AB)})_{\{r_f\}}$ in Eq. (2.26).

function. Starting with $\left(\mathcal{E}_2^{(12)}\right)_{\{r_f\}}$ we have

$$\begin{aligned}\left(\mathcal{E}_2^{(12)}\right)_{\{r_f\}} &= (T_F^a)_{r_B r_n}\,(c_2)_{\{r_f\}}\,(T_F^a)_{r_m r_A} \\ &= (T_F^a)_{r_B r_n}\,\frac{1}{2}\left(\delta_{r_m r_n}\delta_{r_1 r_2} - \frac{1}{N_c}\delta_{r_m r_1}\delta_{r_n r_2}\right)(T_F^a)_{r_m r_A}\,. \end{aligned} \tag{2.30}$$

Using Eqs. (2.22) and (2.29) for the first and the second term in Eq. (2.30) we obtain

$$\left(\mathcal{E}_2^{(12)}\right)_{\{r_f\}} = \frac{C_F}{2N_c}(c_1)_{\{r_f\}} + \left(C_F - \frac{1}{2N_c}\right)(c_2)_{\{r_f\}}\,. \tag{2.31}$$

Following similar considerations for other diagrams we obtain

$$\begin{aligned}\left(\mathcal{E}_2^{(A1)}\right)_{\{r_f\}} &= \left(\mathcal{E}_2^{(B2)}\right)_{\{r_f\}} = -\frac{1}{2N_c}(c_2)_{\{r_f\}}\,, \\ \left(\mathcal{E}_2^{(B1)}\right)_{\{r_f\}} &= \left(\mathcal{E}_2^{(A2)}\right)_{\{r_f\}} = -\frac{1}{N_c}(c_2)_{\{r_f\}} + \frac{C_F}{2N_c}(c_1)_{\{r_f\}}\,. \end{aligned} \tag{2.32}$$

Let us define $\zeta^{(AB)}$ by the loop integral in Fig. 2.2 excluding color factors. We can now write down the mixing matrix for this process in terms of α, β and γ

defined in terms of the loop integral, $\zeta^{(ij)}$, of each relevant diagram,

$$\begin{aligned} \alpha &= \zeta^{(AB)} + \zeta^{(12)} , \\ \beta &= \zeta^{(A1)} + \zeta^{(B2)} , \\ \gamma &= \zeta^{(B1)} + \zeta^{(A2)} . \end{aligned} \tag{2.33}$$

We will obtain the complete forms of the loop integrals in Chap. 5 for a rapidity gap process. Recall that if the original set of color basis is denoted by (c_1, c_2) and the set which has mixed under a gluon exchange is denoted by (c_1', c_2'), we have Eq. (2.24) where the mixing matrix, $\mathcal{C}^{q\bar{q}\to q\bar{q}}$, is given by, at one-loop order,

$$\mathcal{C}^{q\bar{q}\to q\bar{q}} = \begin{pmatrix} C_F\beta & \frac{C_F}{2N_c}(\alpha+\gamma) \\ \alpha+\gamma & C_F\alpha - \frac{1}{2N_c}(\alpha+\beta+2\gamma) \end{pmatrix} . \tag{2.34}$$

This matrix describes how the color tensors and the corresponding loop integrals mix under one-loop corrections for a soft gluon gluon exchange. The mixing matrix for the other quark process, $qq \to qq$, can be calculated in a similar way, and given by [36]

$$\mathcal{C}^{qq\to qq} = \begin{pmatrix} C_F\beta & \frac{C_F}{2N_c}(\alpha+\gamma) \\ \alpha+\gamma & C_F\gamma - \frac{1}{2N_c}(2\alpha+\beta+\gamma) \end{pmatrix} , \tag{2.35}$$

in the $t-$channel basis for this process

$$\begin{aligned} c_{1\{r_f\}} &= \delta_{r_A r_1}\delta_{r_B r_2} , \\ c_{2\{r_f\}} &= \frac{1}{2}\left(\delta_{r_A r_2}\delta_{r_B r_1} - \frac{1}{N_c}\delta_{r_A r_1}\delta_{r_B r_2}\right) . \end{aligned} \tag{2.36}$$

We close this section with a few words relating our discussion to Monte Carlo (MC) event generators. Showering mechanisms for soft emissions away from jets in MC simulations are based on successive gluon emissions ordered in energies or transverse momenta. The summation of this showering beyond one-loop order is based on the color space that is leading in the large N_c limit [37]. In this way, the result of showering can be written in an evolution form of scalar quantities rather than matrices. To describe a full picture for color flows in parton showering models, the construction of short distance functions in the above matrix form would be essential. This correct picture would be

not only very helpful for the study of underlying events in hadronic collisions but also useful for identifying the SM gauge content of heavy resonances in BSM, which we will study in Chap. 5.

Chapter 3

Substructure of High-p_T Jets at the LHC

3.1 Introduction

At the Large Hadron Collider (LHC), events with highly-boosted massive particles, tops [38], W, Z and Higgs [39] may be the key ingredient for the discovery of physics beyond the standard model [40–42]. In many decay channels, these particles would be identified as high-p_T jets, and any such signal of definite mass must be disentangled from a large background of light-parton ("QCD") jets with a continuous distribution. This background far exceeds such signals, and relying solely on jet mass as a way to reject QCD background from signal would probably not suffice in most cases [26], even using a narrow window for dijets in the search for massive particles such as tops, produced in pairs.

In this chapter, we argue that for massive, high-p_T jets, infrared (IR) safe observables may offer an additional tool to distinguish heavy particle decays from QCD background, perhaps even on an event-by-event basis. We will refer to inclusive observables dependent on energy flow within individual jets as *jet shapes*. A jet within a cone of radius 0.4, for example, may be identified from the energy recorded in roughly fifty 0.1×0.1 calorimeter towers. It thus contains a great deal of information. Perturbatively-calculable, infrared safe jet shapes combined, of course, with IR-safe jet finding algorithms [43–46], may enable us to access that information systematically, and to form a bridge

between event generator output and direct theory predictions.

Essentially, any observable that is a smooth functional of the distribution of energy flow among the cells defines an IR-safe jet shape [47]. The jet mass is one example, but a single jet may be analyzed according to a variety of shapes. In particular, the jet mass distribution has large corrections when the ratio of the jet mass to jet energy is small [48], but can be computed at fixed order when the logarithm of that ratio has an absolute value of order unity. Once the jet mass is fixed at a high scale, a large class of other jet shapes becomes perturbatively calculable with nominally small corrections. Indeed, a jet whose mass exceeds $\mathcal{O}(100\,\mathrm{GeV})$ becomes, from the point of view of perturbation theory, much like the final state in leptonic annihilation at a similar scale. At such energies, event shapes, which in the terminology of this chapter are jet shapes extended over all particles, have been extensively studied in perturbation theory [49]. In this study we explore the possibility that perturbative predictions for jet shapes differ between those jets that originate from the decay of heavy particles, and those which result from the showering of light quarks and gluons. Very interesting related studies have recently appeared in [41, 50, 51].

3.2 Jet shapes and jet substructure

We would like to identify jet shapes for which perturbative predictions differ significantly between QCD and other high-p_T jets, focusing on relatively narrow windows in jet mass. In paper [26] we have discussed how to calculate the jet mass distribution for the QCD background. We now extend this argument to the computation of other jet shape observables.

We emphasize that, because the observables under consideration are IR-safe, we may calculate them as power series in α_s, starting at first order for the QCD background, and zeroth order for an electroweak decay signal.

Our approximation for the jet cross sections is based on factorization for the relatively-collinear partons that form a jet from the remainder of the process [48]. For a jet of cone size R, contributions that do not vanish as a power of R are generated by a function that depends only on the flavor of the parent parton, its transverse momentum, and the factorization scale. Denoting a jet

shape by e, we then have,

$$\frac{d\sigma}{dm_J\, de} = \sum_c \int_{{p_T}^{min}}^{\infty} dp_T \frac{d\hat{\sigma}_c(p_T)}{dp_T} \, \frac{dJ_c(e, m_J, p_T, R)}{de} \,, \tag{3.1}$$

where $d\hat{\sigma}/dp_T$ includes the hard scattering and the parton distributions of the incoming hadrons, and where the jet function for partons c in the final state is defined formally as in Refs. [26, 36].

In Ref. [26], we have found that the distribution of QCD jet masses in the range of hundreds of GeV is fairly well described by the jet function in Eq. (3.1) at order α_s, based on two-body final states. It thus seems natural to anticipate that for QCD jets, energy flow inside the cone would produce a *linear* deposition in the detector [41, 42, 50–52]. While this is certainly the case for an event consisting of two sub-jets, it is a simpler condition, and more easily quantified. Indeed, such a linear flow should also characterize jets from the two-body decay of a highly-boosted, massive particle. We will see below that relatively simple jet shapes can help distinguish QCD jets from many top-decay jets that involve three-body decay. We will also see that jet shapes can help separate samples that contain both QCD jets and jets from two-body decays, such as those of the W, Z or Higgs. We emphasize that a single event may be analyzed by a variety of jet shapes, so that the resolution associated with each one need not be dramatic, so long as they are effectively independent.

3.3 Top decay and planar flow

The linear flow of QCD jets at leading order should be compared with a $\geq$ 3-body decay where the energy deposition tends to be *planar*, covering a two-dimensional region of the detector. An IR-safe jet shape, which we denote as *planar flow*, a two-dimensional version of the "D parameter" [53–56], distinguishes planar from linear configurations. The utility of a closely-related observable was emphasized in Ref. [51].

Planar flow is defined as follows. We first construct for a given jet a matrix I_ω as

$$I_\omega^{kl} = \frac{1}{m_J} \sum_i \omega_i \frac{p_{i,k}}{\omega_i} \, \frac{p_{i,l}}{\omega_i} \,, \tag{3.2}$$

where m_J is the jet mass, ω_i is the energy of particle i in the jet, and $p_{i,k}$ is the k^{th} component of its transverse momentum relative to the axis of the jet's momentum. Given I_ω, we define Pf for that jet as

$$Pf = \frac{4\det(I_\omega)}{\mathrm{tr}(I_\omega)^2} = \frac{4\lambda_1\lambda_2}{(\lambda_1+\lambda_2)^2}\,, \tag{3.3}$$

where $\lambda_{1,2}$ are the eigenvalues of I_ω. Pf vanishes for linear shapes and approaches unity for isotropic depositions of energy.

Jets with pure two-body kinematics have a differential jet function fixed at zero planar flow,

$$\frac{1}{J}\left(\frac{dJ}{dPf}\right)_{\text{2body}} = \delta(Pf)\,. \tag{3.4}$$

This would apply to leading order for events with highly boosted weak gauge boson, Higgs and QCD jets. On the other hand, events that are characterized by $\geq$ 3-body kinematics have a smooth distribution.

Realistic QCD jets have, of course, nonzero Pf. Because Pf is an IR safe observable, however, its average value can depend only on the hard momentum scales of the jet, that is, m_J and p_T. This suggests an average Pf of order $\alpha_s(m_J) \sim 0.1$ for high jet masses, times at most logarithms that are order unity for these heavy jets. Correspondingly, higher order corrections should, by analogy to two-jet event shapes [49], replace the delta function of Eq. (3.4) with a differential distribution that peaks near the origin and then falls off. For jets resulting from three-body decay, on the other hand, we anticipate that corrections in α_s shift the already-smooth distribution modestly, without affecting its overall shape. Finally, for the vast majority of high-p_T QCD jets, with masses $m_J \ll p_T$, planar flow corrections associated with multi-gluon emission may be expected to be large, and to shift Pf to order unity. These considerations are confirmed in Fig. 3.1, where we show the Pf distribution for QCD jet and hadronic $t\bar{t}$ events, for $R = 0.4$, $p_T = 1000\,\mathrm{GeV}$ and $m_J = 140 - 210\,\mathrm{GeV}$ as obtained from MadGraph [57] and Sherpa [58] with jet reconstruction via (the IR-safe algorithm) SISCone [45].

We see that QCD jets peak around small values of Pf, while the top jet events are more dispersed. A planar flow cut around 0.5 would clearly remove a considerably larger proportion of QCD jets than top jets. Figure 3.1 also shows that if we do not impose these mass cuts, for the QCD jets planar flow

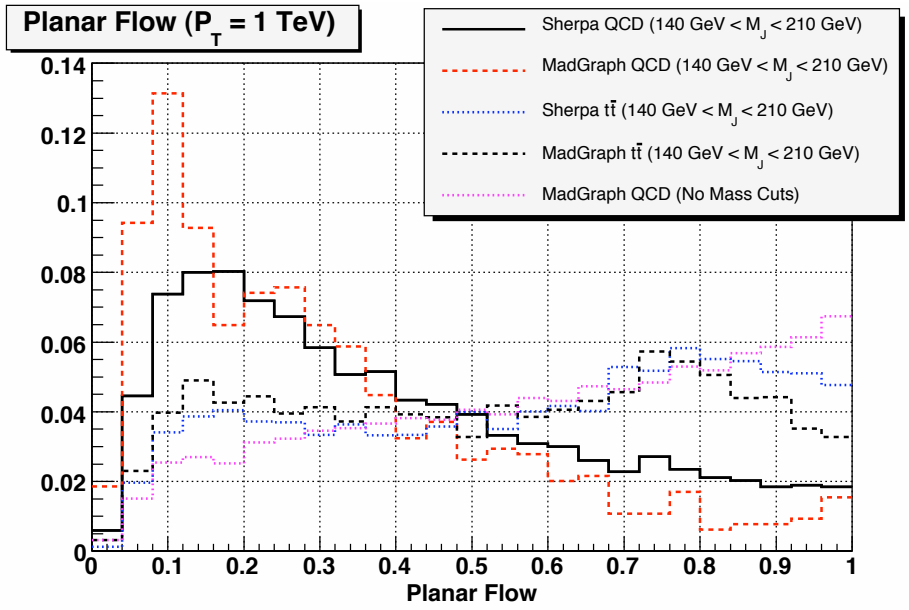

Figure 3.1: The planar flow distribution for QCD and top jets obtained from MadGraph and Sherpa. Distributions are normalized to the same area.

becomes larger and almost indistinguishable from that of top jets.

3.4 Two-body decay

While planar flow can help enrich samples with characteristically three- and higher-body kinematics, other jet shapes can also provide additional information on events with relatively low Pf. Here, we will still wish to distinguish the QCD background from highly boosted electroweak gauge bosons or Higgs [52] as well as from top jets whose Pf happens to be relatively low. We begin with jets that are linear at lowest order, and identify a set of jet shapes that have some power to distinguish between the two. Fixing p_T, R and m_J leaves only one free parameter to characterize the shape.

The QCD jet function for two-body kinematics is defined as a matrix element in [26] and is readily expressed as an integral over θ_s, the angle of the softer particle relative to the jet momentum axis. For a quark jet, for example,

the integrand is therefore the differential jet function,

$$\begin{aligned}\frac{dJ^{QCD}}{d(c\theta_s)} &= \frac{\alpha_s C_F \beta_z z^2}{4\pi m_J^2 (1-\beta_z c\theta_s)(2(1-\beta_z c\theta_s)-z^2)} \\ &\times\left[\frac{(2(1+\beta_z)(1-\beta_z c\theta_s)-z^2(1+c\theta_s))^2}{z^2(1+c\theta_s)(1-\beta_z c\theta_s)}+3(1+\beta_z)\right. \\ &\left.+\frac{z^4(1+c\theta_s)^2}{(1-\beta_z c\theta_s)(2(1+\beta_z)(1-\beta_z c\theta_s)-z^2(1+c\theta_s))}\right], \quad (3.5)\end{aligned}$$

where $z \equiv m_J/p_T$, $\beta_z \equiv \sqrt{1-z^2}$ and $c\theta_s \equiv \cos\theta_s$. The jet mass function, for a jet cone of size R, is found by the integral

$$J(R,z) = \int_{\theta_m}^{R} d\theta_s \left(\frac{dJ}{d\theta_s}\right), \quad (3.6)$$

where $\theta_m = \cos^{-1}\left(\sqrt{1-z^2}\right)$ is the minimum angle the softer particle can make with the jet axis. At $\theta_s = \theta_m$, both particles have the same energy and angle to the jet axis.

It is natural to ask how the integrated jet function, Eq. (3.6) depends of the jet algorithm used to define the jet, and in particular how results for cone jets compare to results when jets are identified by k_t or the newer "anti-k_t" algorithms [44, 46]. For the low orders and small cones discussed here, this relationship is straightforward.

Reference [46] introduces a class of k_t algorithms, for which two particles are within the same jet if their distance d_{ij} is less than d_B, given by

$$d_{ij} = \min(k_{T,i}^{2p}, k_{T,j}^{2p})\frac{r_{ij}^2}{R_{k_t}^2}, \quad (3.7)$$

$$d_B = \min(k_{T,i}^{2p}, k_{T,j}^{2p}), \quad (3.8)$$

where $r_{ij} = \sqrt{\Delta\eta^2 + \Delta\phi^2}$ is the distance between particles i and j in the rapidity-azimuthal angle plane. The choice $p = 1$ defines a standard k_t algorithm, and $p = -1$ the anti-k_t. For small cones, $r_{ij} \approx \theta_{ij}$, where θ_{ij} is the angle between two particles. At lowest order, that is for two particles in the final state, for both positive and negative values of p, these algorithms constrain

r_{ij}^2, and therefore θ_{ij}, by

$$0 < \frac{r_{ij}^2}{R_{k_t}^2} < 1\,. \tag{3.9}$$

As in Eq. (3.6) the energy and angles of the massless two particles are related at fixed jet mass and fixed transverse momentum, through

$$\begin{aligned} m_J^2 &= 2k_{T,i}k_{T,j}(\cosh\Delta\eta - \cos\Delta\phi) \\ &\approx k_{T,i}k_{T,j}\left((\Delta\eta)^2 + (\Delta\phi)^2\right)\,, \end{aligned} \tag{3.10}$$

where again we assume small angles. Changing variables from θ_s to r_{ij}, or equivalently θ_{ij}, is straightforward, and the basic integral for an inclusive jet function in Eq. (3.6) is of the same form for a cone and a k_t (or anti-k_t) jet at lowest nontrivial order. At this order the difference is that in k_t algorithms the parameter R_{k_t} directly restricts the distance between the two particles, in contrast to a cone size R, which restricts the distance of each particle to the jet axis. The only difference is in the upper limit of Eq. (3.6). The integral found with a cone jet of size R corresponds to a generalized k_t algorithm with parameter $R_{k_t}(R)$. Their relation can be easily found from the dependence of r_{ij} in θ_s,

$$\begin{aligned} R_{k_t}(R) &= R + \sin^{-1}\left(\frac{z^2\sin R}{(1+\beta_z^2) - 2\beta_z\cos R}\right) \\ &= R + \frac{z^2}{2}\frac{\sin R}{1-\cos R} + \mathcal{O}(z^4)\,, \end{aligned} \tag{3.11}$$

a result that depends on z, the ratio of the jet energy to its mass. We see that for highly boosted heavy jets, or for jets of low mass, with $z \ll 1$, $R_{k_t}(R) \to R$, and the two integrated jet functions are identical. The k_t algorithm parameter, R_{k_t}, approaches the cone jet parameter, R, from above because the k_t algorithm is slightly more restrictive at this order. For the remainder of our discussion, we shall assume a cone jet algorithm.

For signal events from highly-boosted massive gauge bosons, we consider

separately the cases when it is longitudinal and when it has helicity ($h = \pm 1$),

$$\begin{aligned} \frac{dJ^{\text{Long}}}{d(c\theta_s)} &= \frac{C}{(1-\beta_z c\theta_s)^2}\,, \\ \frac{dJ^{h=\pm 1}}{d(c\theta_s)} &= \frac{C}{(1-\beta_z c\theta_s)^2}\left(1 - \frac{(zs\theta_s)^2}{2(1-\beta_z c\theta_s)^2}\right), \end{aligned} \tag{3.12}$$

where $s\theta_s \equiv \sin\theta_s$ and C is a proportionality coefficient, totally determined from the two-body decay kinematics. We can interpret the appropriately normalized differential jet functions, $P^x(\theta_s) = (dJ^x/d\theta_s)/J^x$ as the probability to find the softer particle at an angle between θ_s and $\theta_s + \delta\theta_s$. As the ratio z decreases, the decay products become boosted and the cone shrinks. For QCD jets from light partons, however, this shrinkage is much less pronounced. From Fig. 3.2 we can see that the jet functions for the gauge boson distributions of Eq. (3.12) fall off with θ_s faster than do QCD jets, Eq. (3.5). This observation suggests that the signal (vector boson-jet) and background (QCD jets) have different shapes for fixed p_T, R and jet mass. This may be used to obtain an improved rejection power against background events. We now consider a class of jet shapes, *angularities*, originally introduced in Refs. [36, 59] for two-jet events in e^+e^- annihilation. A natural generalization of these jet shapes to single-cone jets of large mass m_J is

$$\tilde{\tau}_a(R, p_T) = \frac{1}{m_J}\sum_{i\in jet}\omega_i \,\sin^a\left(\frac{\pi\theta_i}{2R}\right)\left[1 - \cos\left(\frac{\pi\theta_i}{2R}\right)\right]^{1-a}\,, \tag{3.13}$$

with m_J the jet mass. The arguments of the trigonometric functions vary from zero to $\pi/2$ as θ increases from zero to R, that is, over the size of the cone. These weights revert to the angularities as defined in for leptonic annihilation in [36, 59] when $R = \pi/2$, so that the cone is enlarged to a hemisphere and m_J is replaced by the center-of-mass energy in a two-jet event. For massive jets, the angularities are clearly non-zero at lowest order, in contrast to the lowest order planar flow, Eq. (3.4). Then, precisely because of their IR safety, higher-order corrections to the τ_a distributions should be moderate.

As the parameter a varies, the angularities give more or less weight to particles at the edge of the cone compared to those near the center. From the differential jet distribution functions in Eqs. (3.5) and (3.12) and the definition

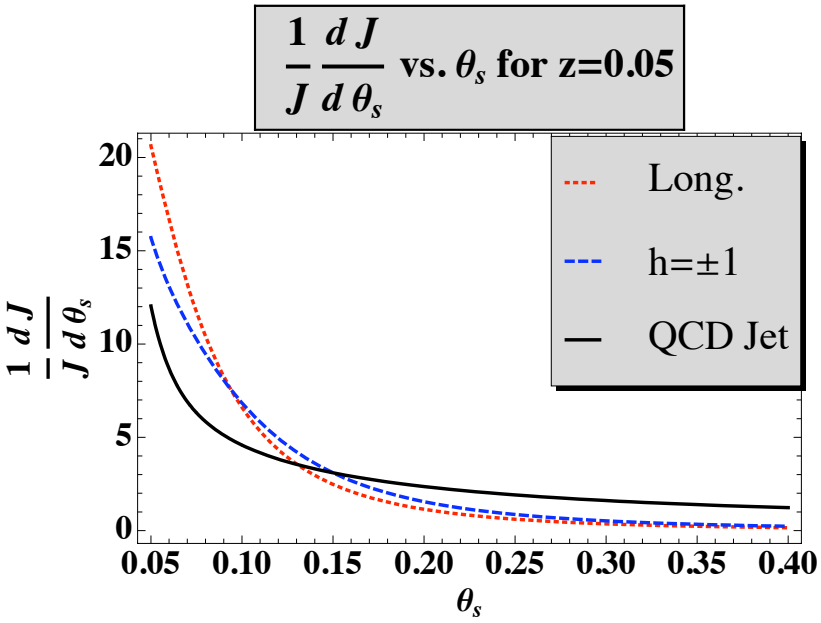

Figure 3.2: Normalized jet distributions for gauge bosons, in Eq. (3.12), and QCD in Eq. (3.5).

of $\tilde{\tau}_a$ we can obtain expressions for $P^x(\tilde{\tau}_a)$ [as before x= sig (signal) or QCD], the probability to find a jet with an angularity value between $\tilde{\tau}_a$ and $\tilde{\tau}_a + \delta\tilde{\tau}_a$ at fixed p_T, R, m_J and a. Our focus is not on the form of the individual distributions but rather on the ratio of the signal to background

$$R(\tilde{\tau}_a) = \frac{P^{\rm sig}(\tilde{\tau}_a)}{P^{\rm QCD}(\tilde{\tau}_a)} \,. \tag{3.14}$$

In Fig. 3.3 we show $R^{\tilde{\tau}_a}$ for $a = -2$ and $z = 0.05$, for the different vector boson polarizations. In Fig. 3.4 we show the corresponding angularity distributions at the event generator level, comparing the output of MadGraph for longitudinal Z boson production to QCD jets in the same mass window. The pattern suggested by the lowest-order prediction of Fig. 3.3 is confirmed by the output of the event generator, with signal and data curves crossing in Fig. 3.3 near $\tilde{\tau}_{-2} = 0.02$, where $R(\tilde{\tau}_{-2}) \sim 1$. Comparing Eqs. (3.5) and (3.12), we observe that the QCD jet distribution is more peaked as $\theta_s \to \theta_m$ than the Z boson jet, corresponding to a sharper falloff with increasing $\tilde{\tau}_{-2}$. In this case, $\theta_m \sim 4 \times 10^{-3}$, and the maximum of the lowest-order angularity distribution would

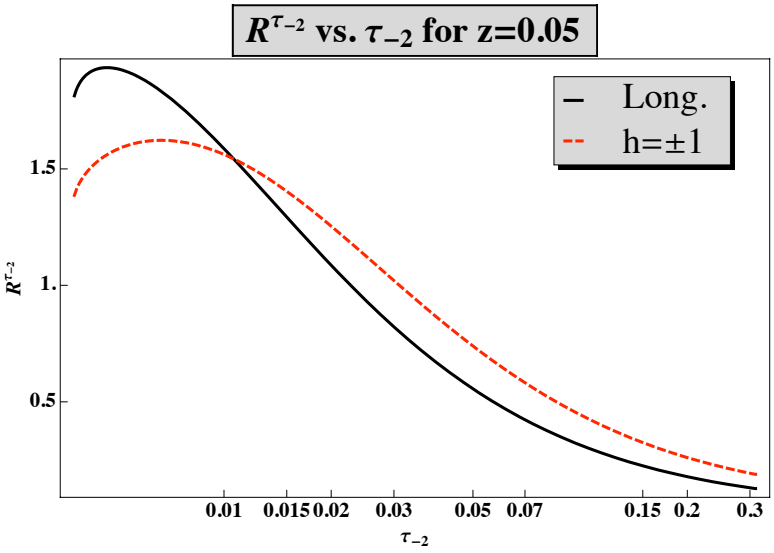

Figure 3.3: The ratio between the signal and background probabilities to have jet angularity $\tilde{\tau}_{-2}$, $R^{\tilde{\tau}_{-2}}$.

be in the lowest bin of the figure. In the event generator output, we see a slight shift to the right for the QCD distribution, due to radiation. This, however, does not affect the clear contrast between the QCD and Z boson cases.

3.5 Linear three-body decay

The leading-order differential top jet function can be obtained by considering its three-body decay kinematics. The analytic expression is similar to Eq. (3.12) for the two-body case, although a bit more elaborate. In the following we simply point out a few features that may help angularities to distinguish top jets from background, even when they have relatively linear flow.

The lowest-order three-body distribution is fully characterized by three angles. The first, θ_b, is the angle between the b quark and the jet axis. The second, θ_{Wq}, is the angle of the quark (from W-decay) relative to the W. The third, ϕ, is the angle of the same quark relative to the plane defined by the W and the b. For an on-shell W, the distributions peak around $\theta_b = \theta_m$ (as in two-body kinematics) and $\theta_{Wq} = \theta_{m(W)}$ the minimal angle relative to the W momenta in the W rest frame. Because it is massive, the W's decay

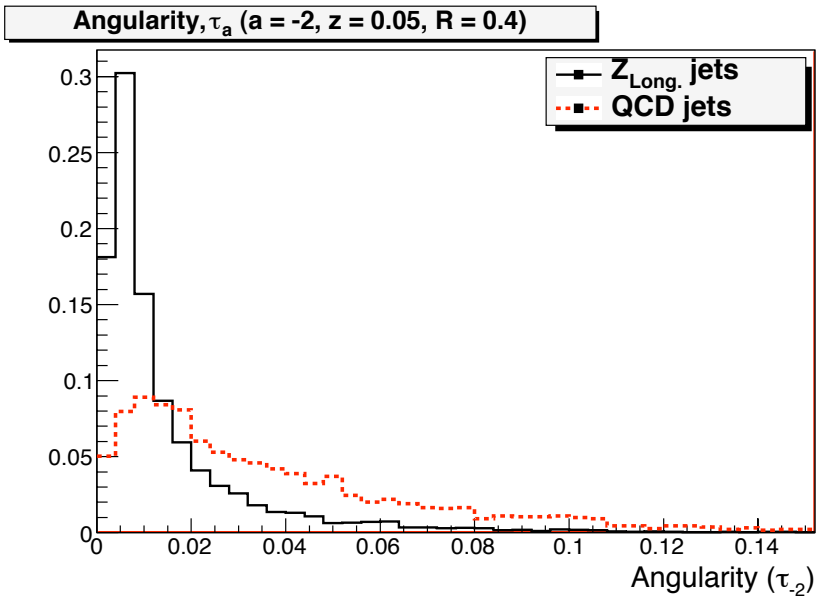

Figure 3.4: The angularity distribution for QCD (red-dashed curve) and longitudinal Z (black-solid curve) jets obtained from MadGraph. Both distributions are normalized to the same area.

products move in somewhat different directions, even in the boosted frame, and their relative orientation induces the ϕ-dependence. Clearly, planar flow has maxima for odd multiples of $\phi = \pi/2$, and vanishes at lowest order at multiples of π. To tag top events at zero planar flow, angularities can be of use. In Fig. 3.5 we plot $\tilde{\tau}_{-5}$ as a function of the azimuthal angle of the $W(q\bar{q})$ pair, ϕ, for a typical top jet event. We also show the corresponding value for the two-body case (clearly ϕ independent). For illustration we choose the kinematical configuration that maximizes the corresponding differential jet distributions. We notice that this top angularity has maxima with ϕ at zero and π at values far above the most likely two-body configuration. The reason is simply that angularities with large negative values of a tend to emphasize flow at the edge of the cone. Other values of a weight individual jets differently in general. We consider this simple plot, along with the forgoing examples from event generators, as strong evidence for the potential of jet shape analysis.

In summary, planar flow, angularities, and jet shapes that are as yet to be invented, may afford a variety of tools with which to distinguish the quantum mechanical histories of jets, whether resulting from heavy particle decay, or

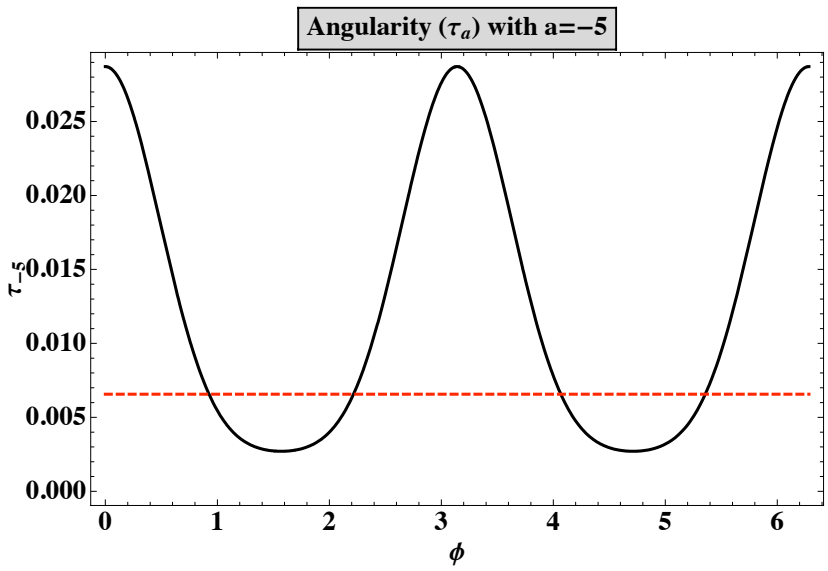

Figure 3.5: Angularity, $\tilde{\tau}_{-5}$ as a function of the azimuthal angle of the $W(q\bar{q})$ pair, ϕ_q, for a typical top jet event, compared to the typical case two-body kinematics.

strong interactions. Our approach is complementary to others that have been proposed recently [41, 42, 50, 51]. For the most part, these references analyze a subclass of highly boosted tops that are not fully collimated as seen for a specific choice of jet-finder. Efficiencies for these event may then be quite high. Here, we take a less exclusive approach, accepting all data in a given mass range. This enables us to readily identify analytic approximations inspired by factorization. As demonstrated in this chapter and its companion [26], our treatment allows one to have fairly straightforward theoretical control over the expected observed distributions. This allows us to interpret the data (only from Monte-Carlo at this point) in the light of simple predictions that are based directly on theory.

Chapter 4

Top Quark Jets at the LHC

4.1 Introduction

The Large Hadron Collider (LHC) is expected to uncover some of the most interesting mysteries of nature. We expect to probe the underlying principles of electroweak symmetry breaking (EWSB) and what stabilizes the weak scale against radiative corrections from unknown microscopic dynamics. Due to its large mass, the top quark induces the most severe contributions to the Higgs quadratic divergence. Furthermore, in almost every known natural model of EWSB, the top sector plays a crucial role in breaking the EW symmetry. Thus, the top sector might hold a key to a new physics (NP) discovery. Many interesting models of EWSB predict new particles with mass $\sim$ TeV scale. In several known examples, the new particles decay into highly boosted top quark pairs ($pp \to X \to t\bar{t}$), or other decay chains containing a single top quark ($pp \to X \to t\,Y$). In addition, the Standard Model (SM) predicts that the LHC will produce more than 10^5 top quarks with $p_T \geq 1\,\text{TeV}$, significantly enhancing our ability to study high p_T tops and resolving beyond the SM dynamics.

Top quarks decay dominantly into hadronic final states ($t \to bW \to bq\bar{q}$) with a branching ratio $\sim 2/3$, providing potentially enhanced statistics. In the present work, we focus on highly boosted top quarks (decaying through the hadronic channel), and on the dominant QCD jet background. We refer to a top quark that decays hadronically as a *hadronic top*. For moderately boosted top quarks ($p_T \sim 500$ GeV), conventional top quark reconstruction meth-

ods, which exploit the decay chain topology, remain adequately efficient (see *e.g.* [60]). As the top quark p_T approaches 1 TeV, the situation significantly changes [41, 61–64].[5] The average separation of the top quark decay products approaches the limits of reliable jet reconstruction (cone size $R \sim 0.4$), and starts to encroach upon the detector resolution ($R \sim 0.1$). As a result, the efficiency of conventional reconstruction methods drops quickly. The performance of b-tagging and light jet rejection is expected to drop substantially in this kinematic regime. At present, there is very little published data on b-tagging at $p_T \sim 1$ TeV [65]. We perform our analysis without accounting for the possible benefits of b-jet identification.[6]

We turn our focus away from this family of "conventional" reconstruction methods. We examine the situation where the decay products of at least one top quark are reconstructed as a single jet, or *top-jet*. In semileptonic $t\bar{t}$ events, for example, the leptonic top may still be reconstructed via semi-conventional reconstruction methods, giving up on lepton isolation cuts [61], see also [63, 66]. These methods call for further extensive study due to expected reducible backgrounds and uncertainties related to the ability to measure the collimated semi-leptonic top mass (dileptonic $t\bar{t}$ events are also analyzed in [67]). Hadronic top, on the other hand, will give rise to a top-jet. There will still be some small, but non-negligible, number of $t\bar{t}$ events where one of the top quarks reconstructs as a top-jet, but the other top quark can be reconstructed via conventional methods (or semi-conventional methods where one of the tops is manifested as a two-jet object). In this chapter, we focus on the top-jet itself as a means of identifying $t\bar{t}$ events. The main reasoning behind that is as follows:

(i) We find that for $p_T > 1$ TeV the majority of hadronic-tops are manifested as top-jets, even for cone size as small as $R = 0.4$. Thus, it is clear that our tools will be applicable for a wide range of top momenta.

(ii) The distributions and shapes of both background and signal can be understood via first principle calculations as shown in this study and in

[5] For earlier works in the case of boosted EW bosons see also [42].

[6] The possibility of b-tagging jets, when the top quark reconstructs to 2 (or more) jets, one of which has a mass $\sim m_W$ and the sum of the two jets has a mass $\sim m_t$, is outside the main focus of this chapter.

Ref. [25]. It may allow for a cleaner analysis, in the sense that a more direct contact between actual data (expected to arrive soon) and the microscopical theory can be made.

Apart from substructure, to leading order, top jets provide four pieces of information, namely its energy, two angles and mass (just as any QCD jet, ignoring the possibility of b-tagging). Without a mass cut, the QCD jet background swamps the hadronic top signal by orders of magnitude. The most basic tagging method after giving up conventional methods is to use the jet mass as a discriminator between the QCD background and the hadronic top signal; the high-p_T top-jet mass distribution should peak around the top mass while the QCD jet mass distribution peaks near zero. However, using a jet mass as a discriminator is more complicated for several reasons. Due to radiation, QCD jets acquire a large tail in the mass distribution. The cross section for acquiring large jet mass, for example near the top mass, increases substantially with p_T and cone size. Top-jets also broaden due to radiation, hardening their jet mass distribution.[7] Furthermore, a finite jet reconstruction cone size will not always capture all the daughters of the top quark decay chain, thus softening its mass distribution. The net effect is a smearing of the expected naive, broadened, Breit-Wigner distribution for the top jet mass distribution. Detector effects further smear the distribution, making the above idealized description unrealistic.

Nevertheless, jet mass cuts should retain some rejection power against the QCD background [69–71]. Our study addresses this issue in both quantitative and qualitative manner, by considering the experimental and theoretical aspects of the analysis. On the theoretical front, based on a factorization approach, we derive a simple approximation for the shape of the QCD jet mass spectrum. We demonstrate that there is good agreement between our simple analytic predictions and Monte Carlo (MC) results. We are able to compute from first principle various features related to a jet mass cut. We evaluate its significance in the form of a semi-analytical expression for the rejection power and show that it is independent of pseudorapidity. We provide a quantitative study of the distribution of the signal and background, via MadGraph/MadEvent [72–74](MG/ME) and Sherpa [75]. We consider the de-

[7]For a detailed recent study see [68] and references therein.

tector resolution by using transfer functions [76], smearing jets according to a profile obtained from full Geant4 Atlas simulation. Transfer functions provide a versatile mechanism to explore such effects as shifts in jet energy scale (JES), etc.

We apply the results of our studies to analyze boosted SM top quark pair production, an important discovery channel for NP [61–63, 66, 77–81]. To put results into perspective, we use both $25\,\mathrm{fb}^{-1}$ and $100\,\mathrm{fb}^{-1}$ of integrated luminosity as reference luminosities. At this time, these correspond to many years of data taking. We show that using single- and double-tagging methods with our jet functions (defined below) to analyze jet mass distributions, we can significantly separate the Standard Model $t\bar{t}$ signal from the QCD background. Our theoretical QCD jet mass distributions can efficiently characterize the background via sideband analyses. With 25 fb^{-1} of data, our approach allows us to resolve 1 TeV top-jets from the QCD background, and about 1.5 TeV top-jets with 100 fb^{-1}, if we exploit the kinematics of the so-called "away" side of the event, without relying on b-tagging. The essence of the away side mass cut is that it preferentially keeps the $t\bar{t}$ signal over the background. We analyze the mass distribution in more detailed manner, as simple counting methods are inadequate. As described above, the $t\bar{t}$ signal is expected to exhibit pronounced structure near the top quark mass. In order to resolve this "peak" against the QCD background, we need to understand the shape of both the $t\bar{t}$ signal and the QCD background. To characterize the background we perform a sideband analysis to reduce contamination by the signal. Our theory-driven ansatz for the QCD background is an admixture of quark- and gluon-jet functions, the coefficients of which we analyze by fitting in the sidebands (outside the top mass window). We interpolate the results of the fit into the top mass window ($140\,\mathrm{GeV} \leq m_J \leq 210\,\mathrm{GeV}$). Armed with *shapes* for the signal and background, we fit them into the data to obtain the normalization constants. These normalization constants are the magnitude of the signal and background. The errors associated with the normalization provides a measure of the significance of the measurement.

To further improve the significance we consider jet shapes [25], which resolve substructure of energy flow inside cone jets. In a companion paper [25], we explore the possibility that, requiring a large jet mass, perturbative predic-

tions for jet shapes differ between jets that originate from the decay of heavy particles, and those which result from the showering of light quarks and gluons. With such additional handles, we might have a chance to distinguish boosted $t\bar{t}$ signal from the QCD background even at a smaller integrated luminosities.[8] We discuss jet substructure later in the text.

We turn our attention to the use of b-jets as spin analyzers for the top quarks. For highly boosted top quarks, chirality is approximately equal to helicity and is conserved to a good approximation. Information about the top chirality is encoded in the angular distribution of the decay products [61, 83, 84]. Naively, one would argue that for hadronic tops this information is inaccessible due to collimation and the absence of leptons which are known to be good spin analysers [83, 84]. We explore the possibility of using p_T of the b-quark for measuring the top quark polarization, which is important for exploring NP. For this, we explore the case when at least one of the boosted top quark can be resolved into more than two jets. We also consider the possibility of using p_T of the lepton for measuring the top quark polarization for semi-leptonically decaying tops.

This work has two main focal points, namely QCD jet mass distributions and hadronic $t\bar{t}$ signal, and is structured as follows. In the next section, we discuss the MC generation and detector simulation. In section 4.3 we focus on highly boosted QCD jets. The jet mass distribution is examined numerically, via MC methods, and analytically, via jet functions. The salient points of the jet functions are introduced, leaving detailed derivations for the Appendix. Section 4.4 discusses the top-jet signal. In section 4.5, we compare high p_T hadronic $t\bar{t}$ events with QCD jets. In section 4.6 we discuss jet shapes [25], which can be used as additional discriminants against the background. Section 4.7 discusses the hadronic top quark polarization by using the transverse momentum of the bottom quark. We conclude in section 4.8.

[8] There are other approaches dealing with a similar situation in a different perspective in recent literature [50, 51, 64, 82].

4.2 Event simulation

4.2.1 Monte Carlo generation

The Sherpa [75] and MG/ME (version 4) [72, 74] MC generators were used to produce $t\bar{t}$ and QCD jet events, with parameters appropriate to the LHC. To effect partonic level cuts during the generation of QCD jets ($p_T(\geq 1 \text{ parton}) \geq$ 800 GeV), we used customized code provided by the Sherpa authors applicable to Sherpa V1.1.0. For technical reasons, $t\bar{t}$ events were generated using Sherpa version 1.0.9, whereas QCD jet events were generated with Sherpa version 1.1.0. MG/ME interfaces to Pythia V6.4 (for parton shower and fragmentation) [85]. For jet reconstruction, we used SISCone V1.3 [86] for both Sherpa and MG/ME. Cross sections are calculated to leading order. Jets are defined via the cone algorithm [87] with $R = 0.4$ and $R = 0.7$, referred to as C4 and C7, respectively. Jets have $p_T > 50\,\text{GeV}$ and $|\eta| \leq 2$. At the hard scatter level, final state partons are required to have $p_T \geq 20\,\text{GeV}$. For MG/ME events, the final state partons have $|\eta| \leq 4.5$.

We do not account for pile-up effects nor characterize the underlying event. Efficiencies for triggering and reconstruction of jets at these energies are very close to unity; the corrections are negligible and are not considered. The strong coupling constant was allowed to run. Throughout the analysis, we used Sherpa V1.0.9 with CTEQ6M parton distribution functions (PDF) [88]. Comparisons to MG/ME were made whenever appropriate, and also occasionally to Pythia (version 8.1) [37] for $2 \to 2$ process without matching. In such cases, the distinct curves are marked accordingly. The events used in the analysis were inclusive, i.e. $pp \to t\bar{t}(j)$ and $pp \to jj(j)$, with matching (see [89] for a detailed discussion): modified MLM [90] for MG/ME and CKKW [91] for Sherpa.

4.2.2 Cross sections

In table 4.1 we present cross sections for producing final state (hadronic level) jets with $p_T \geq 1\,\text{TeV}$ for the different MC simulations. There are large uncertainties in the cross sections, due to differences between the MLM and CKKW matching, between MC generators, and between PDFs. It is outside the scope

of this chapter to explore the reasons behind these differences.[9] We estimate a 100% systematic uncertainty associated with the $t\bar{t}$ cross section, and a 20% systematic uncertainty in the QCD jet cross section.

Process	Generator	PDF	Matching	Cross Section
$pp \to t\bar{t}(j)$	SHERPA 1.0.9	CTEQ6M	CKKW	135 fb
$pp \to t\bar{t}(j)$	SHERPA 1.1.2	CTEQ6M	CKKW	149 fb
$pp \to t\bar{t}(j)$	MG/ME 4	CTEQ6M	MLM	68 fb
$pp \to t\bar{t}(j)$	MG/ME 4	CTEQ6L	MLM	56 fb
$pp \to t\bar{t}$	Pythia 6.4	CTEQ6L	-	157 fb
$pp \to t\bar{t}$	Pythia 8.1	CTEQ6M	-	174 fb
$pp \to jj(j)$	SHERPA 1.1.0	CTEQ6M	CKKW	10.2 pb
$pp \to jj(j)$	MG/ME 4	CTEQ6L	MLM	8.54 pb
$pp \to jj(j)$	MG/ME 4	CTEQ6M	MLM	9.93 pb
$pp \to jj$	Pythia 6.4	CTEQ6L	-	13.7 pb
$pp \to jj$	Pythia 8.1	CTEQ6M	-	13.3 pb

Table 4.1: Cross sections for producing final state $R = 0.4$ leading cone jets with $p_T \geq 1\,\text{TeV}$ and $|\eta| \leq 2$. Generation level cuts were imposed as follows. Final state partons from the hard scatter were required to have $p_T \geq 20\,\text{GeV}$. For MG/ME, final state partons have $|\eta| \leq 4.5$. Processes with a trailing (j) suffix indicate that $2 \to 2$ and $2 \to 3$ processes are represented.

4.2.3 Modelling detector effects

A transfer function, trained with full ATLAS detector simulation on high p_T jet and high p_T $t\bar{t}$ samples, was used to map particle level jets (Atlas truth jet reconstruction) onto a full simulation model [76]. Transfer functions work by feeding back the differences between the target collection (Full Simulation) and the source collection (Truth Jets). The differences and efficiencies are stored as distributions, in the form of histograms, and binned in p_T and η. We refer to the collection of the smearing distributions as a *transfer function*. It is important to note that transfer functions are applicable on events with similar jet multiplicity and topology. We applied the transfer function (trained on

[9] Sherpa data was generated with an invariant $t\bar{t}$ mass cut greater than 500 GeV; MadGraph was generated with a p_T cut > 700 GeV. The initial-state radiation (ISR) contributions to the cross sections do not significantly affect our analysis, as such jets populate the low mass spectrum.

Atlas truth jets) to SISCone truth jets, which preserve the salient characteristics of the Atlas truth jets. We used the transfer function to effect p_T and mass smearing, but not reconstruction efficiency. At the energies considered in this chapter, reconstruction efficiency is very close to unity. In summary, the results of the transfer function should be viewed simply as realistic detector smearing.

In this chapter, a jet is transferred as follows. The transverse momentum and mass of truth-level jets are smeared according to the appropriate distribution. For the purposes of modeling the effects of the JES, the means of the p_T distributions are shifted accordingly, without cross correlation to the mass smearing. This is a subtle point. Depending on the reconstruction mechanism, reported jet masses may depend proportionally on the JES; a JES shift results in a jet mass shift. In our study of the effects of the JES, we do not make a correlation between the p_T and mass distributions. This effect is much smaller, and such precision is not warranted in these studies.

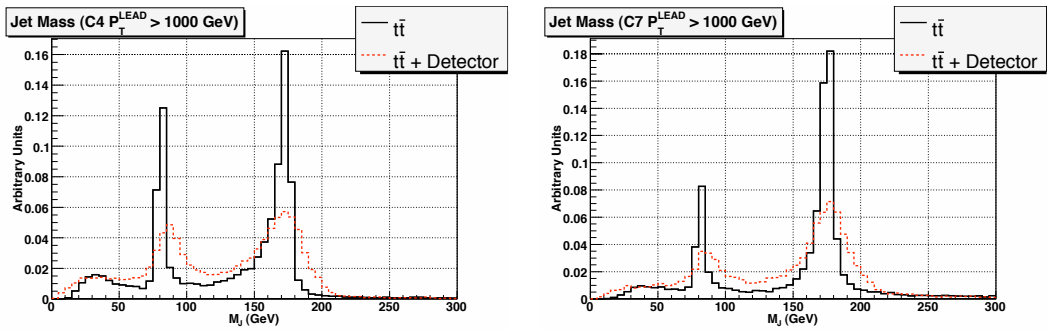

Figure 4.1: We compare the mass distribution of the leading jet (${p_T}^{lead} \geq 1000\,\text{GeV}$) for the $t\bar{t}$ signal with (the red dotted curve) and without (the black solid curve) leading detector effects. The plot on the left corresponds to C4 jets; the plot on the right corresponds to C7 jets.

In Fig. 4.1, we compare the $t\bar{t}$ jet mass distributions for C4 and C7 jets, with and without detector smearing, for ${p_T}^{lead} \geq 1000\,\text{GeV}$. We see, as expected, that due to the finite cone size even the top jet mass distribution is far from the naive Breit-Wigner shape. In cases where the outgoing b quark is outside the cone, we expect that the top jet mass to be peaked around the W mass. In cases where one of the quarks from the W decay is outside the cone we expect a smooth distribution with a typical invariant mass of roughly $m_t/\sqrt{2}$, etc. These effects are present even at the truth level, without detector effects.

The black curve shows a smooth distribution with a spurious peak around the W mass. The red curve demonstrates how the detector effects further smear the top jet mass distribution.

4.3 QCD jet background

If jet mass methods are to be viable, we must be able to characterize the dominant QCD jet background [92]. One of the primary points in this work is that we are able to understand the QCD jet background *analytically* as well as through MC simulations. In this section, we present the summary of our analytic calculations of the QCD jet mass distribution based on the factorization formalism [19, 36], which is presented in the Appendix. We compare our theoretical prediction with simulated MC data. Note that the final states, which induce the jet masses, simulated by MC event generators are much more complicated (due to radiation, showering etc.) than our simple two body final states. Yet, as we shall see, we can consistently describe the simulated MC data.

4.3.1 Analytic prediction

We are interested in looking at the following processes:

$$\begin{aligned} H_a(p_a) + H_b(p_b) &\rightarrow J_1(m^2_{J_1}, p_{1,T}, R) + X\,, \\ H_a(p_a) + H_b(p_b) &\rightarrow J_1(m^2_{J_1}, p_{1,T}, R) + J_2(m^2_{J_2}, p_{2,T}, R) + X\,, \end{aligned} \tag{4.1}$$

where, H_i are the initial hadrons, p_i being the corresponding momenta, and the final states include jets in the direction of the outgoing partons of the underlying process, with a fixed jet mass, m_{J_i}, "cone size" $R^2 = \Delta\eta^2 + \Delta\phi^2$ and tranverse momenta, $p_{i,T}$.

We begin with the factorized hadronic cross section for single inclusive jet processes,

$$\begin{aligned} \frac{d\sigma_{H_A H_B \to J_1 X}(R)}{dp_T dm_J d\eta} &= \sum_{abc} \int dx_a\, dx_b\, \phi_a(x_a)\, \phi_b(x_b) \\ &\quad \times \frac{d\hat{\sigma}_{ab\to cX}}{dp_T dm_J d\eta}(x_a, x_b, p_T, \eta, m_J, R)\,, \end{aligned} \tag{4.2}$$

which in the limit of small R, we can further factorize into (see Appendix B),

$$\begin{aligned}\frac{d\sigma_{H_AH_B\to J_1X}(R)}{dp_T dm_J d\eta} &= \sum_{abc}\int dx_a\, dx_b\, \phi_a(x_a)\, \phi_b(x_b) H_{ab\to cX}(x_a, x_b, p_T, \eta, R) \\ &\quad \times J_1^c(m_J, p_T, R). \end{aligned} \tag{4.3}$$

The factorization and renormalization scales are chosen to be p_T, ϕ_i is the PDF for the initial hadrons, $H_{ab\to cX}$ denotes the perturbative cross section, and J^c denotes jet functions, whose matrix elements are defined in Appendix 4.9 (see *e.g.* [93] for recent reviews and references therein). Furthermore the J^cs are, by definition, normalized as

$$\int dm_J\, J^c = 1\,. \tag{4.4}$$

We have used the fact that the jet functions do not depend on η in the leading expansion (see Appendix 4.9). Therefore, we can write Eq. (4.3) for the hadronic cross section as

$$\frac{d\sigma(R)}{dp_T dm_J} = \sum_c J^c(m_J, p_T, R)\, \frac{d\hat{\sigma}^c(R)}{dp_T}\,, \tag{4.5}$$

where c represents the flavour of the jet, and where

$$\frac{d\hat{\sigma}^c(R)}{dp_T} = \sum_{ab}\int dx_a\, dx_b\, \phi_a\, \phi_b \int d\eta \int dm_J\, \frac{d\hat{\sigma}_{ab\to cX}(R)}{dp_T dm_J d\eta}\,. \tag{4.6}$$

We employ the jet functions given in the Appendix by Eqs. (4.37) and (4.39), for fixed jet mass and R at the next-to-leading order (NLO) with running coupling effects. As we will see below, these results are consistent with the MC data for sufficiently large ($m_J \geq \mathcal{O}(100\,\mathrm{GeV})$) jet masses.

At the lower end of the jet mass spectrum, where $m_J \ll p_T R$, the jet mass distribution is dominated by higher order corrections and non-perturbative physics [93], which are beyond the scope of our work, as our interest lies in the region of high jet mass. We note this causes complications when trying to predict the moments of the mass distributions, such as the mean and RMS, unless we introduce a lower cutoff on the mass.

In the Appendix, we provide the full NLO[2] result for the jet function in term of θ_S, the angle of the softer particle with respect to the jet axis. These exact results can be approximated by the eikonal approximation introduced in Appendix B as

$$\begin{aligned} J^{(eik),c}(m_J, p_T, R) &= \alpha_s(p_T)\frac{4\,C_c}{\pi m_J}\log\left(\frac{1}{z}\tan\left(\frac{R}{2}\right)\sqrt{4-z^2}\right) \\ &\simeq \alpha_s(p_T)\frac{4\,C_c}{\pi m_J}\log\left(\frac{R\,p_T}{m_J}\right), \end{aligned} \tag{4.7}$$

where $\alpha_s(p_T)$ is the strong coupling constant at the appropriate scale, $z = \frac{m_J}{p_T}$, c represents the flavour of the parton which initiated the jet and C_c equals $C_F = 4/3$ for quarks, and $C_A = 3$ for gluons. These expressions agree with the full NLO jet functions to the level of about 1% and 10% for quark and gluon initiated jets in the region of the top mass window, respectively (checked for $R = 0.4$ and 0.7 and $p_T \gtrsim 1\,\text{TeV}$).

We can interpret the jet function as a probability density functions for a jet with a given p_T to acquire a mass between m_J and $m_J + \delta m_J$. Our rather simple treatment is valid for the higher end of the jet mass spectrum (above $m_J \sim \mathcal{O}(100\,\text{GeV})$), where NLO perturbative calculation captures the dominant physics. In Fig. 4.2 we show the gluon jet mass distribution from (4.39) with running (red, dashed), and fixed (blue, dotted) coupling, along with the eikonal jet function (green, dashed-dotted) with fixed coupling. The fixed scales are chosen to be p_T. For reference we also superimpose in the Fig. a $1/m_J$ curve which has the same dimension as that of our jet functions and is roughly of the form of the soft function (*cf* Appendix B). It is remarkable that our theory curves are significantly different from simple $1/m_J$ curve whose normalization is chosen such that this curve overlaps with our theory curves around the top mass. This indicates that logarithmic factor is very important in our theory prediction. Note that at lower masses the running is much harder than the fixed cases since the configurations associated with this mass region have lower k_T (the radiated gluon momenta), leading to a larger α_s. Also, the eikonal approximation is equivalent to a no recoil approximation, thus resulting overall in a harder process than the result in Eq. (4.39) at fixed

[2]Note that what we mean by NLO is "lowest nontrivial order".

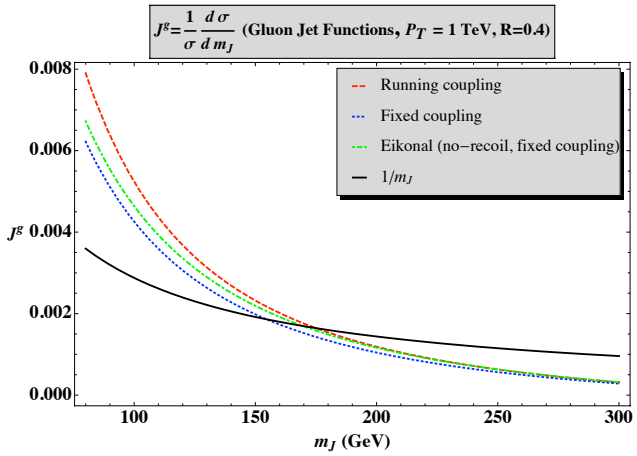

Figure 4.2: Various theoretical gluon-jet mass distributions, along with a $1/m_J$ curve, are plotted for $p_T = 1\,\text{TeV}$ and $R = 0.4$. Plotted are the jet mass distribution from (4.39) with running (red, dashed), and fixed (blue, dotted) coupling, along with the eikonal jet function (green, dashed-dotted) with fixed coupling. For the jet functions with no running the scales were chosen be p_T.

scales.

For the purpose of comparing the mass distributions obtained from jet functions and the MC simulations, Eq. (4.6) can be matched to $(d\sigma^c(R)/dp_T)_{\text{MC}}$ obtained from MC, leading to the following relation,

$$\frac{d\sigma^c_{pred}(R)}{dp_T dm_J} \;=\; J^c\left(m_J, p_T, R\right)\left(\frac{d\sigma^c\left(R\right)}{dp_T}\right)_{\text{MC}}, \tag{4.8}$$

for the prediction of quark and gluon jet mass distribution based on perturbative calculated jet functions, Eqs. (4.37) and (4.39). Note, however, that this would require us to split the MC output in terms of the parton flavours c, which for realistic simulation leads to ambiguities especially when matching is used. Therefore, for our analysis, instead, we use the analytic result to suggest bounds for the "data" distribution from the MC. There is, however, no a posteriori way to determine the flavour which initiated the jet (as with real

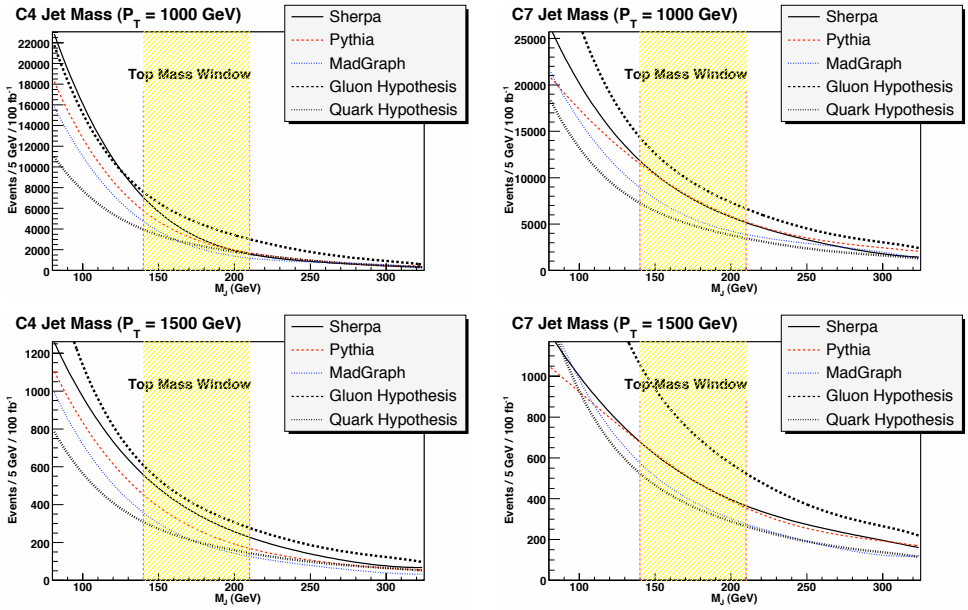

Figure 4.3: The jet mass distributions for Sherpa, Pythia and MG/ME are plotted for different p_T and jet cone sizes. The quark and gluon mass distributions from the jet functions are overlaid, using Eqs. (4.9) and (4.10). The upper left plot corresponds to $950\,\text{GeV} \leq p_T \leq 1050\,\text{GeV}$ and $R = 0.4$. The upper right plot corresponds to $950\,\text{GeV} \leq p_T \leq 1050\,\text{GeV}$ and $R = 0.7$. The lower left plot corresponds to $1450\,\text{GeV} \leq p_T \leq 1550\,\text{GeV}$ and $R = 0.4$. The lower right plot corresponds to $1450\,\text{GeV} \leq p_T \leq 1550\,\text{GeV}$ and $R = 0.7$.

data). Thus, we write

$$\frac{d\sigma_{pred}(R)}{dp_T dm_J}_{\ upper\ bound} = J^g\left(m_J, p_T, R\right) \sum_c \left(\frac{d\sigma^c\left(R\right)}{dp_T}\right)_{\text{MC}}, \tag{4.9}$$

$$\frac{d\sigma_{pred}(R)}{dp_T dm_J}_{\ lower\ bound} = J^q\left(m_J, p_T, R\right) \sum_c \left(\frac{d\sigma^c\left(R\right)}{dp_T}\right)_{\text{MC}}, \tag{4.10}$$

exploiting the fact that $J^g > J^q$ in the region of high jet mass, as can be seen in Eq. (4.8).

4.3.2 Jet function, theory vs. MC data

In this section, we compare a set of theory-based bounds for the jet mass distribution to the mass distribution obtained via MC event generators. This part contains one of our main results, where we demonstrate that our theoretical

predictions are in agreement with the MC data. In Fig. 4.3, we compare the quark and gluon jet mass distributions from Eqs. (4.9) and (4.10) to the distributions from different MC generators (MG/ME, Sherpa and Pythia). We perform this comparison at fixed p_T, since we are interested in the relative shapes of these distributions around the top mass window. Note that above $m_J \sim \mathcal{O}(100\,\text{GeV})$, the *shapes* of three MC distributions are very similar. Sherpa and MG/ME distributions interpolate between the quark jet function (lower bound) and the gluon jet function (upper bound) as expected. For the purposes of comparing shapes, Pythia and MG/ME are rescaled so that their total cross sections agree with Sherpa. This cross section scaling does not affect the predictive quality of the theory curves, since it affects both sides of Eqs. (4.9) and (4.10). The scaling allows us to present the results from the different event generators on a single plot. Note, as mentioned before, that for $m_J \ll p_T R$, higher order corrections will contribute, pushing the distribution down, with a Sudakov-like suppression, which can be seen in the lower mass region for $p_T = 1.5$ TeV and $R = 0.7$.

In a typical experimental setup, a lower cut over p_T will be assumed and the distributions will be integrated above that p_T^{min} cut. Thus we can integrate over the appropriate region on Eq. (4.8), which leads to the analog of Eqs. (4.9) and (4.10) for the p_T-integrated jet mass cross section,

$$\frac{d\sigma^c_{pred}(R)}{dm_J} = \int_{p_T^{min}}^{\infty} dp_T\, J^c\left(m_J, p_T, R\right) \sum_{c'} \left(\frac{d\sigma^{c'}(R)}{dp_T}\right)_{\text{MC}}, \qquad (4.11)$$

where J^c is defined as before. The MC differential cross section is obtained by summing over the contributions from both quark and gluon jets. Therefore, the cross section's shape is characterized by an admixture of quark and gluon jets and should interpolate between the two curves, $c = q$ and g. In Fig. 4.4, we compare leading jet mass distribution for events where the leading jet has $p_T \geq 1\,\text{TeV}$ obtained from Sherpa. The quark and gluon curves, obtained from Eq. (4.11), with use of the jet functions in Eqs. (4.37) and (4.39), correspond to the cases where the lead jets are all quark or gluons jets, respectively.

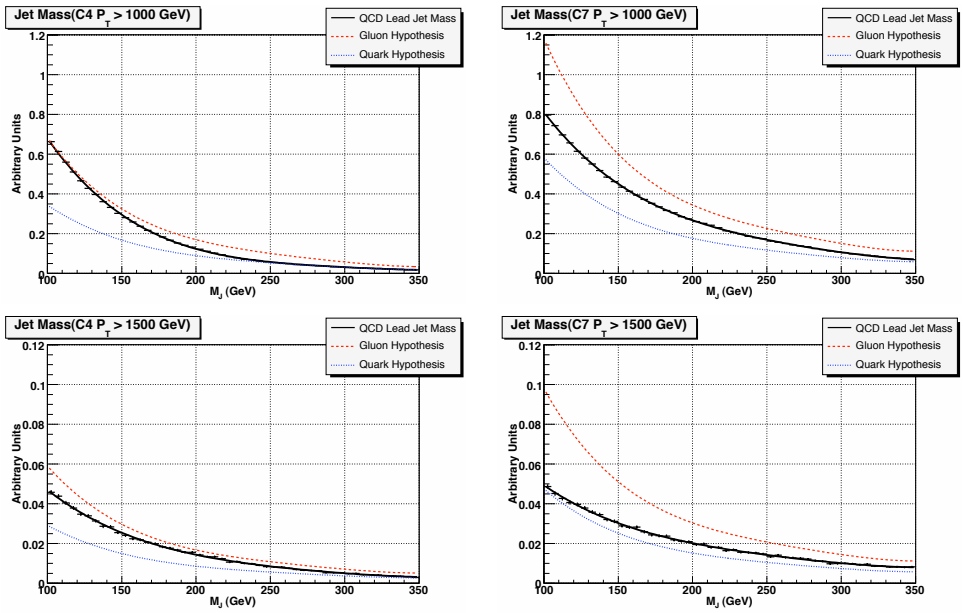

Figure 4.4: Comparison between the theoretical jet mass distributions and MC leading jet mass distribution from Sherpa. The minimum p_T and cone size are indicated on the plots. A gluon (quark) hypothesis is the prediction made if the entire contribution were from gluon (quark) jets (cf Eq. (4.11)).

As before, we find the bounds for the total cross section

$$\sigma(R)_{upper\ bound} = \int_{p_T^{min}}^{\infty} dp_T \sum_c \left(\frac{d\sigma^c(R)}{d\,p_T}\right)_{\rm MC} \times \int_{140\,GeV}^{210\,GeV} J^g(m_J, p_T, R)\, dm_J\,, \tag{4.12}$$

$$\sigma(R)_{lower\ bound} = \int_{p_T^{min}}^{\infty} dp_T \sum_c \left(\frac{d\sigma^c(R)}{d\,p_T}\right)_{\rm MC} \times \int_{140\,GeV}^{210\,GeV} J^q(m_J, p_T, R)\, dm_J\,. \tag{4.13}$$

In table 4.2, we refer to the gluon and quark jets from the results in Eqs. (4.12) and (4.13), respectively. The numbers in the table were calculated as follows. From a MC sample corresponding to 100 fb^{-1} of data, we extracted the number of events with C4 lead jet $p_T \geq 1000(1500)\,\text{GeV}$ and $140\,\text{GeV} < m_J < 210\,\text{GeV}$, the top mass window. We repeated this exercise for C7 jets. The *data* column contains these results.

$p_T{}^{lead}$ cut	Cone Size	Data	Quark hypothesis	Gluon hypothesis
1000 GeV	C4	113749	70701	135682
1000 GeV	C7	197981	131955	260045
1500 GeV	C4	10985	6513	12785
1500 GeV	C7	13993	11164	22469

Table 4.2: Comparison of Sherpa MC data to predictions of pure-quark and pure-gluon hypothesis, for the number of events with leading jet with mass between 140 GeV and 210 GeV. The data is compared to the bounds given in Eqs. (4.12) and (4.13). The statistics reflect 100 fb^{-1} of integrated luminosity.

Fractional fake rate

With the theoretical machinery discussed in the previous section, we are able to make a prediction of the rate at which QCD jets will fake the mass signature of top-jets. We define the fractional fake rate as the fraction of jets with $140\,\text{GeV} \leq m_J \leq 210\,\text{GeV}$, for given p_T and R. We estimate the upper and lower bounds of the fractional fake rate as

$$\int_{140\ GeV}^{210\ GeV} dm_J\, J^q(m_J, p_T, R) \leq \text{ Fractional fake rate } \leq \int_{140\ GeV}^{210\ GeV} dm_J\, J^g(m_J, p_T, R)\,. \tag{4.14}$$

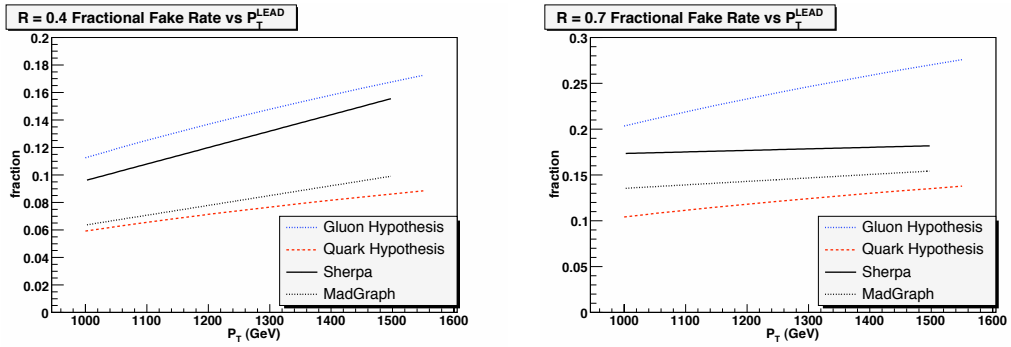

Figure 4.5: The fraction of jets which acquire $140\,\text{GeV} \leq m_J \leq 210\,\text{GeV}$ as a function of the transverse momentum of the leading jet. Quark- and gluon-hypothesis curves yield the prediction for the fractional fake rate, if all jets were either quark- or gluon-jets, respectively. The plot on the left corresponds to C4 jets; the plot on the right corresponds to C7 jets (cf Eq. (4.14)).

In Fig. 4.5, we plot the fractional fake rate as a function of jet transverse momentum. To predict the number of fakes in our sample, we fold the differential cross section for QCD jet production (Fig. 4.6) with the fractional fake rate (Fig. 4.5). Again we expect a Sudakov-like suppression when $m_J \ll p_T R$, thus flatting the theoretical fractional fake rate as p_T increases. This can be seen more predominately for $R = 0.7$ in Fig. 4.5.

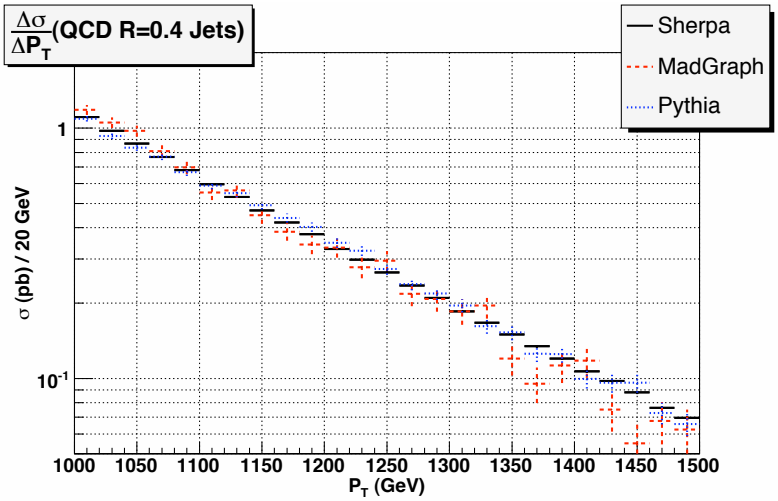

Figure 4.6: The differential cross section for QCD ($R = 0.4$) jet production with respect to the p_T of the leading jet. Sherpa, MG/ME and Pythia are represented.

Pseudorapidity independence of the jet mass distribution

In general, we expect that NP signals will have a pseudorapidity dependence. Therefore, the study of pseudorapidity dependence may provide a tool for NP searches (for an interesting discussion see [94]). In Fig. 4.7, we plot the jet mass distributions for central and outer jets. We observe consistency with the approximation that the distributions are to leading order, independent of pseudorapidity.

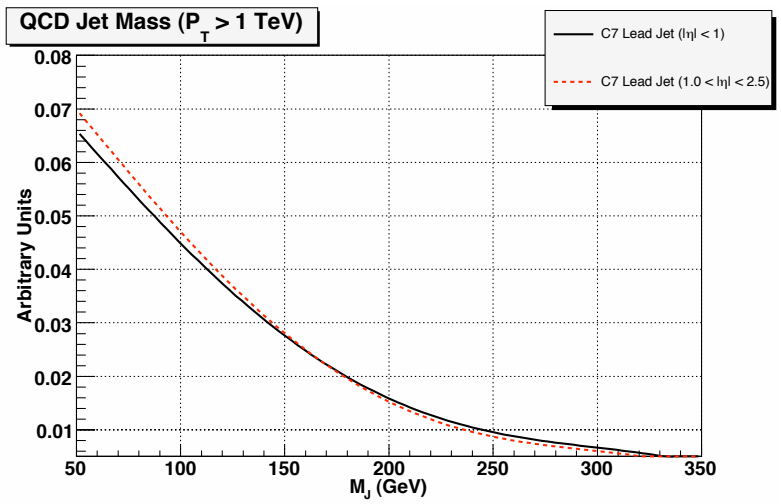

Figure 4.7: The $R = 0.7$ jet mass distribution for central jets ($|\eta| < 1$) and for jets with $1 \leq |\eta| \leq 2.5$. Jets have $p_T \geq 1\,\text{TeV}$. This plot is produced with the Sherpa MC.

4.4 High p_T hadronic top quarks

In this section, we discuss the collimation of the top quark decay products at the partonic level. In Fig. 4.8, we plot the rate of collimation[3] as a function of the top p_T (for a related discussion and analysis see [63, 64, 66]). We define collimation rate as the fraction of top quarks which reconstruct to a jet having $140\,\text{GeV} \leq m_J \leq 210\,\text{GeV}$.

To examine the efficiency of the jet mass methods, it is instructive to look at mass distributions for the signal and background. We examine the distributions for events where the leading jet p_T exceeds 1000 GeV and 1500 GeV with C4 and C7 jets. In Fig. 4.1, we plot the jet mass distribution for the $t\bar{t}$ signal for ${p_T}^{lead} \geq 1000\,\text{GeV}$. The efficiency of C7 jets for capturing the hadronic top is greater than that for C4 jets. For C4 jets, we still observe pronounced structure around the W-mass (M_W), which diminishes for C7 jets. We also note that the peak for the C7 jets moves closer to the top mass, indicating

[3]Due to ISR, collimation rates for final state jets differ from naive expectation values based on partonic-level analysis. As discussed in the text, our analysis methods include a group mass criteria, a simple but powerful discriminant, against ISR jets. Therefore, our results are robust against such effects. Residual contributions are absorbed as a source of background. Refinement of methods to further reduce ISR contributions are analysis-dependent, and outside the scope of this work.

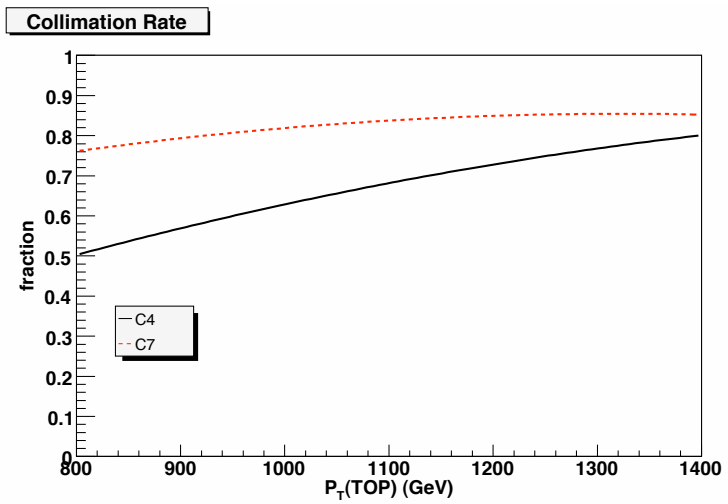

Figure 4.8: The collimation rate for top quarks as a function of their transverse momentum, for C4 (black solid curve) and C7 (red dashed curve) jets. Collimation rate is defined as the fraction of events with top quarks giving rise to a final state jet with $140\,\text{GeV} \leq m_J \leq 210\,\text{GeV}$.

a higher efficiency for capturing the hadronic top. We expect that detector effects will further smear the signal. Fig. 4.1 also shows the mass distributions including leading detector effects (using transfer functions).

We note that the analysis has an inherent tension with regard to choosing the cone size for the jet. The reconstruction cone should be sufficiently wide to capture all the daughter products of the hadronic top. On the other hand, we need to keep the cone appropriately small to keep out the QCD jet background and other soft contamination [64].

We describe the gross features of the top mass distribution, without providing a detailed analytic expression for the top jet. At lowest order in QCD and before decay, the top jet mass distribution is simply $\delta(m_J - m_t)$. This distribution is modified both by QCD radiation and electroweak decay.

We can describe QCD radiation by a top jet function, $J^t_{QCD}(m_{QCD}, R, p_T)$, similar to the functions for massless QCD jets, where J^t_{QCD} is a function of $m_{QCD} \equiv m_t + \delta m_{QCD}$. Gluon radiation from top quarks makes the top jet mass harder, giving the additional mass contribution, δm_{QCD}. Using factorization, this process can be calculated by methods similar to the one discussed in the Appendix, fixing the mass of the parton to m_t and treating it as stable.

For our purposes, the resulting broadening is subdominant for a top mass window of ± 35 GeV. [4] The QCD radiation that determines the shape of J^t_{QCD} at a resolution of ~ 10 GeV is characterized by a very short time scale of $\mathcal{O}(1/(10\,\mathrm{GeV}))$ in the top rest frame.

Although long compared to $1/m_t$, the rest frame time scale on which the distribution in m_{QCD} is determined is substantially shorter than the electroweak time scale, which is set by $\Gamma_t = \mathcal{O}(1.5)$ GeV, the top quark width in the Standard Model [95, 96]. The difference in time scales implies a quantum mechanical incoherence between the QCD radiation, described by J^t_{QCD}, and the top quark weak decay. These two physical processes are thus expected to factorize up to corrections that are determined by the ratio of Γ_t to the size of the top quark window, and we shall assume that this is the case. Using this assumption, we describe the effect of electroweak decay by an overall factor $\mathcal{F}^t_{EW}(\delta m_{EW}, m_{QCD}/(p_T R))$. This function is responsible for producing the two peaks corresponding to the top quark and W boson in the signal mass distribution Fig. 4.1, by acting on the underlying QCD top jet function J^t_{QCD}, which has a single peak at m_t.

We see from Fig. 4.1 that the effect of the decay on the jet mass, δm_{EW}, can be sizable. The actual distribution depends on cone size that we use to identify the jet. The main effect here is a softening of the jet mass, because the jet cone may not capture all the particles from the top quark decay chain. This kinematic effect depends solely on $m_{QCD}/(p_T R)$. As we see from Fig. 4.1, it reduces the mass of the top jet and produces a peak near the W mass. Since the top jet mass softening is a kinematic process, it should be well described by generators based on phase space.

In summary, we can schematically express the top jet mass squared as a sum of three contributions. [5]

$$m_J \sim m_t + \delta m_{QCD} + \delta m_{EW}\,, \tag{4.15}$$

[4] However, a treatment of the broadening is crucial if one aim to improve the top mass measurement at the LHC. At the moment this has been studied only for the ILC [68].

[5] The choice of mass, as opposed to, say, mass squared for the convolution variable is a matter of convention, to keep our notation in J^t_{QCD} consistent with the light quark jet functions. Convolutions in jet mass squared, which are familiar from event shape distributions, can be obtained simply by changing variables and as necessary changing the normalizations of the functions J^t_{QCD} and $\mathcal{F}_{EW}$.

where the jet mass function related to Fig. 4.1 can be schematically written as a convolution of three different sources

$$J^t(m_J, R, p_T) \sim \int d(\delta m_{EW}) dm_{QCD}\, \delta(m_J - m_{QCD} - \delta m_{EW}) \times J^t_{QCD}(m_{QCD}, R, p_T)\, \mathcal{F}_{EW}(\delta m_{EW}, m_{QCD}/(p_T R))\,. \quad (4.16)$$

The top mass is large, so we are not concerned about uncertainties in the lower jet mass spectrum. In fact, the same considerations that lead to this result allow us to conclude that existing MC tools should well describe this part of our studies. We will thus rely on event generators rather than Eq. (4.16) in our numerical studies below.

4.5 $t\bar{t}$ jets vs. QCD jets at the LHC

In this section, we combine the results of the previous discussions, and apply them to analyze energetic SM $t\bar{t}$ events vis-a-vis QCD jet production at the LHC. The main purpose of this section is to understand how well we can discriminate our signal from the overwhelming QCD background. We illustrate an example analysis using the jet functions, and evaluate their performance on MC data. Unfortunately, it is very difficult to outline a one-size-fits-all analysis. Therefore, we perform a broad-strokes analysis that contains sufficient detail to provide general guidance. We do not attempt to invoke advanced, but analysis-specific, procedures that could provide further refinement. It is also important to bear in mind that the final evaluation of the jet functions, as precision analysis tools, can really only be done on real data. The primary reason is that we expect the jet functions to describe physics data. The MC distributions are, at this point, an approximation to what we believe will be LHC data. A precision analysis will show the strains between the jet function-based shape predictions and the effective distribution that MC uses to generate its mass distribution.

We examine two cases in detail, both at truth-level (no detector effects) and accounting for detector effects. The first case, *single tagging*, consists of "top-tagging" (requiring $140\,\text{GeV} \leq m_J \leq 210\,\text{GeV}$) the leading jets satisfying a p_T cut. The second case, *double tagging*, consists of top-tagging the leading

and subleading jets, with a p_T cut only on the leading jet.

4.5.1 Peak resolution

In this analysis, one objective is to resolve the excess of events where the mass of the leading jet lies in the top mass window ($140\,\text{GeV} \leq m_J \leq 210\,\text{GeV}$). It is important to note that we are not hunting for a peak; we already know its location. The issue is that of resolving its magnitude and estimate the probability that the background would fluctuate to yield the observed data. To estimate the significance of such a measurement, we perform a rudimentary analysis for resolving peaks. We emphasize that it is misleading to estimate the significance as $S/\sqrt{B}$, where the signal and background are separate MC samples. These numbers represent an unrealizable scenario, and tend to be optimistic. In real data, there is no way to separate the signal from background with certainty. Furthermore, at the present time, we cannot trust MC to provide the precise shape of QCD jet mass distributions. Therefore, we derive our approximations to the background *shape* directly from the "data", via sideband analysis (outside the top mass window). We use our previous knowledge of the shape of the background in the sideband region, to minimize the number of degree of freedoms involved in the sideband fit. We will discuss this further in the next section.

After approximating the shape of the background in the sideband region, we interpolate the shape of the background into the top mass window. The primary challenges are that our background is large and also has large uncertainties, which induce large uncertainties in the signal. We discuss this in more detail at the conclusion of this section. For the shape of the $t\bar{t}$ signal inside the top mass window, we use MC. In principle, the shape of the top mass distribution can be also derived semi-analytically, as discussed in section 4.4 (see also [68]). However, to leading order we expect the MC data to provide us with a reliable shape (it should capture the radiation at the leading log approximation, also the, phase space, population of the top decay products is purely kinematical). For simplicity we use the simulation data for this step in our analysis. These shapes, after normalization to unit area, are referred to as *probability density functions*. Unfortunately, the standard acronym for probability density functions conflicts with existing usage for parton distribu-

tion functions in this chapter. To avoid confusion, we simply refer to them as *shapes*. We use the approximate shapes for the signal and background to perform an extended maximum likelihood fit to the sample, with jet mass distribution $F(m_J)$, thereby obtaining the background and signal normalizations. We define a jet mass distribution $F(m_J)$ as

$$F(m_J) = N_B \times b(m_J) + N_S \times s(m_J), \tag{4.17}$$

where N_B is the predicted background, and N_S is the predicted signal in the top mass window. $b(m_J)$ and $s(m_J)$ are used to denote the background and signal shapes, respectively. Both N_B and N_S are allowed to float independently.

Sideband background analysis

We perform a sideband analysis in order to avoid the $t\bar{t}$ signal-rich region. The basic goal is to understand the shape of the background by examining a region where there is no signal. In the sidebands, in particular the low side, the signal contaminates the background. In Fig. 4.1, we see that the $t\bar{t}$ signal does not vanish outside the top mass window. Although it is small compared to the QCD background as can be seen in Fig. 4.10, this contamination substantially impacts resolution of the peak. We attempt to purify the background in this region, by rejecting energetic jets consistent with originating from a top quark decay, i.e. - signal, as follows. For a candidate event where the leading jet passes preselection criteria, all jets within a cone $R = 1$ are (vectorially) added into a single combined jet. We call this a group jet, although this definition differs slightly from that in J. Conway, *et al.*, in [64]. If the group mass, m_G, of the combined jet falls within the top mass window, the candidate event is rejected. This discriminant tends to reject events where the decay products of the top quarks are not fully collimated, i.e. reconstructed as a single jet. We must understand any biases introduced by this discriminant. Fig. 4.9 shows the effect of the m_G cuts on the background and signal. The background shape is left relatively intact, but the signal is substantially diminished.

Advanced use of this m_G discriminant is outside the scope of this analysis, possibly leading to more sophisticated analyses (see *e.g.* J. Conway, *et al.*, in [64]). We simply use it to efficiently reject signal events in the sidebands,

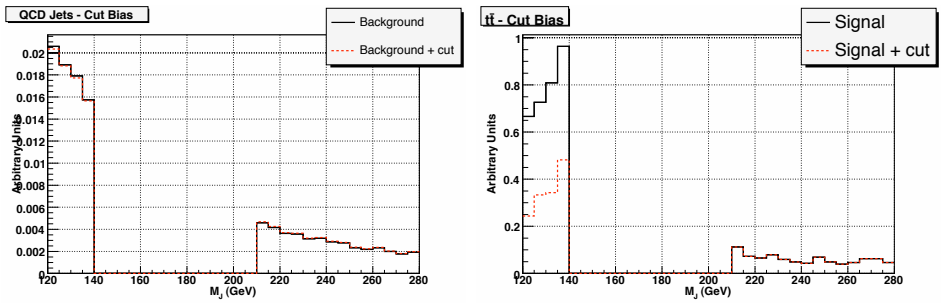

Figure 4.9: The jet mass distributions for the $t\bar{t}$ and QCD jet samples in the sidebands. The plot on the left depicts the shape of the QCD jet sample before and after making a combined jet mass cut on m_G, as described in Sec. 4.5.1. Both curves are normalized to unit area, to show the similarity of the shapes before and after the cut. The plot on the right depicts the effect of the combined jet mass cut on the $t\bar{t}$ signal. The red (dashed) curve shows the effect of the cut relative to the original jet mass distribution (black solid curve). Note: Unlike the left plot, these curves are not renormalized.

while keeping the majority of background events.

We analyze the shape of the background in the sidebands using the jet functions derived in section 4.3. We expect real QCD jets to be an admixture of quark and gluon jets. Therefore, our Ansatz posits the admixture of quarks and gluons as a fraction. We expect small corrections (deviations from a constant admixture) to arise from different sources. For example, we do not consider events with a leading jet of fixed p_T, but rather impose a lower p_T cut. Our Ansatz for the jet mass distribution assumes the following form

$$b(m_J) \propto \beta\left(m_J\right) \times J^Q\left(m_J; p_T^{min}, R\right) + \left(1 - \beta\left(m_J\right)\right) \times J^G\left(m_J; p_T^{min}, R\right), \quad (4.18)$$

where $\beta\left(m_J\right)$ is a linear polynomial $\left(\beta_0 + \beta_1 \frac{m_J}{p_T^{min} R}\right)$. Note that with $b(m_J)$ defined above, along with Eq. (4.17), the total number of degree of freedom involved in the sideband fit is four: β_0, β_1, N_B and N_S.

Significance

After resolving the magnitude of the signal ($t\bar{t}$) peak against that of the QCD jet background, via the methods outlined in the previous sections, we now discuss how to interpret those results. Our analysis is based on *log-likelihood*

ratio method.[6] A background+signal hypothesis to describe a data sample is only meaningful if a background-only hypothesis is unlikely to describe that sample. We estimate the *statistical* significance, n_σ, of the peak as

$$n_\sigma = \sqrt{2\ (\log \mathcal{L} - \log \mathcal{L}_0)}, \tag{4.19}$$

where $\mathcal{L}_0$ is the value of the maximized likelihood function obtained from fitting the data to the background shape alone (equivalent to setting N_S to zero in Eq. (4.17)), and $\mathcal{L}$ is the value of the maximized likelihood function obtained from fitting the data to the background shape and signal shape.[7] The functional form of the likelihood function is given by

$$\mathcal{L} = \prod_{k=1}^{N_{\text{BINS}}} \frac{\exp\left(-F\left(m_k\right)\right) \times \left[F\left(m_k\right)\right]^{N_k}}{N_k!}, \tag{4.20}$$

where we are fitting for the functional form of $F\left(m_J\right)$ as given by Eq. (4.17). Here, m_k and N_k refer to the value of the mass at the center, and the occupancy, of the k-th bin, respectively.

4.5.2 Single top-tagging

For each of the signal ($t\bar{t}$) and background (QCD jets) samples, we preselect events with a p_T cut on the leading jet. In Fig. 4.10 we plot the jet mass distribution including detector effects for the signal and background, including the theoretical upper and lower bound for the background. We show the number of events with jet mass in the range $140\,\text{GeV} \leq m_J \leq 210\,\text{GeV}$. For reference, the number of events for the signal and background, at the truth-level, are presented in table 4.3. It is clear that the background is roughly two orders of magnitude larger than the signal. Once we add detector effects the significance of the signal is further deteriorated. We conclude that a simple counting method would not be effective here.

[6] An excellent discussion may be found in the The Review of Particle Physics [97].

[7] Except in pathological cases, the significance is well approximated by $\frac{S}{\Delta S}$, where S is the fitted signal, and ΔS is the error on S.

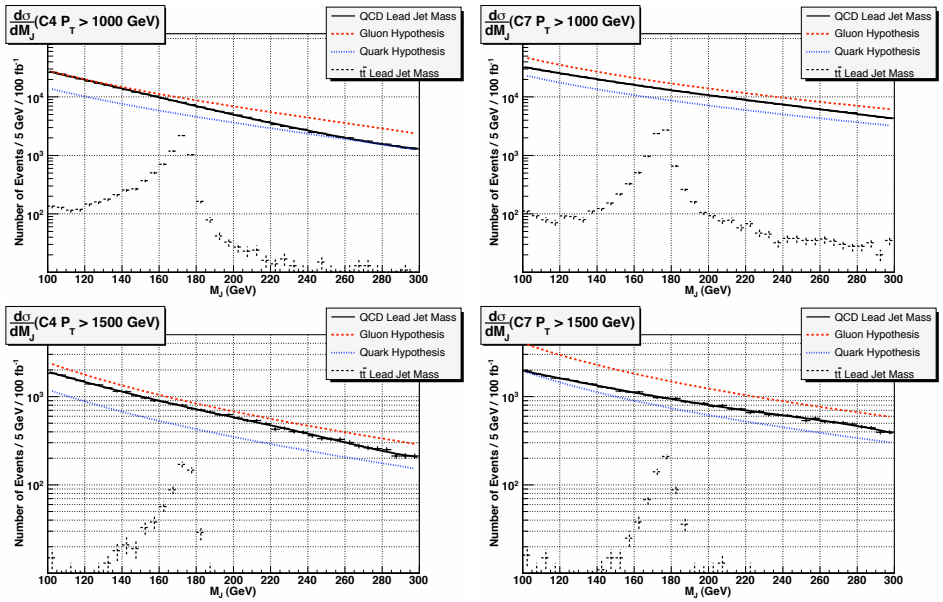

Figure 4.10: The jet mass distributions for the $t\bar{t}$ and QCD jet samples. The plots on the top row correspond to a ${p_T}^{lead} \geq 1000\,\text{GeV}$. The plots on the bottom row correspond to a ${p_T}^{lead} \geq 1500\,\text{GeV}$. The plots on the left correspond to $R = 0.4$; the plots on the right correspond to $R = 0.7$. The theoretical bounds, Eq. (4.11), are also plotted. These numbers are tabulated in table 4.3.

Detector effects

Here, we repeat the truth-level procedure from above, accounting for the leading effects of detector resolution and ±5% jet energy scale. We also tabulate the relative change in acceptance of the signal and background, due to detector resolution and energy scale, which we define as

$$\Delta_{\text{JES}} = \frac{N_{\text{JES}} - N_{\text{TRUTH}}}{N_{\text{TRUTH}}}, \tag{4.21}$$

where N_{JES} is the number of events passing the selection criteria after detector smearing and JES effects have been applied. These results are tabulated in table 4.4, which shows how the signal and background are affected differently by smearing effects. We see that the net effects of the detector smearing plus the uncertainties in the JES lead to substantial uncertainties $\mathcal{O}\,(10\% - 30\%)$ in the signal and background. As anticipated, this leads to a clear failure of simple counting type analyses and calls for a different approach, which will be introduced in the following in the form of sideband analyses and jet shapes.

${p_T}^{lead}$ cut	Cone Size	$t\bar{t}$ (S)	Background (B)	S/B
1000 GeV	C4	6860	113749	0.060
1000 GeV	C7	8725	197981	0.044
1500 GeV	C4	630	10985	0.057
1500 GeV	C7	689	13993	0.049

Table 4.3: Truth-level (no detector effects) results for single-tag jet mass method, reflecting $100\,\text{fb}^{-1}$ of integrated luminosity. S and B reflect the number of jets with 140 GeV $< m_J <$ 210 GeV for the signal and background, respectively.

Results for single tagging

We now apply the analysis described in the previous sections to resolve the peak related to the top quark in the signal region, the top mass window. First we perform a sideband background analysis, to resolve the shape of the background. After applying the cuts described in Sec. 4.5.1, we fit the background to our Ansatz. Fig. 4.11 shows an example of such background fit to our Ansatz. The results of this fit described by Eq. (4.17) and below

$p_T{}^{lead}$ cut	Cone	S (0% JES)	Δ_0	+5% JES	Δ_5	-5% JES	Δ_{-5}
1000 GeV	C4	5778	-15.8%	6562	-4.3%	4798	-30.1%
1000 GeV	C7	7367	-15.6%	8543	-2.1%	6037	-30.8%
1500 GeV	C4	741	17.6%	934	48.3%	536	-14.9%
1500 GeV	C7	789	14.5%	1119	62.4%	601	-12.8%
$p_T{}^{lead}$ cut	Cone	B (0% JES)	Δ_0	+5% JES	Δ_5	-5% JES	Δ_{-5}
1000 GeV	C4	107661	-5.4%	122291	7.5%	90232	-20.7%
1000 GeV	C7	192710	-2.7%	224666	13.5%	154733	-21.8%
1500 GeV	C4	13615	23.9%	18144	65.2%	10108	-8.0%
1500 GeV	C7	18712	33.7%	25361	81.2%	13407	-4.2%

Table 4.4: Acceptance of signal and background for the single tag method, relative to truth-level analysis, accounting for the leading effects of detector resolution and jet energy scale (JES). The $t\bar{t}$ signal is represented in the top half; the QCD jet background is represented in the bottom half. The statistics reflect $100\,\mathrm{fb}^{-1}$ of integrated luminosity. Δ_{JES} is the relative change in background for the indicated JES, relative to truth-level analysis in table 4.3 (cf Eq. (4.21)).

are shown in Fig. 4.12, which demonstrates how the detector affects the signal resolution.

Our main results have been summarized in the tables below. The results of the fitting procedures for the different p_T cuts and cone sizes are shown in tables 4.5 and 4.6 for integrated luminosities of 100 fb^{-1} and 25 fb^{-1} respectively, and subsequently in tables 4.9 and 4.10 for the double top tagging case which is discussed in the following subsection. Our model for the background in these analyses was already introduced in subsection 4.5.1. Apart from the cone size and p_T^{min}, for each JES, we show the result of the fit regarding the number of background (B_{FIT}) and signal (S_{FIT}) events in the mass window and their ratio. ΔS is the error on S_{FIT} and p-value and χ^2/ndf are given to describe the quality of the fit in each case [97]. For our analysis, the total number of degree of freedom is 14 (18 bins $-$ 4 fit parameters: β_0, β_1, N_B and N_S).

Most importantly, we give the statistical significance, n_σ in Eq. (4.19), which is a measure of the probability that fluctuations of the *proposed* background yield in the observed data. The significance value is only as good as the p-value which indicates the goodness of fit. We point out that for entries in which the p-value is lower than, say 5%, the significance figure is probably not reliable. The fitting procedure on that data sample requires further ex-

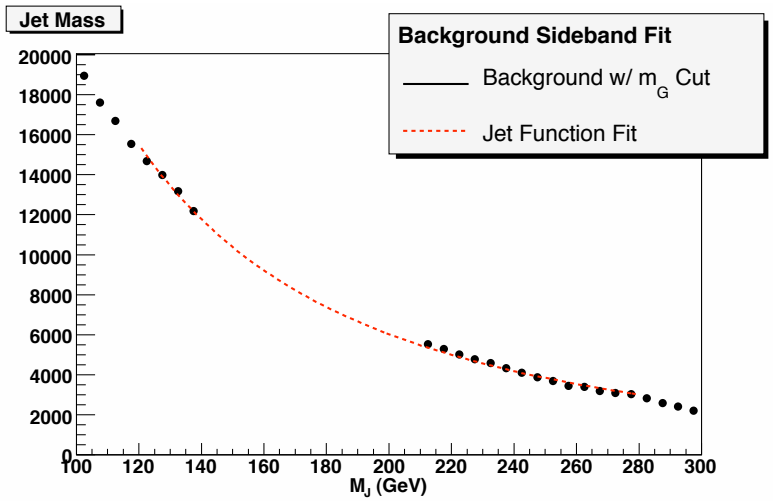

Figure 4.11: A typical example of fitting jet functions to the jet mass distribution in the sideband regions $(120\,\text{GeV} \leq m_J \leq 140\,\text{GeV}) \cup (210\,\text{GeV} < m_J < 280\,\text{GeV})$. This plot corresponds to a single-tag analysis with C7 jets with $p_T \geq 1000\,\text{GeV}$.

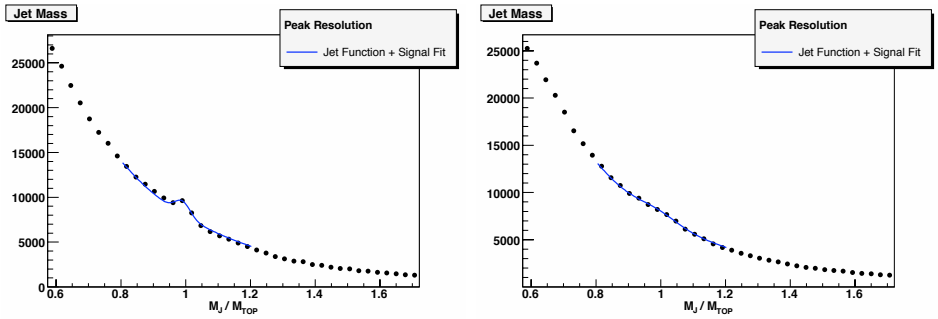

Figure 4.12: The results of fitting jet functions + signal shape to the jet mass distribution in the top mass window. The plot on the left corresponds to a truth-jet analysis. The plot on the right depicts the effects of detector smearing. The statistics reflect 100 fb^{-1} of integrated luminosity.

amination, for residuals and bias analyses, for example, but this falls outside the scope of this work. We find two such instances of failed fits, both in table 4.5. This also suggests how we are to interpret the results of the tables. The relatively large background to signal ratio means that small errors in the background induce relatively large errors in the signal. Furthermore, we have not quantified correlations between the background and signal shapes. Similarities in the shapes can lead to small ambiguities, which are reflected in the fitting parameter errors. The combination of these two difficulties gives rise to an effect, which, strictly speaking, is a defect in the analysis. We remind the reader that we have a large uncertainty in the $t\bar{t}$ signal cross section (see table 4.1), which we have not accounted for in the analysis. We have singled out Sherpa MC data for use in our analyses, and the reader should bear this in mind when interpreting the results in tables 4.5, 4.6, 4.9, 4.10. Small errors in the background shape can yield good fits with high significance figures, and still have relatively large errors in the signal. We are led to interpret the results in the tables as the significance of the peak, relative to the indicated background shape hypothesis (the jet functions in our case). We find that our single tagging method allows us to resolve the $t\bar{t}$ signal from the QCD background with $p_T^{min} \sim 1$ TeV and $25\,\text{fb}^{-1}$ of data. This jet mass analysis does not include any b-tagging or jet-shapes (to be discussed in the following section).

4.5.3 Double top-tagging

The above analyses related to single top-tagging are useful not only for $t\bar{t}$ production, but rather for general cases in which we expect to have at least one very energetic top jet. However, for the cases where there is more than one heavy high-p_T particle, we certainly have more information which can be used to distinguish signal from the QCD background. Clearly, $t\bar{t}$ events contain more information than what is encoded in a single top jet mass. We augment the single-tag analysis for the $t\bar{t}$ signal, by simply requiring that the subleading jet mass be in the top mass window, without imposing a p_T cut. This cut preferentially removes more background events than the signal events, without biasing the distributions. The sideband analysis, applied to the leading jet, remains the same as for the single top-tagging case. As we shall

$p_T{}^{lead} \geq 1000\,\text{GeV}$ Cone $R = 0.4$

JES	B_{FIT}	S_{FIT}	ΔS	n_σ	p-value	χ^2/ndf	$(S/B)_{\text{FIT}}$
0%	106571	6868	671	10.3	0.73	0.74	0.064
5%	120717	8137	715	11.4	0.01	2.01	0.067
-5%	89136	5895	615	9.6	0.95	0.46	0.066

$p_T{}^{lead} \geq 1000\,\text{GeV}$ Cone $R = 0.7$

JES	B_{FIT}	S_{FIT}	ΔS	n_σ	p-value	χ^2/ndf	$(S/B)_{\text{FIT}}$
0%	189185	10892	800	13.7	0.09	1.52	0.058
5%	219189	14020	859	16.4	0.02	1.87	0.064
-5%	151556	9214	720	12.9	0.63	0.83	0.061

$p_T{}^{lead} \geq 1500\,\text{GeV}$ Cone $R = 0.4$

JES	B_{FIT}	S_{FIT}	ΔS	n_σ	p-value	χ^2/ndf	$(S/B)_{\text{FIT}}$
0%	13562	794	224	3.6	1.00	0.26	0.059
5%	17803	1275	256	5.0	0.89	0.58	0.072
-5%	10155	489	193	2.5	0.94	0.49	0.048

$p_T{}^{lead} \geq 1500\,\text{GeV}$ Cone $R = 0.7$

JES	B_{FIT}	S_{FIT}	ΔS	n_σ	p-value	χ^2/ndf	$(S/B)_{\text{FIT}}$
0%	18456	1045	252	4.2	0.75	0.72	0.057
5%	24921	1559	284	5.4	0.96	0.45	0.063
-5%	13315	693	213	3.3	1.00	0.20	0.052

Table 4.5: Estimate of upper limit on significance of peak resolution via single tag method, accounting for detector smearing. S_{FIT} and B_{FIT} are the results of an extended maximum likelihood fit. ΔS is the error on S_{FIT}. Significance n_σ is defined in Eq. (4.19). These results are derived with 100 fb^{-1} of integrated luminosity.

${p_T}^{lead} \geq 1000\,\text{GeV}$ Cone $R = 0.4$

JES	B_{FIT}	S_{FIT}	ΔS	n_σ	p-value	χ^2/ndf	$(S/B)_{\text{FIT}}$
0%	26642	1712	335	5.1	1.00	0.19	0.064
5%	30206	1995	346	5.8	0.96	0.45	0.066
-5%	22371	1379	288	4.8	1.00	0.11	0.062

${p_T}^{lead} \geq 1000\,\text{GeV}$ Cone $R = 0.7$

JES	B_{FIT}	S_{FIT}	ΔS	n_σ	p-value	χ^2/ndf	$(S/B)_{\text{FIT}}$
0%	47277	2730	399	6.8	0.98	0.38	0.058
5%	54870	3419	424	8.1	0.87	0.60	0.062
-5%	37910	2274	354	6.4	1.00	0.21	0.060

${p_T}^{lead} \geq 1500\,\text{GeV}$ Cone $R = 0.4$

JES	B_{FIT}	S_{FIT}	ΔS	n_σ	p-value	χ^2/ndf	$(S/B)_{\text{FIT}}$
0%	3381	201	112	1.8	1.00	0.06	0.059
5%	4418	346	130	2.7	1.00	0.07	0.078
-5%	2519	136	96	1.4	1.00	0.09	0.054

${p_T}^{lead} \geq 1500\,\text{GeV}$ Cone $R = 0.7$

JES	B_{FIT}	S_{FIT}	ΔS	n_σ	p-value	χ^2/ndf	$(S/B)_{\text{FIT}}$
0%	4609	259	125	2.1	1.00	0.18	0.056
5%	6231	382	144	2.6	1.00	0.12	0.061
-5%	3320	174	99	1.6	1.00	0.06	0.052

Table 4.6: Estimate of upper limit on significance of peak resolution via single tag method, accounting for detector smearing. S_{FIT} and B_{FIT} are the results of an extended maximum likelihood fit. ΔS is the error on S_{FIT}. Significance n_σ is defined in Eq. (4.19). These results are derived with 25 fb^{-1} of integrated luminosity.

see even this simple treatment yields a sizable improvement in the significance. Roughly half of the events have smaller p_T than the minimum p_T for the leading jet as shown in Fig. 4.13. Although, by definition, a subleading jet has smaller p_T than the leading one, its p_T distribution is peaked at the ${p_T}^{min}$, and only small portion of events are in the smaller p_T tail region. The number of events for the signal and background, at the truth-level, are presented in table 4.7. To get an idea on how the subleading mass cut affects our signal and background samples, one can compare the numbers given in table 4.3 with the ones in 4.7. For example, we see that at truth level for $R = 0.4$ and ${p_T}^{min} = 1\,\text{TeV}$ the size of the signal sample is decreased by 50% while the background sample by roughly 12%. This is consistent with the results shown in Figs. 4.8 and 4.5 in which the analysis is done for a fixed p_T.

In principle, one could apply a sideband analysis to the subleading jet. However, due to the fact that the p_T is allowed to float, the required analysis would necessarily be more complicated. The double-tagging method increases the signal-to-background ratio, and the significance of the measurements increases. The leading effects of detector resolution and jet energy scale on the signal and background acceptance can be seen in Tables 4.9 and 4.10. We find that our double tagging method yields a reach of up to ${p_T}^{min} \sim 1.5\,\text{TeV}$ with 100 fb^{-1}, without relying on b-tagging or jet-shapes (to be discussed in the following section).

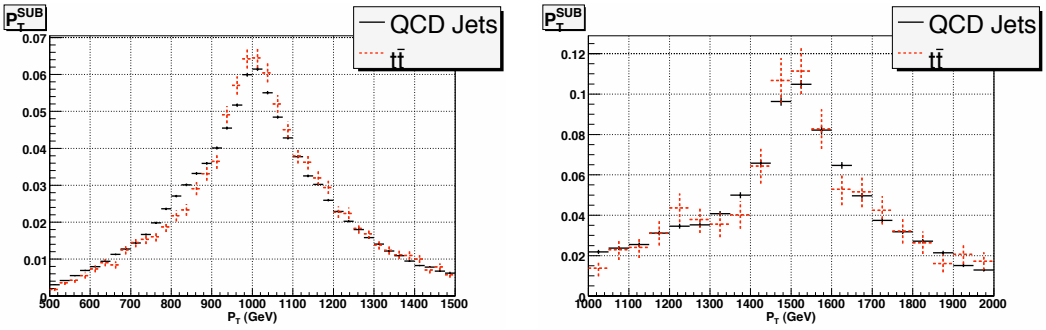

Figure 4.13: We compare the p_T distribution of the subleading jet for the $t\bar{t}$ signal with (the red dotted curve) and without (the black solid curve) leading detector effects. The plot on the left, right corresponds to C4 jets with $\left({p_T}^{lead} \geq 1000, 1500\,\text{GeV}\right)$ respectively.

$p_T{}^{lead}$ cut	Cone Size	$t\bar{t}$ (S)	Background (B)	S/B
1000 GeV	C4	3430	13505	0.254
1000 GeV	C7	6302	36765	0.171
1500 GeV	C4	403	1874	0.215
1500 GeV	C7	458	2724	0.168

Table 4.7: Truth-level (no detector effects) results for double-tag jet mass method using, reflecting $100\,\mathrm{fb}^{-1}$ of integrated luminosity.

$p_T{}^{lead}$ cut	Cone	S (0% JES)	Δ_0	+5% JES	Δ_5	-5% JES	Δ_{-5}
1000 GeV	C4	2601	-24.2%	2868	-16.4%	2228	-35.0%
1000 GeV	C7	4563	-27.6%	5351	-15.1%	3765	-40.3%
1500 GeV	C4	403	0.0%	489	21.3%	292	-27.5%
1500 GeV	C7	487	6.3%	688	50.2%	352	-23.1%
$p_T{}^{lead}$ cut	Cone	B (0% JES)	Δ_0	+5% JES	Δ_5	-5% JES	Δ_{-5}
1000 GeV	C4	13680	1.3%	15187	12.5%	12054	-10.7%
1000 GeV	C7	39361	7.1%	45596	24.0%	32192	-12.4%
1500 GeV	C4	2373	26.6%	3109	65.9%	1746	-6.8%
1500 GeV	C7	4195	54.0%	5651	107.5%	3014	10.6%

Table 4.8: Acceptance of signal and background for the double tag method, relative to truth-level analysis, accounting for the leading effects of detector resolution and jet energy scale (JES). The $t\bar{t}$ signal is represented in the top half; the QCD jet background is represented in the bottom half. The statistics reflect $100\,\mathrm{fb}^{-1}$ of integrated luminosity. Δ_{JES} is the relative change in background for the indicated JES, relative to truth-level analysis in table 4.7 (cf Eq. (4.21)).

$p_T{}^{lead} \geq 1000\,\text{GeV}$ Cone $R = 0.4$

JES	B_{FIT}	S_{FIT}	ΔS	n_σ	p-value	χ^2/ndf	$(S/B)_{\text{FIT}}$
0%	13488	2789	237	11.8	0.99	0.33	0.207
5%	14653	3395	255	13.3	0.94	0.50	0.232
-5%	11762	2516	212	11.9	0.99	0.31	0.214

$p_T{}^{lead} \geq 1000\,\text{GeV}$ Cone $R = 0.7$

JES	B_{FIT}	S_{FIT}	ΔS	n_σ	p-value	χ^2/ndf	$(S/B)_{\text{FIT}}$
0%	38101	5813	358	16.2	0.72	0.76	0.153
5%	43993	6943	386	18.0	0.66	0.81	0.158
-5%	31290	4655	320	14.6	0.57	0.89	0.149

$p_T{}^{lead} \geq 1500\,\text{GeV}$ Cone $R = 0.4$

JES	B_{FIT}	S_{FIT}	ΔS	n_σ	p-value	χ^2/ndf	$(S/B)_{\text{FIT}}$
0%	2341	430	94	4.6	0.99	0.35	0.184
5%	2968	624	110	5.7	0.96	0.45	0.210
-5%	1593	436	79	5.5	0.82	0.66	0.274

$p_T{}^{lead} \geq 1500\,\text{GeV}$ Cone $R = 0.7$

JES	B_{FIT}	S_{FIT}	ΔS	n_σ	p-value	χ^2/ndf	$(S/B)_{\text{FIT}}$
0%	4053	625	129	5.2	1.00	0.28	0.154
5%	5532	801	128	6.3	0.93	0.50	0.145
-5%	2965	399	100	4.0	1.00	0.14	0.135

Table 4.9: Estimate of upper limit on significance of peak resolution via double tag method, accounting for detector smearing, and jet energy scale (JES). S_{FIT} and B_{FIT} are the results of an extended maximum likelihood fit. ΔS is the error on S_{FIT}. Significance n_σ is defined in Eq. (4.19). These results are derived with 100 fb^{-1} of integrated luminosity.

$p_T{}^{lead} \geq 1000\,\text{GeV}$ Cone $R = 0.4$

JES	B_{FIT}	S_{FIT}	ΔS	n_σ	p-value	χ^2/ndf	$(S/B)_{\text{FIT}}$
0%	3367	696	119	5.9	1.00	0.08	0.207
5%	3658	848	128	6.7	1.00	0.12	0.232
-5%	2931	631	106	6.0	1.00	0.07	0.215

$p_T{}^{lead} \geq 1000\,\text{GeV}$ Cone $R = 0.7$

JES	B_{FIT}	S_{FIT}	ΔS	n_σ	p-value	χ^2/ndf	$(S/B)_{\text{FIT}}$
0%	9521	1452	181	8.1	1.00	0.19	0.152
5%	10997	1732	193	9.0	1.00	0.20	0.158
-5%	7817	1162	160	7.3	1.00	0.22	0.149

$p_T{}^{lead} \geq 1500\,\text{GeV}$ Cone $R = 0.4$

JES	B_{FIT}	S_{FIT}	ΔS	n_σ	p-value	χ^2/ndf	$(S/B)_{\text{FIT}}$
0%	577	111	47	2.4	1.00	0.08	0.192
5%	737	155	55	2.8	1.00	0.11	0.210
-5%	393	109	40	2.8	1.00	0.16	0.277

$p_T{}^{lead} \geq 1500\,\text{GeV}$ Cone $R = 0.7$

JES	B_{FIT}	S_{FIT}	ΔS	n_σ	p-value	χ^2/ndf	$(S/B)_{\text{FIT}}$
0%	1005	159	70	2.7	1.00	0.06	0.158
5%	1376	200	64	3.1	1.00	0.12	0.145
-5%	739	96	50	1.9	1.00	0.04	0.130

Table 4.10: Estimate of upper limit on significance of peak resolution via double tag method, accounting for detector smearing, and jet energy scale (JES). S_{FIT} and B_{FIT} are the results of an extended maximum likelihood fit. ΔS is the error on S_{FIT}. Significance n_σ is defined in Eq. (4.19). These results are derived with 25 fb^{-1} of integrated luminosity.

4.6 Jet substructure

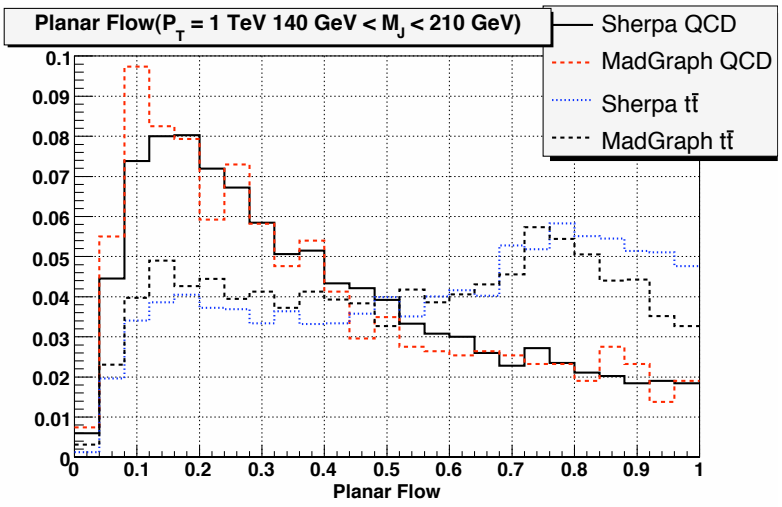

Figure 4.14: The planar flow distribution is plotted for $t\bar{t}$ and QCD jets with mass in the top mass window, $140\,\text{GeV} \leq m_J \leq 210\,\text{GeV}$. Sherpa and MG/ME distributions are represented.

We discussed simple single- and double-mass tagging methods, and we found that we may need additional handles in order to resolve SM $t\bar{t}$ signals for smaller integrated luminosities or higher p_T. We discuss briefly the possibility of using substructure to further analyze energetic jets in the top mass window. We defer the details to our recent work in [25] (see also [51]), where we derive simple analytic expressions to approximate the jet shape variable distributions. For developing additional tools to reslove $t\bar{t}$ signals, there are approaches which exploit information outside of hadronic calorimeter [98] such as tracker or electromagnetic calorimeter. But we limit ourselves to the information encoded only within the hadronic calorimeter to develop significance for resolving $t\bar{t}$ signals. We do not also discuss the possibility of b-tagging for high p_T top-jet [65], which is still under speculation for the range of p_T relevant for our analysis.

Jet shapes are the extensions of well-known event shapes, used at lepton colliders, applied to the analysis of energy flow inside single jets. The fact that we consider only jets with high mass is crucial since it allows us to control the shape of various distributions related to energy flow in a perturbative manner.

As an example, we examine the *planar flow* variable, which measures the extent

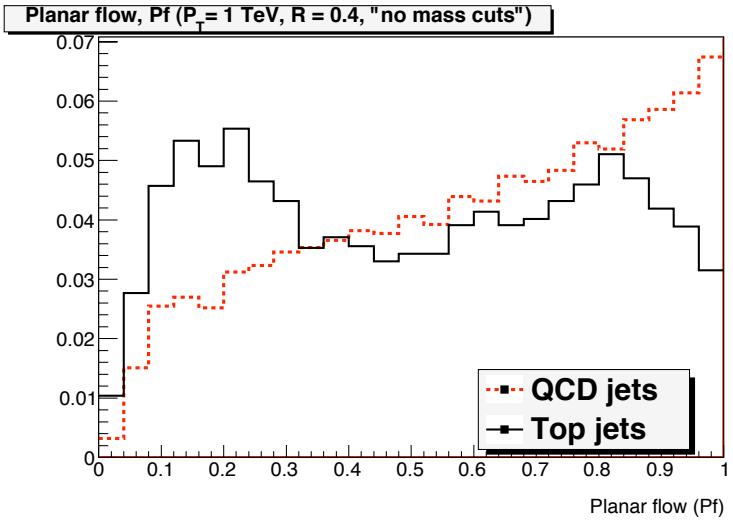

Figure 4.15: The planar flow distribution is plotted for $t\bar{t}$ and QCD jets without fixing jet mass. MG/ME distributions are represented.

to which the energy flow inside the jet is linear or planar. Planar flow (Pf) is defined as follows. We first define an (unnormalized) event shape tensor I_w as[8]

$$I_w^{kl} = \sum_i w_i \frac{p_{i,k}}{w_i} \frac{p_{i,l}}{w_i} , \tag{4.22}$$

where w_i is the energy of particle i in the jet, and $p_{i,k}$ is the k^{th} component of its transverse momentum relative to the thrust axis, which typically coincides with the jet axis. Given I_w, we define Pf as

$$Pf = \frac{4\det(I_w)}{\mathrm{tr}(I_w)^2} = \frac{4\lambda_1\lambda_2}{(\lambda_1+\lambda_2)^2} , \tag{4.23}$$

where $\lambda_{1,2}$ are the eigenvalues of I_w. Pf approaches zero for linear shapes and approaches unity for isotropic depositions of energy. In Fig. 4.14, we plot the planar flow distributions for QCD jets and $t\bar{t}$. As can be seen by comparing Figs. 4.14 and 4.15, it is crucial to consider only events in the top mass window. Without a jet mass cut, the jet shape analysis loses its rejection power.

[8]The overall normalization is not important to this discussion.

4.7 Top quark polarization measurement

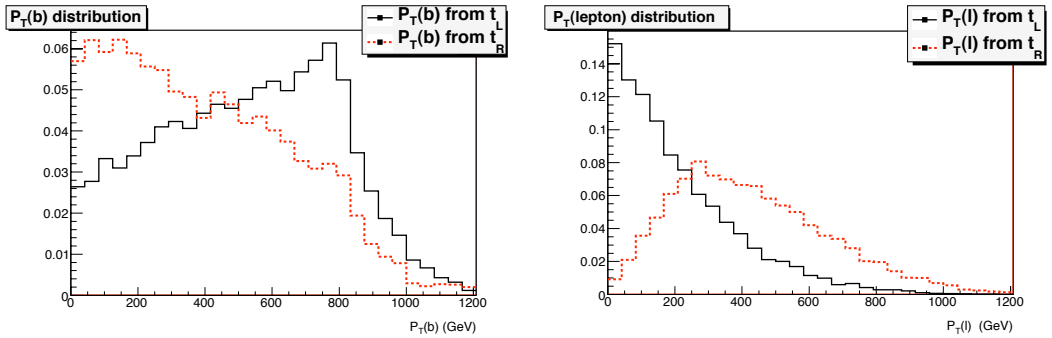

Figure 4.16: In the plot on the left, we show a comparison of the p_T distribution of b quark from t_L (the solid curve) vs. t_R (the dashed curve). In the plot on the right we show the p_T distribution of the charged lepton from t_L (the solid curve) vs. t_R (the dashed curve). We have imposed a lower cut, $p_T^{min} = 1000$ GeV.

In this section, we consider how to exploit b-quarks to measure the polarization of highly boosted hadronic tops. Various new physics models have particle spectra which couple preferentially to one chirality, giving rise to parity violation. Since chirality equals helicity for ultra-relativistic fermions, highly boosted top quarks can help us probe parity violation in the bottom/top quark sector. As is well-known, the top quark decays before the hadronization process occurs, and measurement of the top quark polarization from its leptonic daughters has been studied [61, 62]. We propose using the transverse momentum of the b-quark, inferred from the b-tagged jet, to perform similar measurements. The p_T distribution for the b-quark depends on the chirality of the top-quark. The b-tagged jets should, therefore, also act as good spin analyzers. In Fig. 4.16, we compare the p_T distributions for leptons and b-quarks, for both left- and right-handed top quarks.

As mentioned earlier, the issue of b-tagging at high p_T is quite challenging at this time (for recent studies see [65]), and a fully quantitative study is not yet available. The main idea is to examine the p_T distribution of b-tagged jets, in events where we believe these jets originate from $t \to b\,W$. In order to measure the p_T of the b quark, we need to require at least one of the top-jets should be resolved into more than two jets, since we cannot measure the p_T of the b quark inside a single top-jet. As shown in Fig. 4.8, even for high p_T ($p_T \geq 1000\,\text{GeV}$) top jet, with cone size $R = 0.4$, $\sim 30\%$ of

top-jets can be resolved into more than two jets. By fixing the cone size for jet reconstruction, it is important to understand any biases towards right-handed or left-handed top quarks. Bottom quarks from t_L have a harder p_T distribution than those from t_R, while the opposite is true for leptons from leptonic top quark decays. If one uses a small reconstruction cone, the efficiencies for jet mass reconstruction between the t_L and t_R may differ. We found a negligible bias using cone jets with $R = 0.4$.

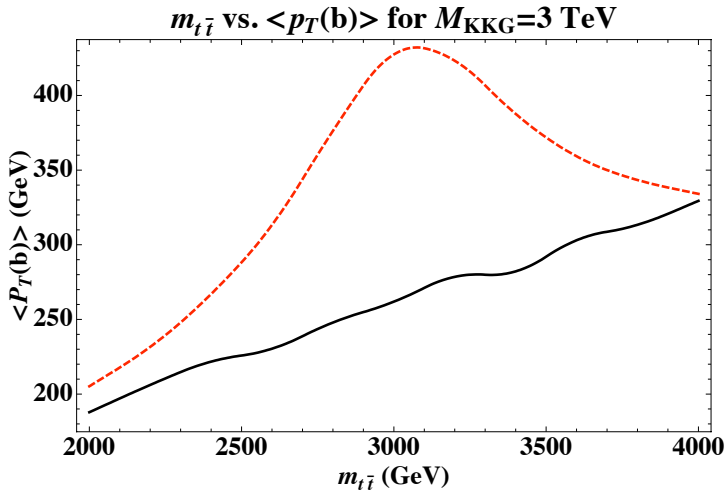

Figure 4.17: We compare the $\langle p_T \rangle$ distribution of the b quark, as predicted by the Standard Model (black solid curve) and by RS1 model with SM fields propagating in the bulk (red dashed curve).

We can develop this discussion further with an example, namely the Randall Sundrum (RS) [99] model with the SM fields propagating in the bulk. We consider the case where the first Kaluza-Klein (KK) excitation of the gluon has a mass $M_{KKG} = 3$ TeV. We perform this analysis at partonic level. In the model we are considering for using b-quark $\langle p_T \rangle$, KK excitations of the gluon couple to left-handed top quarks $\sim 5\times$ stronger than to right-handed top quarks. Typical cross sections for KK gluon production are relatively small. The (background) SM top quarks are produced dominantly via parity-invariant QCD processes, and tend to wash out the signal. In order to resolve the signature, we are compelled to correlate deviations in the b-quark $\langle p_T \rangle$ spectrum to an excess in KK gluon production. In Fig. 4.17, we compare the mean value of the b-quark p_T spectrum, for the Standard Model and RS1 scenarios with

SM fields propagating in the bulk. When correlated to the invariant mass of the KK gluon, we see a substantial deviation in the distribution of the b-quark $\langle p_T \rangle$. In Fig. 4.18, we compare the mean value of the lepton p_T spectrum, for the Standard Model and RS1 scenarios with SM fields propagating in the bulk, where KK excitations of the gluon couple to right-handed top quarks $\sim 5\times$ stronger than to left-handed top quarks.

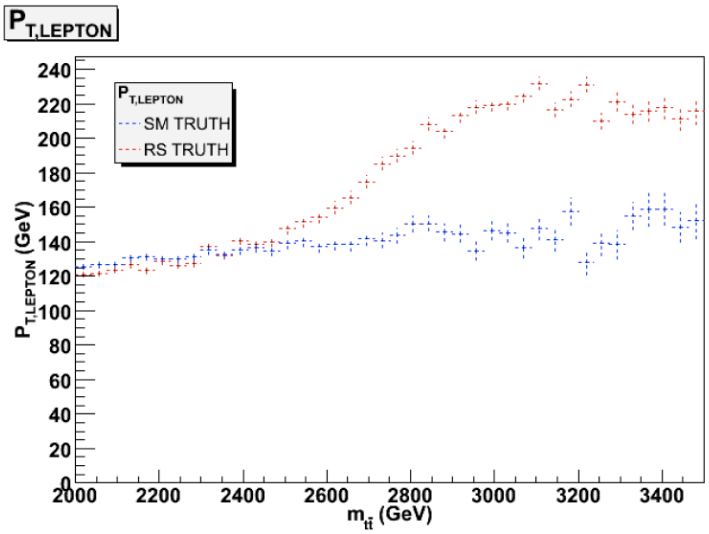

Figure 4.18: We compare the $\langle p_T \rangle$ distributions of the lepton, as predicted by the Standard Model (blue curve) and by RS1 model with SM fields propagating in the bulk (red curve).

4.8 Conclusions

In this study we have mainly focused on high p_T, hadronically decaying, tops in cases where they are fully collimated. Above p_T of 1 TeV the majority of the top daughters particles will be found inside a single cone jet even when the cone size is as small as $R = 0.4$. Therefore, they are simply denoted as top-jets. The leading background for top-jets comes from high p_T QCD jets. We provided analytic expressions for the QCD jet functions which approximate the background and show consistency with MC data. As an example we consider the case of SM $t\bar{t}$ production, and demonstrate how these jet functions, via

side band analysis, allow us to efficiently resolve 1 TeV top-jet from the QCD background with $25\,\mathrm{fb}^{-1}$, and $\sim 1.5\,\mathrm{TeV}$ top-jets with $100\,\mathrm{fb}^{-1}$.

A wide class of new physics models posits $t\bar{t}$ production mechanisms which would significantly contribute to the mass distributions, possibly allowing resolution of excess production with less data. To further improve the significance we consider jet shapes (recently analyzed in [25] and also in [51]), which resolve substructure of energy flow inside cone jets. Augmentation of the analysis, such as the use of jet substructure in combination with a jet mass cut and b-tagging, may improve the signal resolution, allowing us to discover NP signal through top quark channel even with lower luminosity or higher p_T cut. We provided such an example using the *planar flow* jet shape variable, and a detailed analysis is presented in our recent work [25]. We also proposed using the transverse momentum of the bottom quarks to measure top quark polarization as a probe of parity violation.

In this chapter we mostly focused on fairly extreme (but not uncommon at the LHC) kinematical configurations where the tops are fully collimated. This has several advantages such as having direct contact with theoretical based calculation of the jet functions and also the ability to consider arbitrarily high top momenta (at least in principle). However, it is clear that some fraction of the hadronic tops will be reconstructed in 2-jet (intermediate) or $\geq$ 3-jet (conventional) topologies. The fraction of events related to the different topologies is a function of the cone size and p_T. Solid reconstruction algorithms and analyses must be flexible enough to interpolate between these different regions. We note that our approach is complimentary to others that have been proposed recently [42, 50, 51, 64]. In most cases, the difference is related to the fact that the tops considered are not fully collimated and a two-jet topology is exploited to increase the signal to background ratio. It would be very interesting and important to derive theoretically based techniques to control the corresponding distribution of the background relevant to the intermediate region. It is likely that there are overlaps between the different regions. Such issues are important to examine in detail. Mastering these complimentary methods may help to make potential new physics observations more robust, if verified via multiple and independent techniques.

Finally, we want to emphasize that the analysis proposed herein is also

applicable to other processes involving, highly boosted, heavy particles such as electroweak gauge bosons, the Higgs and other new physics particles, to which QCD is a leading background as well.

4.9 Appendix

Here we give details of the definitions and calculations for the jet functions that we employ in section 3. Single inclusive Jet cross sections have been studied intensively [92, 100–102]. Here, we are interested in computing the QCD background to jets of measured mass. The main background to the production of $t\bar{t}$ pairs is from dijet production from hadronic collisions,

$$H_a(p_a) + H_b(p_b) \to J_1(m^2_{J_1}, p_{1,T}, \eta_1, R) + J_2(m^2_{J_2}, p_{2,T}, \eta_2, R) + X, \qquad (4.24)$$

where the final states are jets in the directions of the outgoing partons, each with a fixed jet mass m^2_J , a "cone size" $R^2 = \Delta\eta^2 + \Delta\phi^2$, and transverse momenta, $p_{i,T}$. For simplicity we choose the cone sizes equal for the two jets, although they can be different. For $R < 1$, we can isolate the leading (R^0) dependence of such cross-sections in factorized "jet" functions,

$$\begin{aligned}
&\frac{d\sigma_{H_A H_B \to J_1 J_2}}{dp_T dm^2_{J_1} dm^2_{J_2} d\eta_1 d\eta_2} \\
&\quad = \sum_{abcd} \int dx_a\, dx_b\, \phi_a(x_a)\, \phi_b(x_b) H_{ab\to cd}\left(x_a, x_b, p_T, \eta_1, \eta_2, \alpha_s(p_T)\right) \\
&\quad \times J_1^c(m^2_{J_1}, p_T \cosh\eta_1, R, \alpha_s(p_T))\; J_2^d(m^2_{J_2}, p_T \cosh\eta_2, R, \alpha_s(p_T)),
\end{aligned} \qquad (4.25)$$

with corrections that vanish as powers of R. Here the ϕ's are parton distribution functions for the initial hadrons, $H_{ab\to cd}$ is a perturbative $2 \to 2$ QCD hard-scattering function, equal to the dijet Born cross section at lowest order, and the J_i are jet functions, which are defined below. Jet function J_i summarizes the formation of a set of final state particles with fixed invariant mass and momenta collinear to the i^{th} outgoing parton. Corrections to the cross section of order R^0 can only occur through collinear enhancements which factorize into these functions [35].

Following Ref. [36] we define jet function for quarks at fixed jet mass by

$$\begin{aligned} J_i^q(m_J^2, p_{0,J_i}, R) &= \frac{(2\pi)^3}{2\sqrt{2}\,(p_{0,J_i})^2}\frac{\xi_\mu}{N_c} \\ &\times \sum_{N_{J_i}} \mathrm{Tr}\left\{\gamma^\mu \langle 0|q(0)\Phi_\xi^{(\bar{q})\dagger}(\infty,0)|N_{J_i}\rangle\langle N_{J_i}|\Phi_\xi^{(\bar{q})}(\infty,0)\bar{q}(0)|0\rangle\right\} \\ &\times \delta\left(m_J^2 - \tilde{m}_J^2(N_{J_i},R)\right)\delta^{(2)}(\hat{n}-\tilde{n}(N_{J_i}))\delta(p_{0,J_i}-\omega(N_{J_c})), \quad (4.26) \end{aligned}$$

where $\tilde{m}_J^2(N_{J_i}, R)$ is the invariant mass of all particles within the cone centered on direction $\hat{n}$ in state N_{J_i}. Correspondingly, gluon jet functions are defined by

$$\begin{aligned} &J_i^g(m_J^2, p_{0,J_i}, R) \\ &= \frac{(2\pi)^3}{2(p_{0,J_i})^3}\sum_{N_{J_i}} \langle 0|\xi_\sigma F^{\sigma\nu}(0)\Phi_\xi^{(g)\dagger}(0,\infty)\,|N_{J_i}\rangle\langle N_{J_i}|\Phi_\xi^{(g)}(0,\infty)\,F_\nu^\rho(0)\xi_\rho|0\rangle \\ &\times \delta\left(m_J^2 - \tilde{m}_J^2(N_{J_i},R)\right)\delta^{(2)}(\hat{n}-\tilde{n}(N_{J_i}))\delta(p_{0,J_i}-\omega(N_{J_c})). \quad (4.27) \end{aligned}$$

These functions absorb collinear enhancements to the outgoing particles that emerge from the underlying hard perturbative process and fragment into the observed jets. The Φ's are path ordered exponentials (Wilson lines) defined by

$$\Phi_\xi^{(f)}(\infty,0;0) = \mathcal{P}\left\{e^{-ig\int_0^\infty d\eta\,\xi\cdot A^{(f)}(\eta\,\xi^\mu)}\right\}, \quad (4.28)$$

where $\mathcal{P}$ indicates ordering along the integral and where ξ is a direction with at least one component in the direction opposite to the jet. The full hadronic cross-section is independent of the choice for ξ. As indicated, the gauge field $A^{(f)}$ is a matrix in the representation of the generators for parton f. In general the jet function depends on $\vec{\xi}\cdot\hat{n}$, but for simplicity we suppress this dependence below. Finally the jet functions in Eqs. (4.26) and (4.27) are normalized such that at lowest order we have

$$J_i^{(0)}(m_{J_i}^2, p_{0,J_i}, R) = \delta(m_{J_i}^2). \quad (4.29)$$

4.9.1 Jet functions at next-to-leading order

At next-to-leading order, contributions to the jet mass distributions for light quark or gluon jets have only two particles in their final states. For the quark jet we have the following matrix element which has to be calculated to $\mathcal{O}(g^2)$,

$$\begin{aligned} J_i^q(m_J^2, p_{0,J_i}, R) &= \frac{(2\pi)^3}{2(p_{0,J_i})^2}\frac{\xi_\mu}{N_c\sqrt{2}}\sum_{\sigma,\lambda}\int\frac{d^3p}{(2\pi)^3 2\omega_p}\frac{d^3k}{(2\pi)^3 2\omega_k} \\ &\times \mathrm{Tr}\left\{\gamma^\mu\langle 0|q(0)\Phi_\xi^{(\bar{q})\dagger}(\infty,0)|p,\sigma;k,\lambda\rangle\langle p,\sigma;k,\lambda|\Phi_\xi^{(\bar{q})}(\infty,0)\bar{q}(0)|0\rangle\right\} \\ &\times\delta\left(m_J^2-(p+k)^2\right)\,\delta^{(2)}(\hat{n}-\hat{n}_{\vec{p}+\vec{k}})\,\delta(p_{0,J_i}-p^0-k^0), \end{aligned} \tag{4.30}$$

where σ and λ denote the polarizations , and p and k the momenta of the final-state quark and gluon respectively with $\hat{n}_{\vec{p}+\vec{k}} \equiv \frac{\vec{p}+\vec{k}}{|\vec{p}+\vec{k}|}$. Similarly, for the gluon jet we have

$$\begin{aligned} J_i^g(m_J^2, p_{0,J_i}, R) &= \frac{(2\pi)^3}{4(p_{0,J_i})^3}\sum_{N_{J_i}}\int\frac{d^3p}{(2\pi)^3 2\omega_p}\frac{d^3k}{(2\pi)^3 2\omega_k} \\ &\times\langle 0|\xi_\sigma F^{\sigma\nu}(0)\Phi_\xi^{(g)\dagger}(0,\infty)\,|p,\sigma;k,\lambda\rangle\langle p,\sigma;k,\lambda|\Phi_\xi^{(g)}(0,\infty)\,F_\nu{}^\rho(0)\xi_\rho|0\rangle \\ &\times\delta\left(m_J^2-(p+k)^2\right)\,\delta^{(2)}(\hat{n}-\hat{n}_{\vec{p}+\vec{k}})\,\delta(p_{0,J_i}-p^0-k^0), \end{aligned} \tag{4.31}$$

where p and k are the final state momenta within the cone size, R. To evaluate these matrix elements, we need the rules for vertices shown in Fig. 4.19 for the field strengths. The double lines represent the perturbative expansion of the Wilson lines (4.28) in the ξ-direction (see Eq. (4.34)), whose vertices and propagators are shown in Fig. 4.20. The resulting diagrammatic contributions to the quark and gluon jet functions at next-to-leading order are shown in Fig. 4.21 and Fig. 4.22 respectively.

We choose a frame where the jet is in the $\eta_J = \phi_J = 0$ direction and the vector ξ is light-like and in a direction opposite to the jet,

$$p_{J_i} = p_{0,J_i}(1,\beta_i,0,0) \quad \xi = \frac{1}{\sqrt{2}}(1,-1,0,0)\,, \tag{4.32}$$

where $\beta_i = \sqrt{1-m_{J_i}^2/p_{0,J_i}^2}$ is the velocity of the jet. In this frame we parametrize

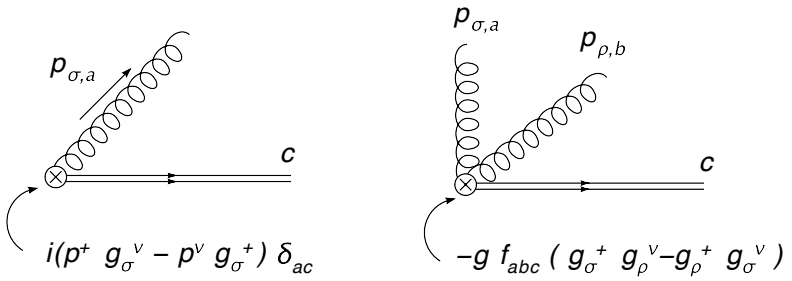

Figure 4.19: Feynman rules associated with the $F^{+\nu}$ operator at the end of a Wilson line.

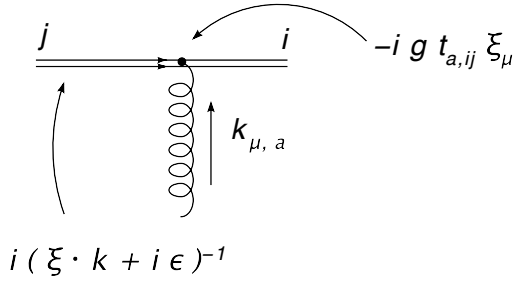

Figure 4.20: Feynman rules associated with eikonal lines, from the expansion of the Wilson lines.

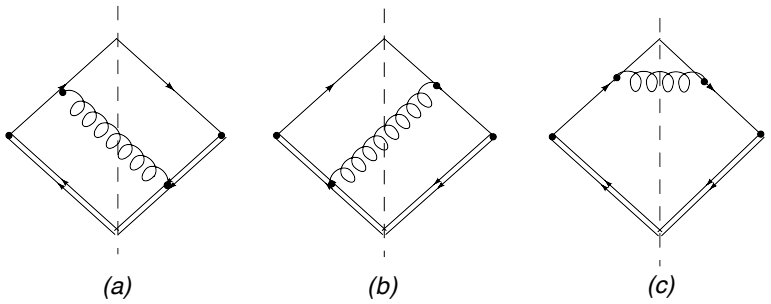

Figure 4.21: Real contributions to the quark jet function at order α_s.

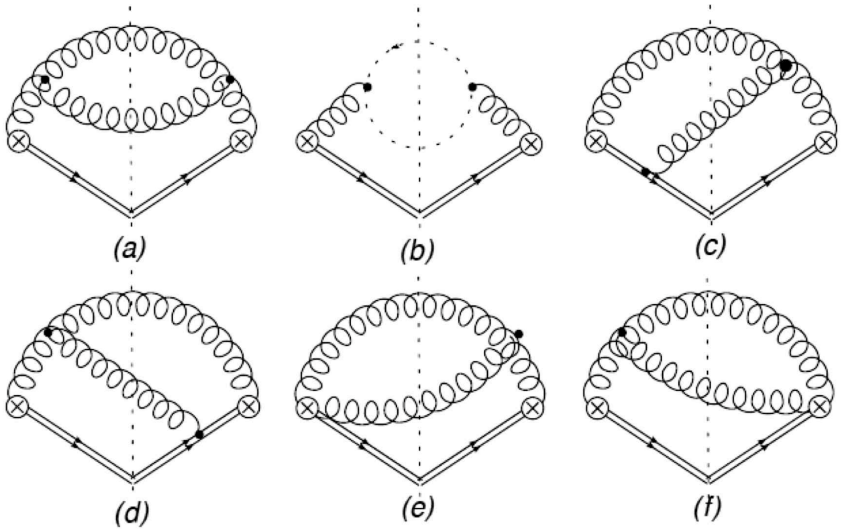

Figure 4.22: Real non-vanishing contributions to the gluon jet function in Feynman gauge at NLO.

the momenta p and k above by

$$p = p^0(1, \cos\theta_p, \sin\theta_p, 0) \quad k = k^0(1, \cos\theta_k, -\sin\theta_k, 0)\,, \tag{4.33}$$

where $\theta_{p,k}$ represents the angle of each particle to the jet axis $\hat{n}$. The path ordered exponentials are expanded order-by-order in g_s, related to the rules in Fig. 4.20 by the expansion,

$$\begin{aligned}\Phi_\xi(\infty, 0; 0) &= \mathcal{P}\left\{e^{-ig\int_0^\infty d\eta\, \xi\cdot A(\eta\,\xi^\mu)}\right\} \\ &= 1 - ig\int \frac{d^4k}{(2\pi)^4}\frac{i}{\xi\cdot k + i\epsilon}\xi\cdot A(k) + \dots\,. \end{aligned}\tag{4.34}$$

We begin with the calculation of the quark jet function, which readily reduces to an integral over the energy and angle of one of the particles,

$$\begin{aligned}J_i^{q(1)}(m_J^2, p_{0,J_i}, R) &= \frac{\beta_i}{8\sqrt{2}}\int \frac{d\cos\theta_k dk_0 k_0}{\pi(p_{0,J} - k_0)}|\mathcal{M}(p,k)|^2 \\ &\quad\times\delta(m_j^2 - 2k^0 p_{0,J}\,(1 - \beta_i\cos\theta_k))\Theta(R - \theta_k)\,, \end{aligned}\tag{4.35}$$

where we choose k to represent the gluon and p the quark. For k the softer momentum, we easily see that $\theta_k \geq \theta_p$. Therefore, $p_0 = k_0$ fixes the minimum

angle for the softest particle, and we find $\cos(\theta_{S,min}) = \beta_i$. The region $\omega_p < \omega_k$ is found by simply interchanging p and k in $|\mathcal{M}(p,k)|^2$ so that

$$\begin{aligned} J_i^{q(1)}(m_J^2, p_{0,J_i}, R) &= \frac{\beta_i}{16\sqrt{2}} \int_{\cos(R)}^{\beta_i} \frac{d\cos\theta_S}{(2\pi)^2} \frac{m_{J_i}^2/p_{0,J}^2}{\left(2(1-\beta_i\cos\theta_S) - \frac{m_{J_i}^2}{p_{0,J}^2}\right)} \\ &\times \frac{1}{p_{0,J}(1-\beta_i\cos\theta_S)} \left(|\mathcal{M}_{q_i}(p,k)|^2 + |\mathcal{M}_{q_i}(k,p)|^2\right) . \end{aligned} \tag{4.36}$$

The evaluation of $|\mathcal{M}_{q_i}(p,k)|^2$ is straightforward from the diagrams of Fig. 4.21, and we find

$$\begin{aligned} J_i^{q(1)}(m_J^2, p_{0,J_i}, R) &= \frac{C_F\beta_i}{4m_{J_i}^2} \int_{\cos(R)}^{\beta_i} \frac{d\cos\theta_S}{\pi} \\ &\times \frac{\alpha_s(k_0)\, z^4}{(2(1-\beta_i\cos\theta_S) - z^2)\,(1-\beta_i\cos\theta_S)} \\ &\times \left\{ z^2 \frac{(1+\cos\theta_S)^2}{(1-\beta_i\cos\theta_S)} \frac{1}{(2(1+\beta_i)(1-\beta_i\cos\theta_S) - z^2(1+\cos\theta_S))} \right. \\ &\left. + \frac{3(1+\beta_i)}{z^2} + \frac{1}{z^4} \frac{(2(1+\beta_i)(1-\beta_i\cos\theta_S) - z^2(1+\cos\theta_S))^2}{(1+\cos\theta_S)(1-\beta_i\cos\theta_S)} \right\}, \end{aligned} \tag{4.37}$$

where $z = \frac{m_{J_i}}{p_{0,J_i}}$, $p_{0,J_i} = \sqrt{m_{J_i}^2 + p_T^2}$, and $k_0 = \frac{p_{0,J_i}}{2} \frac{z^2}{1-\beta_i\cos\theta_S}$.

The calculation of the gluon jet function proceeds along the same lines, with the exception that both particles in the final states are now identical, and the presence of the field strengths, which appear at the end of each Wilson line. The rules for these vertices, as mentioned before, are shown in Fig. 4.19. Once again, we can write the gluon jet function as an integral over the angle of the softer particle,

$$\begin{aligned} J_i^{g(1)}(m_J^2, p_{0,J_i}, R) &= \frac{\beta_i}{16m_{J_i}^2} \int_{\cos(R)}^{\beta_i} \frac{d\cos\theta_S}{(2\pi)^2 p_{0,J_i}^2} \\ &\times \frac{z^2}{(2(1-\beta_i\cos\theta_S) - z^2)\,(1-\beta_i\cos\theta_S)} |\mathcal{M}_{g_i}(p,k)|^2 , \end{aligned} \tag{4.38}$$

where $|\mathcal{M}_{g_i}(p,k)|^2$ is symmetric under the interchange of p and k. We find

from the diagrams shown in Fig. 4.22, the result

$$\begin{aligned} J_i^{g(1)}(m_J^2, p_{0,J_i}, R) &= \frac{C_A \beta_i}{16 m_{J_i}^2} \int_{\cos(R)}^{\beta_i} \frac{d\cos\theta_S}{\pi} \\ &\times \frac{\alpha_s(k_0)}{(1-\beta\cos\theta_S)^2(1-\cos^2\theta_S)(2(1+\beta)-z^2)} \\ &\times \big(z^4(1+\cos\theta_S)^2 + z^2(1-\cos^2\theta_S)(2(1+\beta_i)-z^2) \\ &\quad + (1-\cos\theta_S)^2(2(1+\beta_i)-z^2)^2 \big)^2 . \end{aligned} \tag{4.39}$$

These one-loop expressions have been used to generate the comparisons to event generator output given in Section 3.

4.9.2 R-dependence

It is of interest to isolate the leading logarithmic contributions in both gluon and quark jets, which can be found from eikonal graphs in the adjoint and fundamental representations respectively,

$$\begin{aligned} J^{(eik),c}(m_{J_1}^2, p_T, R) &= \frac{2\,C_c}{\sqrt{2} p_T} g^2 \int \frac{d^3k}{(2\pi)^3 2\omega_k} \frac{\xi\cdot p_J}{\xi\cdot k} \frac{\xi\cdot p_J}{2 p_J\cdot k} \\ &\quad \times \delta\left(m_{J_1}^2 - (p_1+k)^2\right) \Theta\left(p_T - k_T\right) . \end{aligned} \tag{4.40}$$

Parametrizing k as

$$k = k_T \left(\cosh\eta_k, \cos\phi_k, \sin\phi_k, \sinh\eta_k\right) , \tag{4.41}$$

this leads to

$$\begin{aligned} J^{(eik),c}(m_{J_1}^2, p_T, R) &= g^2 \frac{C_c}{(2\pi)^3} \int dk_T\, k_T\, d\phi_k d\eta_k \, \frac{1}{k_T^2\left(\cosh^2\eta_k - \cos^2\phi_k\right)} \\ &\quad \times \delta\left(2 p_T\, k_T \left(\cosh\eta_k - \cos\phi_k\right) - m_{J_1}^2\right) \Theta\left(p_T - k_T\right) \\ &= g^2 \frac{C_c}{(2\pi)^3} \int d\phi_k d\eta_k \, \frac{1}{m_{J_1}^2} \frac{1}{k_T^2\left(\cosh^2\eta_k - \cos^2\phi_k\right)} \\ &\quad \times \delta\left(2 p_T\, k_T\, r - m_{J_1}^2\right) \Theta\left(\cosh\eta_k - \cos\phi_k - \frac{m_{J_1}^2}{p_T^2}\right) . \end{aligned} \tag{4.42}$$

In this expression we can change the variables to

$$\eta_k = r\cos\theta, \quad \phi_k = r\sin\theta\,. \tag{4.43}$$

Since we are dealing with highly collimated jets we can expand the integrand in r and integrate over θ, finding

$$\begin{aligned} J^{(eik),c}(m^2_{J_1}, p_T, R) &\simeq g^2\frac{2C_c}{(2\pi)^2}\int_{m_J/p_T}^{R} dr\,\frac{1}{m^2_{J_1}}\left\{\frac{1}{r}+\mathcal{O}(r^3)\right\} \\ &\simeq \alpha_s(p_T)\frac{C_c}{m^2_{J_1}\pi}\left\{\log\left(\frac{R^2\,p_T^2}{m_J^2}\right)+\mathcal{O}(R^4)\right\}, \end{aligned} \tag{4.44}$$

which shows explicitly the logarithmic behavior in R. Leading logarithmic contributions can be exponentiated, giving us a qualitative description of lower jet masses,

$$J^{(eik),c}(m^2_{J_1}, p_T, R) \simeq \frac{\alpha_s}{\pi}C_c\frac{1}{m_J^2}\log\left(\frac{R^2p_T^2}{m_J^2}\right)\exp\left\{-\frac{\alpha_s}{2\pi}C_c\log^2\left(\frac{R^2p_T^2}{m_J^2}\right)\right\}. \tag{4.45}$$

Without the above approximations, the eikonal jet function is given by

$$J^{(eik),c}(m_J, p_T, R) = \alpha_s(p_T)\frac{4\,C_c}{\pi m_J}\log\left(\frac{p_T}{m_J}\tan\left(\frac{R}{2}\right)\sqrt{4-\left(\frac{m_J}{p_T}\right)^2}\right). \tag{4.46}$$

As we have observed above, all R^0 behavior in the cross section can be found from the jet functions. We can also estimate the contribution of soft initial-state radiation on the cone-jet masses. Here we verify that such radiation is sub-leading in powers of R^2. Contributions due to wide angle gluons come from a "soft function" [35], which is defined in terms of an eikonal cross section,

$$S(m^2_{J_i}) \sim \sum_{N_s}\sigma^{(eik)}(N_s)\delta(m^2_{J_1} - \tilde{m}^2_J(N_s, R)). \tag{4.47}$$

Diagrams that can contribute to the jet mass are illustrated in Fig. 4.23. The initial state radiation shown behaves as

$$S \sim \int d^4k\delta(k^2)\frac{p_a\cdot p_b}{(p_a\cdot k)(p_b\cdot k)}\delta(m^2_{J_1} - 2p_1\cdot k)\Theta(R-\tilde{R}(\eta_k,\phi_k))\,, \tag{4.48}$$

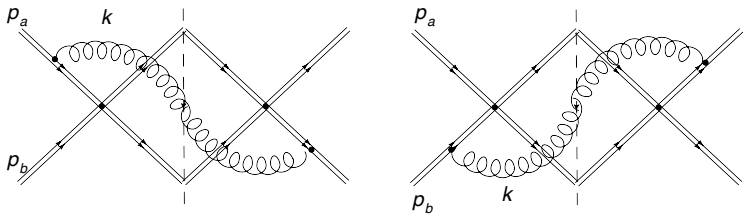

Figure 4.23: Contributions to the jet mass from the soft function.

with p_a and p_b the momenta of incoming partons, neither of which is in the direction of the observed jets. Choosing a frame where the initial momenta are given by

$$p_a = \frac{\sqrt{s}}{2}(1,0,0,1)\,, \quad p_b = \frac{\sqrt{s}}{2}(1,0,0,-1)\,, \tag{4.49}$$

and parametrizing the radiated gluon's momentum k as in Eq. (4.41) above, we find

$$\begin{aligned} S &\sim \int dk_T d\phi_k d\eta_k \frac{1}{k_T} \frac{1}{2p_T(\cosh\eta_k - \cos\phi_k)} \delta\left(k_T - \frac{m_{J_1}^2}{2p_T(\cosh\eta_k - \cos\phi_k)}\right) \\ &\sim \frac{2\pi}{m_{J_1}^2} \int_0^R dr\, r = \frac{\pi R^2}{m_{J_1}^2}\,, \end{aligned} \tag{4.50}$$

which is, as expected, power-suppresed in R compared to the logarithmic dependence we get from the jet function.

Chapter 5

Probing the Gauge Content of Heavy Resonances

5.1 Introduction

QCD has been successfully tested in many hadronic processes at high energy. Current efforts in perturbative QCD have moved toward precision, to help gain accurate predictions for Standard Model processes in collider experiments as backgrounds to new physics. Precise prediction is a key to find new physics, because QCD events should be distinguished from signals in order to claim the discovery of new phenomena at colliders. In this chapter, we show how to use factorized cross sections as a tool for analyzing the gauge content of new heavy particles.

Factorization is a statement of the quantum mechanical incoherence of short and long distance physics, and plays an important role in the use of perturbative QCD. Perturbative calculations of factorized partonic cross sections depend on the separation of regions of momentum space. The three basic regions describe off-shell "hard" partons at short distances, energetic, on-shell "collinear" partons near the light cone, and long-wavelength, "soft" partons (see Ref. [19] for reviews and references therein). Once we obtain a factorized form of the cross section for a certain process, resummation can be achieved from the independence of physical quantities from factorization scales, which leads to evolution equations [33]. The evolution equations can be solved to resum large logarithmic corrections in terms of perturbative anoma-

lous dimensions. Especially, the soft anomalous dimension matrix introduced in Refs. [103, 104], which is the main interest in this chapter, allows us to describe soft gluon radiation systematically in hadronic collisions.

In the mid 1990's, dijet rapidity gap events with anomalously low radiation in a wide interjet rapidity region for electron-proton collision were observed at HERA [105–107] and for proton-antiproton scattering at the Tevatron [108]. Such events were predicted from the exchange of two or more gluons in a color singlet configuration, which avoids color recombination between jets [109]. A quantitative explanation of these events in terms of factorizable cross sections was studied in Ref. [110], which discussed the dependence of the dijet cross section on energy flow, Q_c, into the central region, in terms of a soft function that is a matrix in the space of the possible color exchange at the hard scattering. A "gap" here refers to low energy flow Q_c. Since then, there have been various studies of gap events from this point of view. The soft anomalous dimension matrix, denoted by Γ_S below, for rapidity gap events, was calculated in Ref. [110], and used to resum the leading logarithmic contributions in Refs. [32, 111]. The soft anomalous dimension matrix for three jet rapidity gap processes was calculated in Refs. [112–114].

Cross sections computed from the soft anomalous dimension matrix organize "global" logarithms, following the terminology introduced in Ref. [115], and as such do not organize all logarithms of the gap energy. Non-global logarithmic contributions, mis-cancellations from secondary emission, discovered by Dasgupta and Salam [115], were resummed in the large N_c approximation [116]. More recently, Forshaw, Kyrieleis and Seymour have discovered new logarithmic contributions which they name "super-leading logarithms", which do not seem possible to exponentiate by current techniques [117–119]. The contributions of these non-global logarithms, however, are generally not dominant [120, 121].

In this chapter, we study the pattern of soft gluon radiation into a rapidity gap for the production of heavy particles in hadron-hadron scattering at leading order in the soft matrix, Γ_S, which resums global logarithms. The pattern depends on color flow in the hard scattering, and reflects the gauge content of new particles that participate in the process, for example, as s-channel resonances.

The results of this chapter illustrate the use of energy flow, treated by perturbative QCD and factorization, as a diagnostic tool for determining the color SU(3) representation of new resonances, and the use of resummation for more precise cross sections. Previous work on soft gluon radiation for the study of new physics includes Ref. [122] for Higgs boson production in association with two hard jets, and Refs. [123, 124] for gluino and squark pair production, which describe resummed cross sections to provide more accurate predictions for signals.

There are many proposals for extensions of the Standard Model. These could provide solutions to the hierarchy problem, dark matter explanation, the origin of mass, etc. The most common feature of the models is that they include new heavy particles transforming under definite gauge groups. In many scenarios, we expect that they are created with $\mathcal{O}$(TeV) mass via s-channel processes in hadron-hadron scattering. Possible processes with various spins and gauge groups of new heavy particles are studied and summarized in Ref. [77], which considers new sectors that decay into a top quark pair. There have been studies for identifying signals, including hadronic or leptonic decays from gauge Kaluza-Klein (KK) resonance states and from QCD background [61, 62, 66, 71, 125–129]. These studies show that the ability to distinguish signals especially from hadronic decays, which have much larger branching ratio than leptonic decays, depends on both how strongly the new sector is coupled to the Standard Model and to what extent signals and backgrounds are separated [25, 26, 50–52, 130–132]. Also, various methods for spin measurements of the intermediate new particles have been suggested and discussed (see Ref. [133] for reviews and references therein).

Our study begins from this point. Once we succeed in distinguishing a resonance from backgrounds, a remaining task is to determine the SU(3) color gauge content of the resonance particle, denoted as V'. For simplicity we consider below two possibilities; color-singlet (Z') and color-octet (G). Since we consider QCD radiation with total energy much less than resonance energy, our considerations do not depend on the details of the model. In this chapter, we assume that the decay width is large enough that a hard function is an effective vertex. We will, however, discuss the consequences of a narrow resonance at the end of Secs. 5.3 and 5.6.

In many models there are gauge interactions whose coupling with a top quark pair is enhanced in particular. These include models with a KK excited graviton, weak and strong gauge bosons in extra dimensions [134, 135], as well as heavy spin-0 particles in MSSM and two-higgs-doublet model (2HDM) [136, 137] and spin-1 coloron and axigluon [138]. Such new particles V' of mass M and spin (sp) could show up as resonances in $pp(\bar{p}) \to V'(M, sp) \to Q\bar{Q}$ at the Tevatron and the LHC. We may expect larger branching ratios for heavy quark pair production than for other channels such as massless dijets or dileptons, due to the small couplings of V' to light particles. This motivates the calculation of an analytic form describing soft gluon emission in heavy quark pair production. At the level of global logarithms, this is determined by the soft anomalous dimension matrices for rapidity gap processes involving massive particles. The "massive" soft anomalous dimension matrix for heavy pair production was studied in Refs. [29, 48, 139–145] for threshold resummation. In this chapter, we extend this work to introduce the massive soft anomalous dimension matrix for rapidity gap cross sections, which will be used as a tool for our analysis.

Reference [110] studied rapidity gaps for a process in which t-channel exchange was dominant. The result indicates that, in the limit of a very large interjet region, the color singlet component dominates, with more radiation into the gap when the exchange is a color-octet. In this study, however, we might expect a different pattern of soft gluon radiation due to new heavy particle resonances in the s-channel rather than t-channel. The quantity of interest is the gap fraction, the ratio of the number of events for heavy quark pair production with a gap energy up to some value Q_0 to the total number of events for the process. We will find a quantitative difference that is quite distinguishable and can be used for the study of the gauge content in the new sector. This difference, especially caused by the SU(3) color content, is related to "drag" effects in e^+e^- three-jet $(q\bar{q}g)$ events, compared to $q\bar{q}\gamma$ events [146–148]. The color dipole configurations explain a surplus of radiation in the qg and $\bar{q}g$ interjet regions for three-jet events, while radiation is enhanced in the $q\bar{q}$ region for $q\bar{q}\gamma$ events.

In this study, we do not give a detailed study of non-global [115] or super-leading logarithms [117], arising when gluons radiated outside the gap emit

back into the gap. The latter are sometimes called secondary emissions. We can in principle introduce correlations between energy flow and event shapes that suppress such secondary emissions naturally. This technique was introduced in Ref. [36] for rapidity gap e^+e^- dijet events. Such correlations control secondary radiation, by suppressing states with radiation outside the gap at intermediate energy scales, leading to perturbatively computable measures insensitive to non-global logarithms. In our study, the rapidity gap we choose does not allow radiation of high transverse momentum outside the gap by definition, which suppresses the non-global logarithms from final-state radiation. On the other hand, another issue arises for hadronic collisions, where there is secondary emission nearly parallel to the initial partons. Several classes of observables studied in Refs. [149–151] could be used to suppress exponentially forward radiation, which would then ensure the suppression of non-global, including super-leading, logarithms.

In the following section, we study the definition and kinematics of rapidity gap processes and review the relevant factorization procedure. Here, we introduce the energy flow defined in Ref. [110], and define the gap fraction. After studying the gap fraction in terms of energy flow, we study its relation to color flow at short distances in Secs. 5.3 and 5.4. We argue that the gap fraction exposes the pattern of soft gluon radiation, depending on the color SU(3) gauge content of the resonance in $q\bar{q}(gg) \to Z'/G \to Q\bar{Q}$. In Sec. 5.5, the gap fraction for heavy quark pair production induced by a heavy spin-1 resonance is studied. Finally, in Sec. 5.6, we apply our formalism for a study of spin-0 or 2 resonance particles associated with different partonic processes.

5.2 Heavy quark pair rapidity gap cross sections

5.2.1 Definitions

In this section, we will focus on rapidity gap cross sections for heavy quark pair production through a new physics particle resonance denoted by $V'(M, sp)$ of mass M and spin sp. The partonic scattering process for proton and (anti)-

proton collisions, creating s-channel resonance V', is

$$\mathrm{f}: \; f_1(p_1) + f_2(p_2) \to V'(M, sp) \to Q(p_a) + \bar{Q}(p_b) + \Omega_{gap}(Q_c) + X \,, \quad (5.1)$$

for the production of a heavy quark pair at fixed rapidity difference, $\Delta\eta = \eta_a - \eta_b$. Here the f_i refer to partons that participate in the collision, and we have labeled process (5.1) "f". We sum inclusively over final states, while measuring the energy flow, Q_c, into the rapidity region, Ω_{gap}, in Eq. (5.1). The transverse momentum p_T of a parton $Q(p_a)$ or $\bar{Q}(p_b)$ of mass m_Q in Eq. (5.1) is related to the rapidity difference $\Delta\eta$ according to

$$p_T = \sqrt{\frac{M^2}{4\cosh^2\frac{\Delta\eta}{2}} - m_Q^2} \,. \quad (5.2)$$

As discussed in the introduction, we may expect different patterns of radiation from intermediate resonances if they are distinguished by different gauge content.

The geometry for the gap at a collider is presented schematically in Fig. 5.1, where the gap region is determined by rapidity range Y. The factorization that we will discuss in Sec. 5.2.2 enables us to work perturbatively. The partonic cross section at leading order for process (5.1) involves five external particles. The kinematics of this analysis are described in the Appendix.

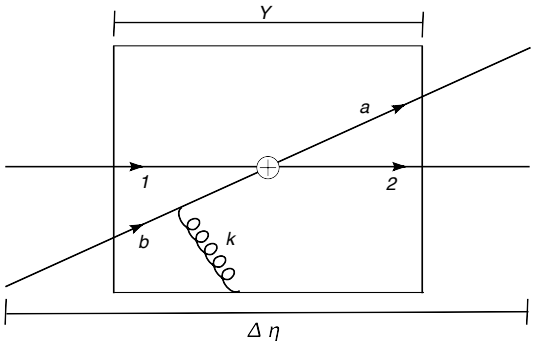

Figure 5.1: Light to heavy process with gluon radiation of momentum k^μ into a rapidity gap. The figure describes $q\bar{q} \to Q\bar{Q}$ process. $\Delta\eta$ is the rapidity difference of a heavy quark pair, $Q(p_a)$ and $\bar{Q}(p_b)$, and Y is the rapidity range of the gap region. 1 and 2 denote the initial partons while a and b denote the final partons.

5.2.2 Factorized and refactorized cross sections

We follow the procedure introduced in Chapter 2.1 for factorized and refactorized cross sections in rapidity gap process. In the following section, we will use Eq. (2.19) to evaluate the gap fraction.

5.2.3 The gap fraction

We define the gap fraction f_{gap} as the ratio of the number of events for heavy quark pair production with a specified rapidity gap to the total number of the pair production events. A gap event was originally identified experimentally by the lack of particle multiplicity in the interjet region [105, 108]. In that case, the multiplicity is determined from the number of calorimeter cells which measure energy deposition above a threshold. A gap event is then defined by the absence of such cells in the rapidity region. Our formulation of the problem is in terms of the transverse energy flow, Q_c, of hadronic radiation carried by the particles [110]. We introduce a variable, energy "gap threshold" Q_0, which is different in principle from the experimental calorimeter threshold, and identify a gap event from the condition of interjet radiation less than Q_0. Then, to get the partonic gap cross section, we evaluate Eq. (2.7) at the value Q_0 for the maximum of interjet energy flow Q_c. The resummed result is given by Eq. (2.19). We note that values of Q_0 at the order of the hard scale p_T would violate the requirement of factorization, since the emission into the gap region would not be soft any more.

To define the gap fraction, we approximate the total cross sections from the LO (Born) partonic cross section, related to Eq. (2.8)

$$\frac{d\hat{\sigma}^{(\mathrm{f},LO)}}{d\Delta\eta} = \sum_{\beta,\gamma} H_{\beta\gamma}^{(\mathrm{f},LO)}(M, m_Q, \Delta\eta, \alpha_s(p_T))\, S_{\gamma\beta}^{(\mathrm{f},0)}\,. \tag{5.3}$$

We may consider the LO and the gap differential partonic cross sections with

respect to M and $\eta_{V'} = \frac{1}{2}\ln\frac{x_1}{x_2}$, given for a resonance by, respectively,

$$\begin{aligned}
&\frac{d\hat{\sigma}^{(\mathrm{f},LO)}\left(M,\, m_Q,\, \Delta\eta,\, \alpha_s(p_T),\, Y\right)}{d\Delta\eta dM^2 d\eta_{V'}} \\
&\qquad = \frac{d\hat{\sigma}^{(\mathrm{f},LO)}}{d\Delta\eta}\delta\left(M^2 - x_1x_2S\right)\delta\left(\eta_{V'} - \frac{1}{2}\ln\frac{x_1}{x_2}\right), \\
&\frac{d\hat{\sigma}^{(\mathrm{f})}\left(M,\, m_Q,\, Q_0,\, \Delta\eta,\, \alpha_s(p_T),\, Y\right)}{d\Delta\eta dM^2 d\eta_{V'}} \\
&\qquad = \frac{d\hat{\sigma}^{(\mathrm{f})}}{d\Delta\eta}\delta\left(M^2 - x_1x_2S\right)\delta\left(\eta_{V'} - \frac{1}{2}\ln\frac{x_1}{x_2}\right), \qquad (5.4)
\end{aligned}$$

which are distinguished by the argument Q_0 in the latter, and where S is the hadronic center of mass energy. Here, the differential with respect to $\eta_{V'}$ corresponds to fixing the center of mass rapidity of the final-state pair in the lab frame. We emphasize that the above condition does not change the description of soft QCD radiation in the soft functions, which depend on the rapidity difference $\Delta\eta$.

We now define the gap fraction at leading order in terms of Eqs. (2.19), (5.3) and (5.4), by

$$f_{gap}^{(LO)} = \frac{\sum_{f_1,f_2}\int dx_1dx_2\phi_{f_1/A}(x_1)\phi_{f_2/B}(x_2)\frac{d\hat{\sigma}^{(\mathrm{f})}\left(M,m_Q,Q_0,\Delta\eta,\alpha_s(p_T),Y\right)}{d\Delta\eta\, dM^2\, d\eta_{V'}}}{\sum_{f_1,f_2}\int dx_1dx_2\phi_{f_1/A}(x_1)\phi_{f_2/B}(x_2)\frac{d\hat{\sigma}^{(\mathrm{f},LO)}\left(M,m_Q,\Delta\eta,\alpha_s(p_T),Y\right)}{d\Delta\eta\, dM^2\, d\eta_{V'}}}. \qquad (5.5)$$

An advantage of using the differential partonic cross sections (5.4) to obtain the gap fraction becomes clear when there is only one partonic initial state for a resonance process. The gap fraction at leading order in Eq. (5.5) for a single partonic channel process is given by

$$f_{gap}^{(LO)}\left(M,\, m_Q,\, Q_0,\, \Delta\eta,\, \alpha_s(p_T),\, Y,\, \eta_{V'}\right) = \frac{\frac{d\hat{\sigma}^{(\mathrm{f})}\left(M,m_Q,Q_0,\Delta\eta,\alpha_s(p_T),Y\right)}{d\Delta\eta}}{\frac{d\hat{\sigma}^{(\mathrm{f},LO)}\left(M,m_Q,\Delta\eta,\alpha_s(p_T),Y\right)}{d\Delta\eta}}, \qquad (5.6)$$

where the PDFs cancel in the ratios of the gap fraction in this case.

5.3 Massive gap soft anomalous dimension matrices

The one-loop soft anomalous dimension matrix, Γ_S, for a rapidity gap process is calculated from the mismatch between real and virtual corrections, generated by imposing a rapidity gap. The soft function is calculated by taking single ultraviolet pole parts from virtual and real corrections, which we will label as $\omega_{V(ij)}$ and $\omega_{R(ij)}$, respectively. The real part, $\omega_{R(ij)}$, comes with a phase space integral outside the gap, where it cancels $\omega_{V(ij)}$. The coefficient of the pole results from the phase space integration inside the rapidity gap region. Here, the single ultraviolet pole arises from the limitation on the energy integration of soft gluons.

In practice, following [32], we construct the gap soft anomalous dimension matrix from a set of integrals, $\omega_{(ij)}$,

$$\gamma_S^{(1)}{}_{(ij)} = \frac{\omega_{(ij)}(-2\varepsilon)}{(\alpha_s/\pi)}\,, \tag{5.7}$$

where we use dimensional regularization, with $D = 4 - 2\varepsilon$. The indices i and j label partons of momenta p_i and p_j, and the $\omega_{(ij)}$ are defined by

$$\begin{aligned}
\omega_{(ij)} &= \omega_{V(ij)} + \omega_{R(ij)} \\
&= -(4\pi\alpha_s)\delta_i\delta_j\Delta_i\Delta_j \int_{P.P.} \frac{d^Dk}{(2\pi)^{D-1}}\delta_+(k^2)\Theta(\vec{k})\frac{(p_i\cdot p_j)}{(p_i\cdot k)(p_j\cdot k)} \\
&\quad +\delta_i\delta_j\Delta_i\Delta_j\frac{\alpha_s}{2\pi}\frac{i\pi}{2\varepsilon}(1-\delta_i\delta_j)\,.
\end{aligned} \tag{5.8}$$

Here the subscript $P.P.$ indicates that the integral is defined by its ultraviolet pole part. We also define $\delta_i = 1(-1)$ for momentum k flowing in the same (opposite) direction as the momentum flow of line i, and $\Delta_i = 1(-1)$ for i a quark (antiquark) line. The function $\Theta(\vec{k}) = 1$ when the vector $\vec{k}$ is directed into a rapidity gap. Equation (5.8) describes the incomplete cancellation between real and virtual gluons from the integration over the geometric phase space of the gap region. Only the part of the phase integration inside the gap survives, and contributes to the soft anomalous dimension matrix for the process.

We express the above integrals in terms of transverse momentum, rapidity,

and azimuthal angle coordinates, with the help of the kinematics described in the Appendix, and use the relations

$$\begin{aligned}\int_{P.P.} d^D k \delta_+(k^2) &= \int_{P.P.} \frac{k_T^{D-3}}{2} dk_T dy d\phi \,, \\ \int_{P.P} \frac{dk_T}{k_T^{1+2\varepsilon}} &= \frac{1}{2\varepsilon} \,. \end{aligned} \tag{5.9}$$

In these terms, the $\omega_{(ij)}$ become

$$\omega_{(ij)} = \left(\frac{\alpha_s}{\pi}\right) \left(- \delta_i \delta_j \Delta_i \Delta_j \frac{1}{2} \frac{1}{2\varepsilon} \int \frac{dy d\phi}{2\pi} \Theta(\vec{k}) \Omega_{ij} + \delta_i \delta_j \Delta_i \Delta_j \frac{i\pi}{2\varepsilon} \frac{(1-\delta_i \delta_j)}{2} \right), \tag{5.10}$$

where we define Ω_{ij} as

$$\Omega_{ij} = \frac{(p_i \cdot p_j) k_T^2}{(p_i \cdot k)(p_j \cdot k)} \,. \tag{5.11}$$

In these coordinates, the Ω_{ij} are given by

$$\begin{aligned}\Omega_{12} &= 2 \,, \\ \Omega_{ab} &= \frac{\rho^2 \cosh \Delta\eta + 1}{\left(\rho \cosh\left(\frac{\Delta\eta}{2} - y\right) - \cos\phi\right)\left(\rho \cosh\left(\frac{\Delta\eta}{2} + y\right) + \cos\phi\right)} \,, \\ \Omega_{1a} &= \frac{\rho\, \epsilon^{-\left(\frac{\Delta\eta}{2} - y\right)}}{\left(\rho \cosh\left(\frac{\Delta\eta}{2} - y\right) - \cos\phi\right)} \,, \\ \Omega_{1b} &= \frac{\rho\, \epsilon^{\left(\frac{\Delta\eta}{2} + y\right)}}{\left(\rho \cosh\left(\frac{\Delta\eta}{2} + y\right) + \cos\phi\right)} \,, \\ \Omega_{2a} &= \frac{\rho\, \epsilon^{\left(\frac{\Delta\eta}{2} - y\right)}}{\left(\rho \cosh\left(\frac{\Delta\eta}{2} - y\right) - \cos\phi\right)} \,, \\ \Omega_{2b} &= \frac{\rho\, \epsilon^{-\left(\frac{\Delta\eta}{2} + y\right)}}{\left(\rho \cosh\left(\frac{\Delta\eta}{2} + y\right) + \cos\phi\right)} \,. \end{aligned} \tag{5.12}$$

We recall that indices 1 and 2 are for initial-state partons, and a and b for final-state partons, as described in Eq. (5.1). The parameter ρ has been defined in Eq. (2.13), and is always larger than one for massive partons and equal to one for the massless case. We will see that all the results we derive here go back

to the previous calculation for massless dijet events, $\rho = 1$ [110, 111].

For complete integrations over the rapidity gap geometry, it is convenient to integrate Ω_{ij} over an azimuthal angle ϕ first. It is then straightforward to evaluate rapidity integrals over a gap region $-Y/2$ to $Y/2$. The final expressions for the ${\gamma_S^{(1)}}_{(ij)}$ of Eq. (5.7) can be found in Eq. (29) of Ref. [27]. We take the massless limit, $\rho = 1$, in Eq. (29) of Ref. [27] to cross-check these results with the previous calculation for massless dijet events, and find [111]

$$\begin{aligned}
{\gamma_S^{(1)}}_{(12)} &= Y - i\pi\,, \\
{\gamma_S^{(1)}}_{(ab)} &= \ln\left(\frac{\sinh\left(\frac{\Delta\eta+Y}{2}\right)}{\sinh\left(\frac{\Delta\eta-Y}{2}\right)}\right) - i\pi\,, \\
{\gamma_S^{(1)}}_{(1a)} &= {\gamma_S^{(1)}}_{(2b)} = \frac{1}{2}\left(\ln\left(\frac{\sinh\left(\frac{\Delta\eta+Y}{2}\right)}{\sinh\left(\frac{\Delta\eta-Y}{2}\right)}\right) - Y\right)\,, \\
{\gamma_S^{(1)}}_{(1b)} &= {\gamma_S^{(1)}}_{(2a)} = -\frac{1}{2}\left(\ln\left(\frac{\sinh\left(\frac{\Delta\eta+Y}{2}\right)}{\sinh\left(\frac{\Delta\eta-Y}{2}\right)}\right) + Y\right)\,.
\end{aligned} \tag{5.13}$$

We can now construct the soft anomalous dimension matrices which depend on the color basis. We use an s-channel singlet-octet basis [48] for quark-antiquark annihilation to a heavy quark pair,

$$c_{singlet} = c_1, \quad c_{octet} = -\frac{1}{2N_c}c_1 + \frac{c_2}{2}\,, \tag{5.14}$$

where c_1 and c_2 are color tensor basis for singlet exchange in the s and t channels,

$$(c_1)_{\{r_i\}} = \delta_{r_1 r_2}\delta_{r_a r_b},\ (c_2)_{\{r_i\}} = \delta_{r_1 r_a}\delta_{r_2 r_b}\,. \tag{5.15}$$

Here, we denote by r_i the color index associated with the incoming or outgoing parton i. The lowest-order soft matrix is the trace of the color basis, $S_{LI}^{(\mathrm{f},0)} = \mathrm{Tr}\,(c_L^\dagger c_I)$, given in singlet-octet basis by

$$S^{(\mathrm{f},0)} = \begin{pmatrix} N_c^2 & 0 \\ 0 & \frac{1}{4}(N_c^2-1) \end{pmatrix}\,, \tag{5.16}$$

which will be used in the resummed cross sections, Eq. (2.19).

To construct the soft anomalous dimension matrix in the color basis (5.14), we rewrite the various one-loop diagrams, using the identity shown in Fig. 5.2:

$$(T_F^a)_{ji}(T_F^a)_{kl} = \frac{1}{2}\left(\delta_{ki}\delta_{jl} - \frac{1}{N_c}\delta_{ji}\delta_{kl}\right) , \tag{5.17}$$

where the T_F^a's are the generators of SU(N_c) in the fundamental representation. In the basis of Eq. (5.14) for the process $q\bar{q} \to Q\bar{Q}$, we derive in this way the

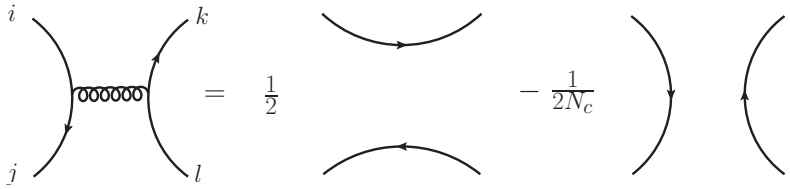

Figure 5.2: Color identity corresponding to Eq. (5.17).

soft anomalous dimension matrix in terms of the integrals $\gamma_{S\,(ij)}^{(1)}$ in Eq. (29) of Ref. [27],

$$\Gamma_S^{(1)(q\bar{q}\to Q\bar{Q})} = \begin{pmatrix} C_F\alpha & \frac{C_F}{2N_c}(\chi+\tau) \\ \chi+\tau & C_F\chi - \frac{1}{2N_c}(2\tau+\alpha+\chi) \end{pmatrix} , \tag{5.18}$$

where α, χ and τ are defined by

$$\begin{aligned} \alpha &\equiv \gamma_{S\,(12)}^{(1)} + \gamma_{S\,(ab)}^{(1)} , \\ \chi &\equiv \gamma_{S\,(1a)}^{(1)} + \gamma_{S\,(2b)}^{(1)} , \\ \tau &\equiv \gamma_{S\,(1b)}^{(1)} + \gamma_{S\,(2a)}^{(1)} . \end{aligned} \tag{5.19}$$

The eigenvectors of $\Gamma_S^{(1)}$ in Eq. (5.18) may be chosen as

$$\begin{aligned} e_1 &= \begin{pmatrix} 1 \\ \frac{4N_c\xi}{\Delta_1+\sqrt{\Delta_1^2+8C_FN_c\xi^2}} \end{pmatrix} , \\ e_2 &= \begin{pmatrix} \frac{\Delta_1-\sqrt{\Delta_1^2+8C_FN_c\xi^2}}{4N_c\xi} \\ 1 \end{pmatrix} , \end{aligned} \tag{5.20}$$

and the corresponding eigenvalues are given by

$$\begin{aligned}
\lambda_1^{(\mathrm{f},1)} &= \frac{\Delta_2 + \sqrt{\Delta_1^2 + 8C_F N_c \xi^2}}{4N_c}\,, \\
\lambda_2^{(\mathrm{f},1)} &= \frac{\Delta_2 - \sqrt{\Delta_1^2 + 8C_F N_c \xi^2}}{4N_c}\,,
\end{aligned} \tag{5.21}$$

where we have defined

$$\begin{aligned}
\Delta_1 &\equiv (\alpha + \chi + 2\tau) + 2C_F N_c(\alpha - \chi)\,, \\
\Delta_2 &\equiv -(\alpha + \chi + 2\tau) + 2C_F N_c(\alpha + \chi)\,, \\
\xi &\equiv (\tau + \chi)\,.
\end{aligned} \tag{5.22}$$

Finally, the transformation matrix R in Eq. (2.14), which diagonalizes the soft anomalous dimension matrix, is given from Eq. (5.20) by

$$(R^{(\mathrm{f})^{-1}})_{J\beta} = \begin{pmatrix} 1 & \frac{\Delta_1 - \sqrt{\Delta_1^2 + 8C_F N_c \xi^2}}{4N_c \xi} \\ \frac{4N_c \xi}{\Delta_1 + \sqrt{\Delta_1^2 + 8C_F N_c \xi^2}} & 1 \end{pmatrix}. \tag{5.23}$$

It was observed in Ref. [110] that for massless partons the above eigenvectors are independent of the rapidity difference $\Delta\eta$, and depend only on the rapidity gap range, Y. However, we find that this is not the case any more for massive quark pair production, $\rho > 1$. As an example, we take the values $\Delta\eta = 2.5$ and $\Delta\eta = 4$ at fixed $m_Q = m_t$, $M = 1.5$ TeV and $Y = 1.5$, and confirm a mild rapidity dependence of the eigenvectors,

$$\begin{aligned}
e_1 &= \begin{pmatrix} 1 \\ -0.098 - 0.269i \end{pmatrix} \text{ for } \Delta\eta = 2.5, \\
e_1 &= \begin{pmatrix} 1 \\ -0.102 - 0.274i \end{pmatrix} \text{ for } \Delta\eta = 4, \\
e_2 &= \begin{pmatrix} 0.022 + 0.060i \\ 1 \end{pmatrix} \text{ for } \Delta\eta = 2.5, \\
e_2 &= \begin{pmatrix} 0.023 + 0.061i \\ 1 \end{pmatrix} \text{ for } \Delta\eta = 4\,.
\end{aligned} \tag{5.24}$$

For these configurations, the first eigenvector, e_1, is close to a color singlet,

while the second, e_2, is close to a color octet. Following the terminology in Ref. [110], we denote the eigenvectors, e_1 and e_2, of Γ_S by "quasi-singlet" and "quasi-octet", respectively.

We will see below that the process $q\bar{q} \to Q\bar{Q}$ is the only relevant partonic channel involving a spin-1 particle resonance, $V'(M, sp = 1)$. For other resonances $V'(M, sp \neq 1)$, we can consider the gluon-induced partonic process

$$g(p_1) + g(p_2) \to V'(M, sp \neq 1) \to Q(p_a) + \bar{Q}(p_b) + \Omega_{\rm gap}(Q_c)\,. \quad (5.25)$$

To describe the color flow in the latter process, a suitable s-channel basis of color tensors has been defined in Ref. [32],

$$\begin{aligned} (c_1)_{\{r_i\}} &= \delta_{r_1 r_2}\delta_{r_a r_b}\,, \\ (c_2)_{\{r_i\}} &= d_{r_1 r_2 c}(T_F^c)_{r_a r_b}\,, \\ (c_3)_{\{r_i\}} &= i f_{r_1 r_2 c}(T_F^c)_{r_a r_b}\,, \end{aligned} \quad (5.26)$$

where c_1 is again the s-channel singlet tensor, and c_2 and c_3 are the symmetric and antisymmetric octet tensors, respectively. In this basis, the anomalous dimension matrix for the process $gg \to Q\bar{Q}$ is found to be [111]

$$\Gamma_S^{(1)(gg\to Q\bar{Q})} = \begin{pmatrix} C_F\,\gamma_S^{(1)}{}_{(ab)} + N_c\,\gamma_S^{(1)}{}_{(12)} & 0 & \frac{1}{2}(\chi+\tau) \\ 0 & N_c\,\zeta & \frac{N_c}{4}(\chi+\tau) \\ \chi+\tau & \frac{N_c^2-4}{4N_c}(\chi+\tau) & N_c\,\zeta \end{pmatrix}, \quad (5.27)$$

where $\zeta \equiv \frac{1}{4}(\chi-\tau) - \frac{1}{2N_c^2}\gamma_S^{(1)}{}_{(ab)} + \frac{1}{2}\gamma_S^{(1)}{}_{(12)}$, and where χ and τ have been defined in Eq. (5.19). In analogy to Eq. (5.16), we derive the zeroth order soft matrix for this process in basis (5.26) as

$$S^{(\rm f,0)} = \begin{pmatrix} N_c(N_c^2-1) & 0 & 0 \\ 0 & \frac{(N_c^2-4)(N_c^2-1)}{2N_c} & 0 \\ 0 & 0 & \frac{N_c(N_c^2-1)}{2} \end{pmatrix}. \quad (5.28)$$

One may now find the corresponding eigenvalues and transformation matrices $R^{(\rm f)^{-1}}$ for $gg \to Q\bar{Q}$. The results are too cumbersome to present here,

but are straightforward to derive and evaluate numerically. In large N_c limit, however, the eigenvectors and the corresponding eigenvalues can be obtained readily, since Eq. (5.27) becomes

$$\Gamma_S^{(1)(gg\to Q\bar{Q})} \simeq N_c \begin{pmatrix} \frac{1}{2}\gamma_S^{(1)}{}_{(ab)} + \gamma_S^{(1)}{}_{(12)} & 0 & 0 \\ 0 & \zeta & \frac{1}{4}(\chi+\tau) \\ 0 & \frac{1}{4}(\chi+\tau) & \zeta \end{pmatrix}, \qquad (5.29)$$

for large N_c. Normalized eigenvectors of $\Gamma_S^{(gg\to Q\bar{Q})}$ in large N_c limit are then

$$e_1 = \begin{pmatrix} 1 \\ 0 \\ 0 \end{pmatrix}, \quad e_2 = \frac{1}{\sqrt{2}} \begin{pmatrix} 0 \\ 1 \\ 1 \end{pmatrix}, \quad e_3 = \frac{1}{\sqrt{2}} \begin{pmatrix} 0 \\ -1 \\ 1 \end{pmatrix}, \qquad (5.30)$$

and the corresponding eigenvalues are given by

$$\begin{aligned} \lambda_1^{(\mathrm{f},1)} &= \left(\frac{1}{2}\gamma_S^{(1)}{}_{(ab)} + \gamma_S^{(1)}{}_{(12)}\right) N_c\,, \\ \lambda_2^{(\mathrm{f},1)} &= \left(\zeta + \frac{1}{4}(\chi+\tau)\right) N_c\,, \\ \lambda_3^{(\mathrm{f},1)} &= \left(\zeta - \frac{1}{4}(\chi+\tau)\right) N_c\,. \end{aligned} \qquad (5.31)$$

We emphasize that, in Eq. (5.30), e_1 is an exact color singlet and that e_2 and e_3 are octet basis vectors. We will not restrict ourselves the above approximation in following sections. We will see, however, in Sec. 5.6 that the explicit results of eigenvalues and eigenvectors for $gg \to Q\bar{Q}$ in the kinematics and the gap geometry we study in this chapter are close to the results of the large N_c limit.

The analysis in this section is based on wide resonances with $\Gamma \sim M$ of decay width, Γ, and resonance mass, M. We note, however, that the energy scale μ of gluon radiation into a gap should be separated into two different regions, depending on the decay widths of heavy resonances. This may lead to different prescriptions for describing soft gluon radiation, depending on μ. For gluon radiation at scale μ, with $Q_0 < \mu < \sqrt{\Gamma M}$, the hard function can be treated as an effective vertex. This is the condition we have used for describing soft gluon radiation in this section, where we assume that the hard

scale p_T is of the same order as $\sqrt{\Gamma M}$. For the case of gluon radiation in the range $\sqrt{\Gamma M} < \mu < M$, direct radiation from the resonance, which was not considered in this section, has to be included in the soft function. In addition to this, the contributions from soft gluon interactions between initial and final state partons are suppressed for both octet and singlet resonance processes if the hard scale falls into the regime $\sqrt{\Gamma M} < \mu < M$. In this chapter, we concentrate on the case that $\sqrt{\Gamma M}$ is of the order of p_T.[1] In general, the decay width of an octet resonance would be large enough to satisfy this condition. For example, a KK gluon above 1 TeV (as required by precision tests) has decay width of about $M_G/6$ [61, 125] in basic RS models, and $0.215 M_G$ [66, 152] in RS models based on extended electroweak gauge symmetry with specific fermion charges and localization that explain the LEP anomaly of the forward-backwardy asymmetry for b quarks. Axigluons or universal colorons have decay width of about $\alpha_s M_G$ [138], resulting in $\sqrt{\Gamma M_G} \sim p_T$ where p_T is the hard scale we have used. On the other hand, the widths of singlet resonances are sensitive to the model parameters for the Z'. A Z' can be very narrow, $\mathcal{O}(10^{-3} M_{Z'})$, or very broad, $\mathcal{O}(M_{Z'})$, in both Topcolor Z' models [153] and in the Little Higgs models [154–157], depending on parameters such as the $SU(2)_1 \otimes SU(2)_2$ mixing angle. In the following sections, our study will be based primarily on the broad widths of heavy resonances, $Q_0 < \mu < \sqrt{\Gamma M}$. We have observed that for narrow resonances we have to evolve μ both from Q_0 to $\sqrt{\Gamma M}$ with the exponents we have obtained in this section and from $\sqrt{\Gamma M}$ to the hard scale with a different analysis. We will discuss briefly how such a narrow singlet resonance can change our results at the end of Sec. 5.6.

5.4 Hard functions

The remaining piece to complete constructing a partonic cross section in Eq. (2.8) is a hard function. Hard functions describe physics at the large momentum scale. In our study, the mechanism of new heavy particle resonances is thus contained in the hard functions, decoupled from soft QCD

[1] In principle, a hard scale for the specific model could be chosen as $\sqrt{\Gamma M}$, the minimum off-shellness of the resonance. The hard scale p_T is suitable in our study since we are interested in a model independent approach and since we consider broad resonances that satisfy $\sqrt{\Gamma M} \sim p_T$ by assumption.

radiation. The direct radiation from an octet resonance can thus be neglected. In the previous section, we have constructed soft functions in the space of color flow at short distances. Thus, it is convenient to construct hard functions in the same basis. In Fig. 5.3, we represent several possible diagrams for the hard part, involving s-channel heavy resonances at lowest order. In the color basis (5.14), the corresponding hard functions for $q\bar{q} \to G/Z' \to Q\bar{Q}$ in Figs. 5.3(a) and 5.3(b) are given by, respectively,

$$(H_G^{(\mathrm{f},LO)})_{KL} = h_G(M,s,t,u) \begin{pmatrix} 0 & 0 \\ 0 & 1 \end{pmatrix} , \tag{5.32}$$

$$(H_{Z'}^{(\mathrm{f},LO)})_{KL} = h_{Z'}(M,s,t,u) \begin{pmatrix} 1 & 0 \\ 0 & 0 \end{pmatrix} . \tag{5.33}$$

A hard function for $gg \to G \to Q\bar{Q}$ in Fig. 5.3(c) such as a KK gluon resonance process [134, 135] would take the form

$$(H_G^{'(\mathrm{f},LO)})_{KL} = h'_G(M,s,t,u) \begin{pmatrix} 0 & 0 & 0 \\ 0 & 0 & 0 \\ 0 & 0 & 1 \end{pmatrix} , \tag{5.34}$$

and for $gg \to Z' \to Q\bar{Q}$ in Fig. 5.3(d) a hard function is given by

$$(H_{Z'}^{'(\mathrm{f},LO)})_{KL} = h'_{Z'}(M,s,t,u) \begin{pmatrix} 1 & 0 & 0 \\ 0 & 0 & 0 \\ 0 & 0 & 0 \end{pmatrix} , \tag{5.35}$$

in the color basis (5.26). The overall functions $h_{G/Z'}(M,s,t,u)$ and $h'_{G/Z'}$ (M,s,t,u) depend on hard scale kinematic variables, M, s, t and u, independent of the gap variables, Q_0 and Y. We note that the spin of the particle V' limits possible partonic cross sections. Specifically, as noted in Refs. [158, 159], the Landau-Yang theorem [160] forbids the creation of a massive state of total angular momentum $J = 1$ from two massless spin-1 particles. Therefore, the gluon-induced production of a spin-1 massive state in Fig. 5.3(c) or 5.3(d) is not allowed if the spin of the resonance is one. Spin-0 singlet or octet resonances

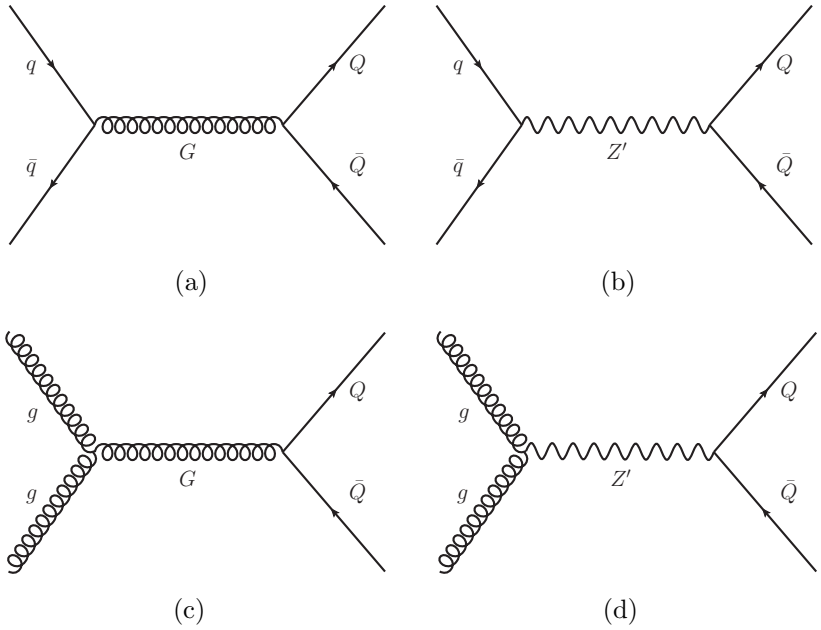

Figure 5.3: Figures (a)-(d) represent the resonance mechanisms for hard functions in Eqs. (5.32), (5.33), (5.34) and (5.35), respectively.

could arise, however, in split SUSY scenarios via gg annihilation. In such cases, $gg \to G/Z'(sp = 0)$ could be the dominant production channel, giving hard functions of the forms, Eqs. (5.34) and (5.35). Also, spin-2 particles $V'(sp = 2)$ such as gravitons and reggeons [161] could be created in s-channel resonances through $gg \to V'(sp = 2) \to Q\bar{Q}$, as well as $q\bar{q} \to V'(sp = 2) \to Q\bar{Q}$. The cross sections for resonances in these cases depend crucially on the model we study. For spin-1 resonance processes, we do not need to know specific coupling strength to the SM particles, because spin-1 G and Z' involve *only* the quark-induced partonic process, $q\bar{q} \to G/Z' \to Q\bar{Q}$. This simplifies the study of the gap fraction. According to the argument in Sec. 5.2.3, the gap fraction at leading logarithm results in the ratio of partonic cross sections (5.6), free from the PDFs that cancel in the ratios. Also, h_G or h_Z of the hard-scattering functions cancels in the ratios (5.6). We can thus study the gap fraction analytically.

In Sec. 5.6, we will discuss how gluon-induced resonances contribute to the gap fraction in massive spin-0 or 2 resonance processes. For a complete study of the gap fraction in this case, we should combine all the possible partonic processes that depend on the specific model. In addition to these, we must

convolute the partonic level results with PDFs, following Eq. (2.5). We leave this study for a further project.

To obtain the partonic cross section in Eq. (2.19), hard functions in Eqs. (5.32), (5.33), (5.34), and (5.35) are transformed to $(H^{(\mathrm{f},LO)})_{\gamma\beta}$ through Eq. (2.16) in the color basis that diagonalizes $\Gamma_S^{(\mathrm{f})}$ in Eq. (2.14). We will study explicitly how partonic cross sections and gap fractions are evaluated in the following sections.

5.5 Gap fractions for spin-1 resonances

From the previous sections, we have all the tools necessary for the evaluation of the partonic cross section in Eq. (2.19). As mentioned above, the main quantity we focus on is the gap fraction (5.5). For spin-1 resonances, we can limit ourselves to quark-induced resonances, shown in Figs. 5.3(a) and 5.3(b), following the argument in Sec. 5.4. The partonic cross section for heavy quark production via G or Z' resonances is

$$\frac{d\hat{\sigma}^{(\mathrm{f})}_{G/Z'}}{d\Delta\eta} = \sum_{\beta,\gamma} (H^{(\mathrm{f},LO)}_{G/Z'})_{\beta\gamma}(M, m_Q, \Delta\eta, \alpha_s(p_T))\, S^{(\mathrm{f},0)}_{\gamma\beta} \left[\frac{\ln\left(\frac{Q_0}{\Lambda}\right)}{\ln\left(\frac{p_T}{\Lambda}\right)}\right]^{E^{(\mathrm{f})}_{\gamma\beta}} , \tag{5.36}$$

where the $(H^{(\mathrm{f},LO)}_{G/Z'})_{\beta\gamma}$ are hard functions written in the basis that diagonalizes the soft anomalous dimension matrix. We will implement Eq. (5.36) in numerical studies below. Following Eq. (2.16), to obtain $(H^{(\mathrm{f},LO)}_{G/Z'})_{\beta\gamma}$, we transform the hard functions in Eqs. (5.32) and (5.33), through matrix R given explicitly in Eq. (5.23). The soft matrix $S^{(\mathrm{f},0)}_{\gamma\beta}$ is obtained by transforming Eq. (5.16) through the same matrix R. Finally, the exponents $E^{(\mathrm{f})}_{\alpha\beta}$ that appear in the cross sections (5.36) are given by Eq. (2.18).

In Eq. (5.36), we observe that the Q_0-dependent factor, $\left[\ln\left(\frac{Q_0}{\Lambda}\right) / \ln\left(\frac{p_T}{\Lambda}\right)\right]^{E^{(\mathrm{f})}_{\gamma\beta}}$, is larger at fixed Q_0 for smaller $E^{(\mathrm{f})}_{\gamma\beta}$, because $\left[\ln\left(\frac{Q_0}{\Lambda}\right) / \ln\left(\frac{p_T}{\Lambda}\right)\right]$ is less than one for $Q_0 < p_T$. Note that we apply Eq. (5.36) only for $Q_0 < p_T$. A constraint for the maximum value of $\Delta\eta$ is obtained from ρ in Eq. (2.13),

$$Y < \Delta\eta < 2\cosh^{-1}\left(\frac{M}{2m_Q}\right) . \tag{5.37}$$

Recall that the gap fraction measures the fraction of events for which the radiated transverse energy is less than or equal to the gap threshold Q_0. For any $E^{(\mathrm{f})}_{\alpha\beta} > 0$, the fraction vanishes for $Q_0 = \Lambda$, and approaches unity for $Q_0 = p_T$, where we choose $\mu = p_T$ in numerical calculations. The soft anomalous dimension matrix for this analysis is given by Eq. (5.18). Representative numerical values of the real and imaginary parts of the eigenvalues are shown in Fig. 5.4 as a function of gap size Y. The corresponding exponents at fixed Y are shown in Fig. 5.5 as a function of $\Delta\eta$. Only the real parts enter the cross section. Imaginary parts are shown for completeness. Qualitatively, in Figs. 5.4 and 5.5, we see that the eigenvalues and the corresponding exponents are larger for larger Y and for smaller $\Delta\eta$. In Fig. 5.4, we observe that for Y

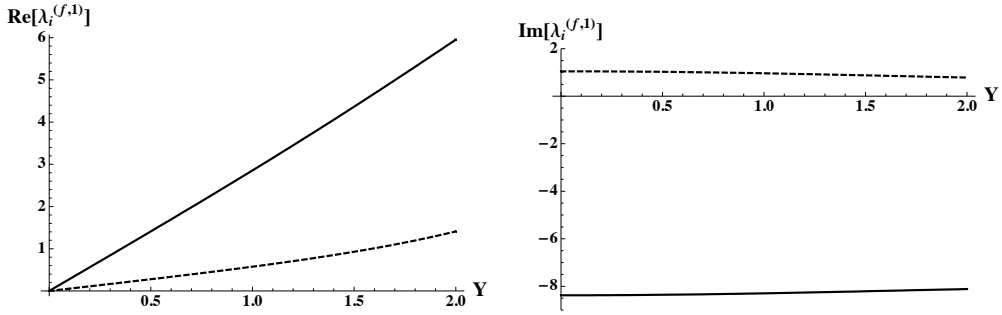

(a) (b)

Figure 5.4: Plot of the real (a) and imaginary (b) parts of the eigenvalues of the soft anomalous dimension matrix in Eq. (5.18) for $q\bar{q} \to Q\bar{Q}$, as a function of Y for $M = 1.5$ TeV, $\Delta\eta = 2.5$ and $m_Q = m_t$. The solid line identifies the quasi-singlet eigenvalue, $\lambda_1^{(\mathrm{f},1)}$, the dashed line, quasi-octet, $\lambda_2^{(\mathrm{f},1)}$, in Eq. (5.20).

of order unity, $\mathrm{Re}[\lambda_1]$ is much larger than $\mathrm{Re}[\lambda_2]$, leading to $E^{(\mathrm{f})}_{22} < 1 < E^{(\mathrm{f})}_{11}$, as shown in Fig. 5.5. Following the discussion below Eq. (5.36), a smaller value of the exponent $E^{(\mathrm{f})}_{22}$ enhances the factor $\left[\ln\left(\frac{Q_0}{\Lambda}\right) / \ln\left(\frac{p_T}{\Lambda}\right)\right]^{E^{(\mathrm{f})}_{22}}$ in the partonic cross section (5.36) relative to a larger value. We note that off-diagnal contributions are small.

The resulting gap fractions for two different spin-1 resonances, Z' and G, of mass 2 TeV, 1.5 TeV, 750 GeV, and 550 GeV are illustrated as functions of Q_0 in Fig. 5.6 as the solid and the dashed curves for a top pair, and as the dot-dashed and the dotted curves (blue) for a bottom pair at fixed $Y = 1.5$ and $\Delta\eta = 2$. The ratios of gap fractions, $f^G_{gap}/f^{Z'}_{gap}$, are shown in Fig. 5.7 at fixed $Q_0 = 5$ GeV in terms of Y and $\Delta\eta$ for $M = 1.5$ TeV and 750 GeV.

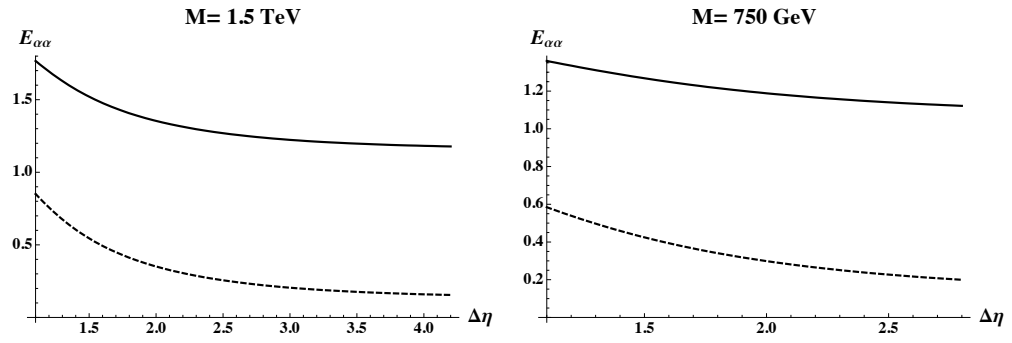

(a) (b)

Figure 5.5: Plot of the exponents, $E^{(\mathrm{f})}_{\alpha\alpha}$, of the soft anomalous dimension matrix for $q\bar{q} \to Q\bar{Q}$, as a function of $\Delta\eta$ for $Y = 1$ and $m_Q = m_t$ with resonance mass $M = 1.5$ TeV and $M = 750$ GeV for (a) and (b), respectively. The solid lines identify the quasi-singlet exponent, $E^{(\mathrm{f})}_{11}$, the dashed lines, quasi-octet, $E^{(\mathrm{f})}_{22}$, obtained from Eq. (2.18).

We observe that for the ratios the dependence on $\Delta\eta$ is negligible at fixed Y. Also, Fig. 5.7 shows that these ratios get larger at fixed Q_0 as the gap range increases.

In Figs. 5.8 and 5.9, the gap fractions and their ratios are presented as functions of Q_0 and Y for $M = 1.5$ TeV and 750 GeV, respectively. The gap fraction for an octet resonance increases rapidly for small values of Q_0 in comparison to a singlet resonance for any gap size. Many fewer events are accumulated at low Q_0 through a color-singlet resonance than for a color-octet resonance. For instance, at $Q_0 = 3$ GeV and $V'(1.5\ \mathrm{TeV}, sp = 1)$ in Fig. 5.6(b), we obtain gap fractions of 12% and 54% for color-singlet and -octet resonances, respectively. The figures also show that the ratios are larger for larger M and Y.

We can interpret these results as follows. As we saw in Eq. (5.24) of Sec. 5.3, the eigenvectors, e_1 and e_2, of the soft anomalous dimension matrix for $q\bar{q} \to Q\bar{Q}$ are very close to a color singlet and a color octet for the kinematics and the gap geometry we study in this section. For this reason, we have called them "quasi-singlet" and "quasi-octet" eigenvectors, respectively. Consequently, this leads the hard functions in Eqs. (5.32) and (5.33) to retain approximately their color basis dependence even after transforming the functions to the diagonal basis.

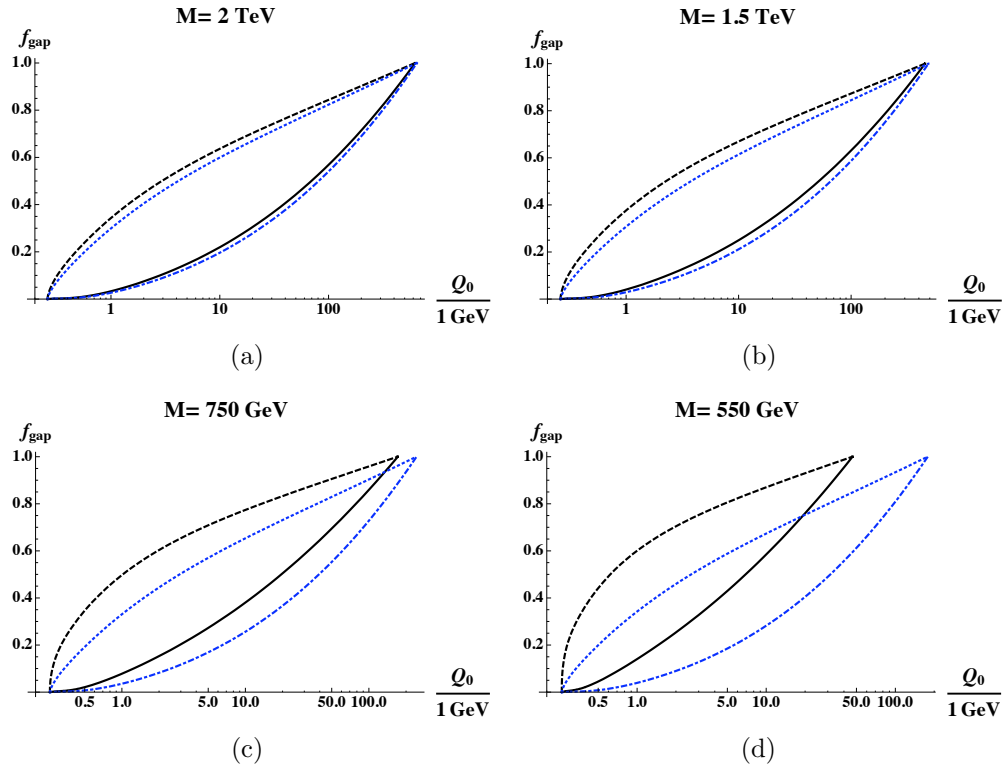

(a) (b) (c) (d)

Figure 5.6: The fractions for gaps identified by the energy threshold Q_0 at $\Delta\eta = 2$ and $Y = 1.5$ for resonance masses $M = 2$, 1.5, 0.75, and 0.55 TeV. In the above figures, the solid curves describe the gap fraction through a Z' resonance (color-singlet), and the dashed curves throughout a G resonance (color-octet) into a *top* quark pair. The dot-dashed curves (blue) describe the gap fraction through a Z' resonance (color-singlet), and the dotted curves (blue) throughout a G resonance (color-octet) into a *bottom* pair.

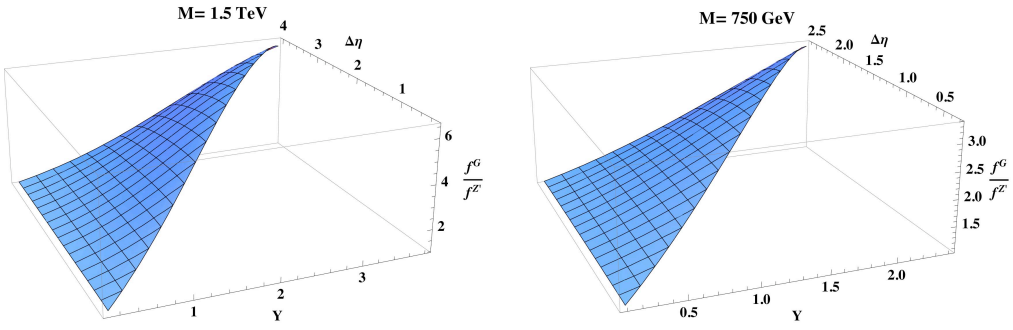

(a) (b)

Figure 5.7: The ratios of two different gap fractions, $f^G_{gap}/f^{Z'}_{gap}$, as functions of Y and $\Delta\eta$ at fixed $Q_0 = 5$ GeV are shown (a) for $M = 1.5$ TeV and (b) $M = 750$ GeV, respectively.

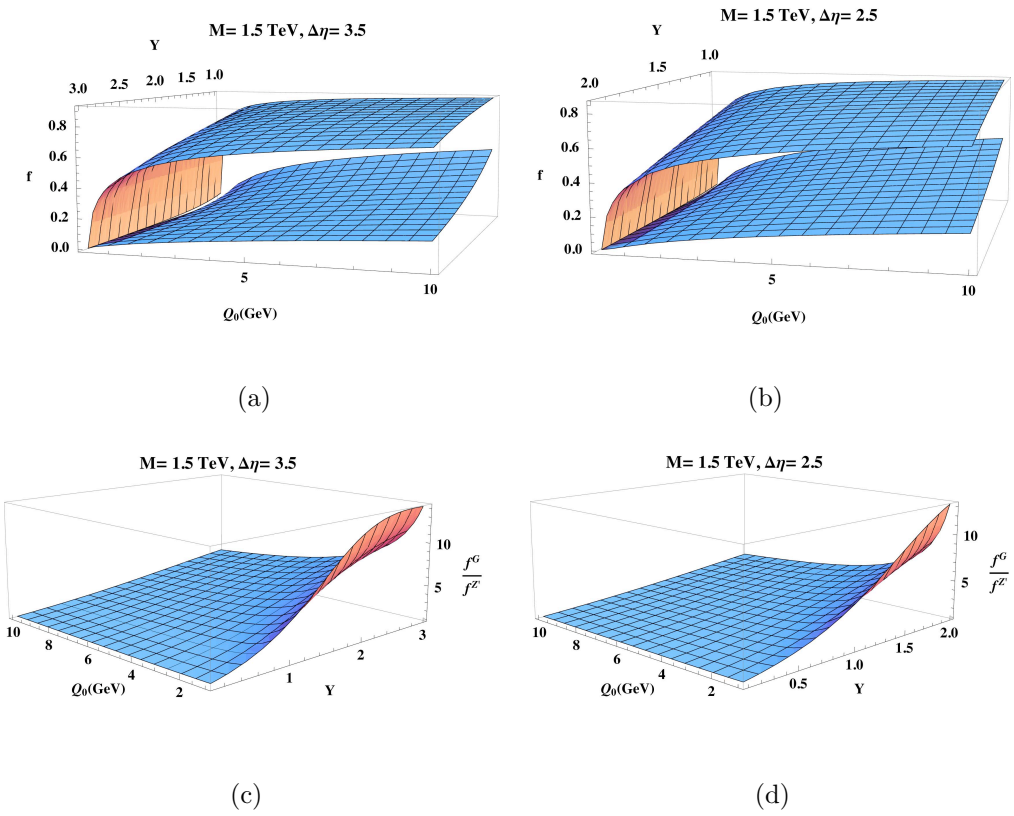

(a) (b)

(c) (d)

Figure 5.8: Gap fractions as functions of energy threshold Q_0 and gap range Y from a resonance of $M = 1.5$ TeV, (a) for $\Delta\eta = 3.5$ and (b) for $\Delta\eta = 2.5$. The lower surfaces in (a) and (b) describe the gap fractions through a Z' resonance (color-singlet), the upper surfaces throughout a G resonance (color-octet) decaying into a top quark pair. The ratios of the gap fraction for an octet resonance to the gap fraction for a singlet resonance are illustrated in (c) and (d) as functions of Q_0 and Y.

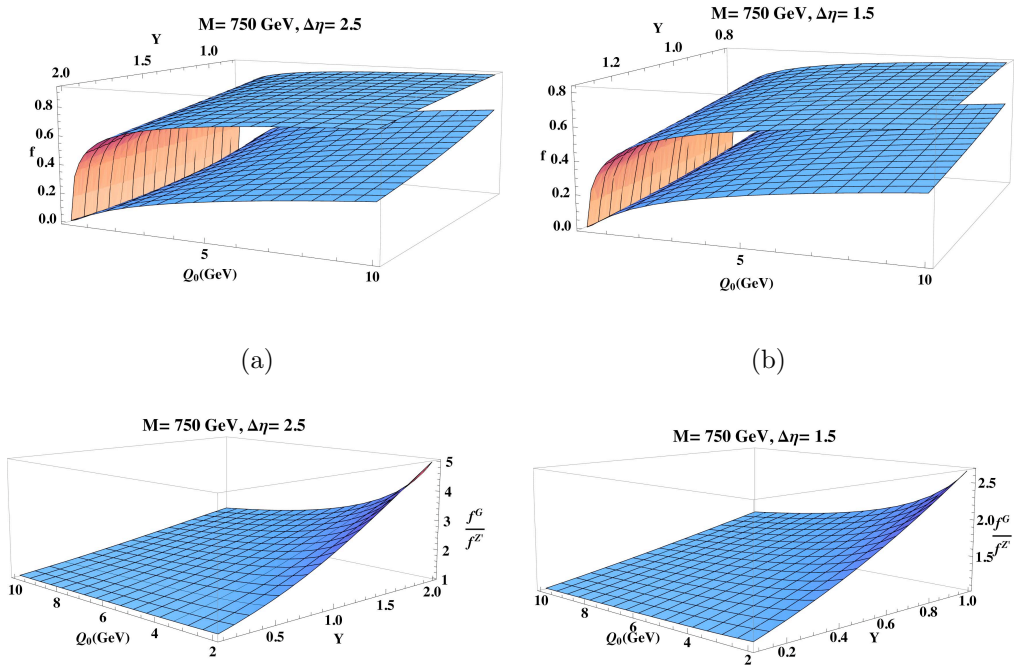

(a) (b)

(c) (d)

Figure 5.9: Same as Fig. 5.8, for $M = 750$ GeV, in the allowed region in gap size Y.

Following the above property of the hard functions and the eigenvalues, shown in Fig. 5.4(a) for $q\bar{q} \to Q\bar{Q}$, the quasi-octet component of the hard function for a color octet resonance is the leading component, with a corresponding small exponent, $E_{22}^{(\mathrm{f})}$. We thus find that the quasi-octet cross section $(H_G^{(\mathrm{f},LO)})_{22} S_{22}^{(\mathrm{f},0)} \left[\frac{\ln\left(\frac{Q_0}{\Lambda}\right)}{\ln\left(\frac{p_T}{\Lambda}\right)}\right]^{E_{22}^{(\mathrm{f})}}$ is dominant in the partonic gap cross section (5.36) for an octet resonance G. The quasi-octet cross section is enhanced due to its large overlap with the color-octet basis which gives a small exponent $E_{22} < 1$. It is clear that this term produces the "convex" shapes of the dashed gap fraction curves (f_{gap}) of the log plot on the x-axis, as shown in Fig. 5.6, and the upper surfaces in Figs. 5.8 and 5.9 for top pair production. These curves rise rapidly at low Q_0.

The singlet resonance process, on the other hand, has a larger overlap with the quasi-singlet component of the hard function. The eigenvalue of the quasi-singlet is larger than one, and $E_{11}^{(\mathrm{f})} = (4/\beta_0)\mathrm{Re}\,\lambda_1^{(\mathrm{f},1)} > 1$. Thus, the quasi-singlet cross section, $(H_{Z'}^{(\mathrm{f},LO)})_{11} S_{11}^{(\mathrm{f},0)} \left[\frac{\ln\left(\frac{Q_0}{\Lambda}\right)}{\ln\left(\frac{p_T}{\Lambda}\right)}\right]^{E_{11}^{(\mathrm{f})}}$, is suppressed at low Q_0, explaining the "concave" shapes of the solid lines in Fig. 5.6 and the lower surfaces in Figs. 5.8 and 5.9 for top pair production. These increase slowly at low Q_0. The differential partonic cross sections with respect to Q_c are presented in Fig. 5.10 for octet and singlet resonance processes for values $M = 1.5$ TeV, $\Delta\eta = 2.5$, and $Y = 1.5$. The behavior of the exponents corresponds to the dominance of the octet resonance process at low Q_c in Fig. 5.10.

The gap fraction depends on the quark mass, m_Q, through the variable ρ in Eq. (2.13). The dependence can be seen in Fig. 5.6 by comparing the black curves (solid and dashed) for a top pair with the blue curves (dotted and dot-dashed) for a bottom pair. For the b quark, the gap fractions are slightly smaller at fixed gap threshold energy than for a top quark pair for the relatively heavy resonances in Fig. 5.6. This difference is, however, larger for smaller resonance mass, as also shown in Fig. 5.6. We note that the quark mass dependence on the gap fraction for bottom quark pair production is negligible even for a resonance of relatively low mass, but not for a top pair. For instance, we obtain $\rho = 1.0003$ for bottom pair production via a resonance of $M = 550$ GeV with $\Delta\eta = 2$, while $\rho = 3.8200$ for a top pair. This results

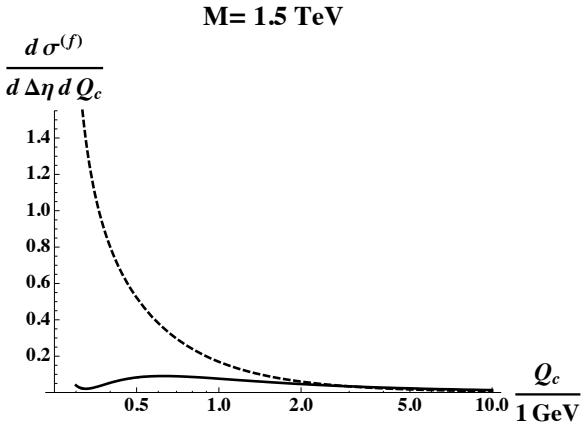

Figure 5.10: The cross section from the octet resonance (dashed line) and the singlet resonance (solid line) for $M = 1.5$ TeV, $\Delta\eta = 2.5$, and $Y = 1.5$. Both distributions are normalized to the same area for the range of $\Lambda < Q_c < p_T$.

in the very different shapes of the black curves compared to the blue curves in Fig. 5.6(d).

The results in this section show that the measurement of gap fractions can be an effective tool to identify the color content of a spin-1 s-channel resonance. In the next section, we study gap fractions for spin-0 or 2 resonance processes, which contain more partonic channels.

5.6 Gap fractions for spin-0 or 2 resonances

As we discussed briefly in Sec. 5.4, in several models of new physics, there are s-channel spin-0 and spin-2 resonances, decaying into a heavy quark pair, which can be produced, through gluon-induced processes in addition to quark-antiquark reactions. We readily recognize that spin-0 or 2 resonance processes might lead to a different pattern of soft gluon radiation between the Tevatron and the LHC, because of the presence of both quark and gluon-induced partonic processes. As we shall see, PDFs no longer cancel in the leading order gap fraction. This is distinguished from the analysis in Sec. 5.5 for spin-1 resonances, involving only one partonic channel. The results in Sec. 5.5 are energy-independent, at leading order, applying to both the Tevatron and the LHC.

Let's assume that there are two partonic processes that produce a heavy

resonance, decaying into a heavy quark pair, $\mathrm{f}_1 : q\bar{q} \to V' \to Q\bar{Q}$ and $\mathrm{f}_2 : gg \to V' \to Q\bar{Q}$. In addition, we assume for simplicity that the coupling of light quarks is universal. Recall that the process f_2 cannot occur for a spin-1 resonance in general. Therefore, we consider the octet resonance as spin-0 or 2. In this case, we obtain the gap fraction, following Eq. (5.5),

$$f_{gap}^{(LO)} = p^{q\bar{q}\to Q\bar{Q}} f_{gap}^{q\bar{q}\to Q\bar{Q}} + p^{gg\to Q\bar{Q}} f_{gap}^{gg\to Q\bar{Q}}, \tag{5.38}$$

where the p^{f_i} are defined by

$$\begin{aligned} p^{q\bar{q}\to Q\bar{Q}} &\equiv \frac{\frac{d\hat{\sigma}^{(\mathrm{f}_1,LO)}}{d\Delta\eta}\left(\sum_{f_1 f_2}\phi_{f_1/A}(x_1)\phi_{f_2/B}(x_2)\right)}{\frac{d\hat{\sigma}^{(\mathrm{f}_1,LO)}}{d\Delta\eta}\left(\sum_{f_1 f_2}\phi_{f_1/A}(x_1)\phi_{f_2/B}(x_2)\right) + \frac{d\hat{\sigma}^{(\mathrm{f}_2,LO)}}{d\Delta\eta}\phi_{f_g/A}(x_1)\phi_{f_g/B}(x_2)}, \\ p^{gg\to Q\bar{Q}} &\equiv \frac{\frac{d\hat{\sigma}^{(\mathrm{f}_2,LO)}}{d\Delta\eta}\phi_{g/A}(x_1)\phi_{g/B}(x_2)}{\frac{d\hat{\sigma}^{(\mathrm{f}_1,LO)}}{d\Delta\eta}\left(\sum_{f_1 f_2}\phi_{f_1/A}(x_1)\phi_{f_2/B}(x_2)\right) + \frac{d\hat{\sigma}^{(\mathrm{f}_2,LO)}}{d\Delta\eta}\phi_{f_g/A}(x_1)\phi_{f_g/B}(x_2)}, \end{aligned} \tag{5.39}$$

and the gap fractions, $f_{gap}^{q\bar{q}\to Q\bar{Q}}$ and $f_{gap}^{gg\to Q\bar{Q}}$, are given by

$$f_{gap}^{q\bar{q}\to Q\bar{Q}}(Q_0) = \frac{\frac{d\hat{\sigma}^{(\mathrm{f}_1)}(Q_0)}{d\Delta\eta}}{\frac{d\hat{\sigma}^{(\mathrm{f}_1,LO)}}{d\Delta\eta}}, \quad f_{gap}^{gg\to Q\bar{Q}}(Q_0) = \frac{\frac{d\hat{\sigma}^{(\mathrm{f}_2)}(Q_0)}{d\Delta\eta}}{\frac{d\hat{\sigma}^{(\mathrm{f}_2,LO)}}{d\Delta\eta}}, \tag{5.40}$$

which can be calculated perturbatively, following Eqs. (2.19) and (5.3). We can interpret the p^{f_i} as the probability for the process f_i among the channels, $p^{q\bar{q}\to Q\bar{Q}} + p^{gg\to Q\bar{Q}} = 1$.

We can study the above gap fraction for representative choices of $p^{q\bar{q}\to Q\bar{Q}}$ and $p^{gg\to Q\bar{Q}}$. For the first example, we compare the gap fraction for an octet resonance with the gap fraction for a singlet resonance through a pure gluon-induced process, $p^{gg\to Q\bar{Q}} = 1$ and $p^{q\bar{q}\to Q\bar{Q}} = 0$. A pseudo-scalar or a boson-phobic scalar resonance is a good example for the above resonance process, where gluon-induced processes are dominant and the branching ratio to a top pair can be taken to be unity [77]. In general, SUSY models with this feature can be constructed for singlet resonances [162], and split SUSY scenarios can explain octet resonances from bound states of meta-stable gluinos [163].

The gap fractions for the pure gluon-induced resonances are determined

by the soft anomalous dimension matrix in Eq. (5.27), its eigenvalues and eigenvectors for the process $gg \to Q\bar{Q}$. The resulting gap fractions for octet and singlet resonances are illustrated in Fig. 5.11(a) for $M = 1.5$ TeV, $\Delta\eta = 2.5$, and $Y = 1$.

To study the effect of an admixture of quark- and gluon-induced processes, the gap fraction for an octet resonance with $p^{gg\to Q\bar{Q}} = 0.8$ and $p^{q\bar{q}\to Q\bar{Q}} = 0.2$ is represented in Fig. 5.11(b) as a dashed curve in comparison to the gap fraction for the pure gluon-induced singlet resonance, shown as a solid curve in the same figure. This quark/gluon admixture for an octet resonance can occur for the reggeon resonances of Ref. [161].

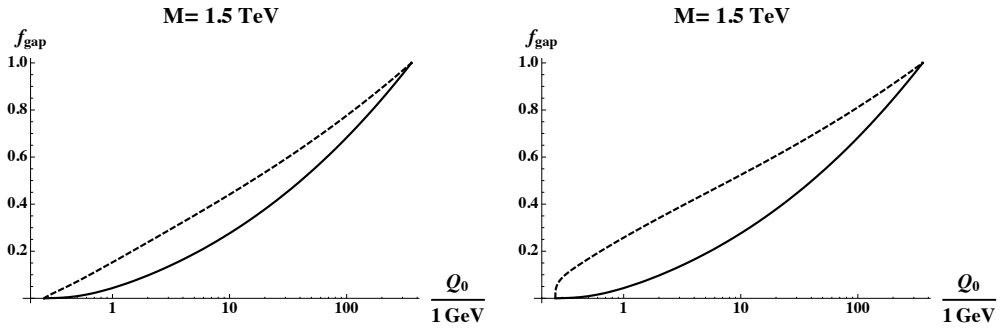

(a) (b)

Figure 5.11: Gap fraction as a function of gap energy threshold Q_0 at $\Delta\eta = 2.5$ with $M = 1.5$ TeV and $Y = 1$. In (a) and (b), the solid lines describe the gap fraction through a Z' resonance (color-singlet) for $p^{gg\to Q\bar{Q}} = 1$. The dashed line describes the gap fraction through a G resonance (color-octet) in (a) for $p^{gg\to Q\bar{Q}} = 1$ and in (b) for $p^{gg\to Q\bar{Q}} = 0.8$ and $p^{q\bar{q}\to Q\bar{Q}} = 0.2$.

As observed in the previous section, we again see in Fig. 5.11(a) that there is "less" radiation into the gap region for the color-octet resonance process. At the same time, we notice that for the same resonances there is "more" radiation for gluon-induced processes than for quark-induced processes. This can be seen by comparing solid and dashed curves in Fig. 5.6 with the curves in Fig. 5.11(a).

Scattered gluons tend to emit more radiation, compared to scattered quarks. We note that the shape of the gap fraction for gluon-induced octet resonances in Fig. 5.11(a) is "linear", while the shape for quark-induced octet resonances in Fig. 5.6 is "convex". Following the arguments in the previous section, the values of the exponents for gluon-induced processes in Fig. 5.12 can account

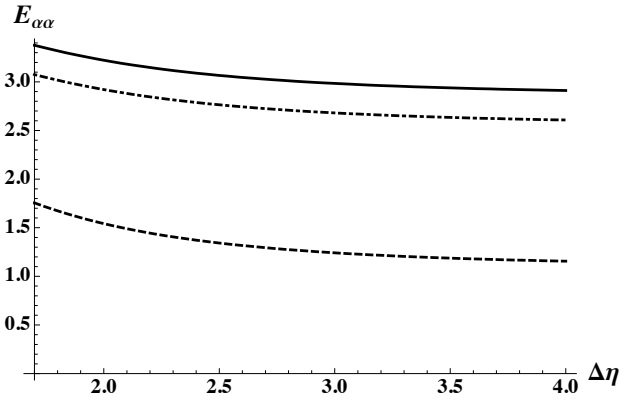

Figure 5.12: Plot of the exponents, $E^{(\mathrm{f})}_{\alpha\alpha}$, of the soft anomalous dimension matrix for $gg \to Q\bar{Q}$ as a function of $\Delta\eta$ for $Y = 1.5$ and $m_Q = m_t$ with resonance mass $M = 1.5$ TeV. The solid line identifies the quasi-singlet exponent, the dashed and the dot-dashed lines the two quasi-octets.

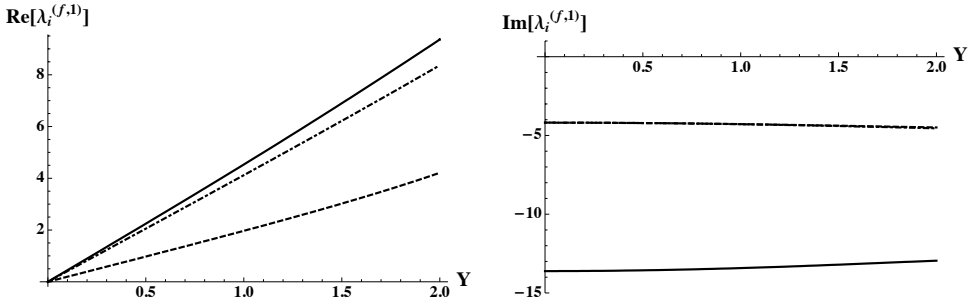

(a) (b)

Figure 5.13: Plot of the real (a) and imaginary (b) parts of the eigenvalues of the soft anomalous dimension matrix for $gg \to Q\bar{Q}$ of $M = 1.5$ TeV, $\Delta\eta = 2.5$ and $m_Q = m_t$. The solid line identifies the quasi-singlet eigenvalue, the dashed and the dot-dashed lines the two quasi-octets.

for the difference. The eigenvalues for the process $gg \to Q\bar{Q}$ in Fig. 5.13 ensure that all exponents $E_{\alpha\beta}^{(gg\to Q\bar{Q})}$ are larger than one for Y of order unity, as shown in Fig. 5.12. We note that two quasi-octet eigenvectors, e_2 and e_3, of $\Gamma_S^{(gg\to Q\bar{Q})}$ in Eq. (5.27), which we recall are determined numerically, turn out to approach e_2 and e_3 in Eq. (5.30), obatined in large N_c limit. As a result, both the quasi-octet components, $(H_G')_{22}$ and $(H_G')_{33}$, of the octet hard function, written in the basis that diagonalizes $\Gamma_S^{(1)(gg\to Q\bar{Q})}$, are important. Their exponents, $E_{22}^{(gg\to Q\bar{Q})}$ and $E_{33}^{(gg\to Q\bar{Q})}$, are shown as the dashed and the dot-dashed lines in Fig. 5.12. An interesting feature is that one of the quasi-octet exponents is close to the exponent for a quasi-singlet. A semi-numerical expression for the cross section (2.19) for gluon-induced octet resonances is given for $M = 1.5$ TeV, $Y = 1$, and $\Delta\eta = 1.5$ by

$$\begin{aligned}\frac{d\hat{\sigma}_G^{(gg\to Q\bar{Q})}}{d\Delta\eta} &= \sum_{\beta,\gamma} (H_G^{'(\mathrm{f}_2,LO)})_{\beta\gamma}\, S_{\gamma\beta}^{(\mathrm{f}_2,0)} \left[\frac{\ln\left(\frac{Q_0}{\Lambda}\right)}{\ln\left(\frac{p_T}{\Lambda}\right)}\right]^{E_{\gamma\beta}^{(\mathrm{f})}} \qquad (5.41)\\ &\simeq h_G' \left((0.23) \left[\frac{\ln\left(\frac{Q_0}{\Lambda}\right)}{\ln\left(\frac{p_T}{\Lambda}\right)}\right]^{2.27} + (6.19) \left[\frac{\ln\left(\frac{Q_0}{\Lambda}\right)}{\ln\left(\frac{p_T}{\Lambda}\right)}\right]^{2.08} + (6.33) \left[\frac{\ln\left(\frac{Q_0}{\Lambda}\right)}{\ln\left(\frac{p_T}{\Lambda}\right)}\right]^{1.17} \right),\end{aligned}$$

where the first coefficient, 0.23, of second line in Eq. (5.41) is $(H_G^{'(\mathrm{f}_2,LO)})_{11} S_{11}^{(\mathrm{f}_2,0)}$, and the other two, 6.19 and 6.33, are $(H_G^{'(\mathrm{f}_2,LO)})_{22} S_{22}^{(\mathrm{f}_2,0)}$ and $(H_G^{'(\mathrm{f}_2,LO)})_{33} S_{33}^{(\mathrm{f}_2,0)}$, respectively. Here h_G' has been defined in Eq. (5.34). In Eq. (5.41), we omit off-diagonal contributions such as $(H_G^{'(\mathrm{f}_2,LO)})_{23} S_{32}^{(\mathrm{f}_2,0)}$, because they contribute less than 2% of the total. We observe that each Q_0-dependent factor, $\left[\ln\left(\frac{Q_0}{\Lambda}\right) / \ln\left(\frac{p_T}{\Lambda}\right)\right]^{E_{\alpha\beta}^{(gg\to Q\bar{Q})}}$, is thus suppressed, relative to linear behavior in a log plot at low Q_0, for all quasi-octet exponents in the partonic cross section (5.41). This explains why the dashed curve in Fig. 5.11(a) increases slowly at low Q_0 compared to the dashed curves in Fig. 5.6(b).

In Fig. 5.11, the dashed curve for a pure gluon-induced process in (a) shows a smaller gap fraction than the dashed curve for a mixed quark-gluon process in (b) for given Q_0. As we discussed in the previous section, the gap fraction for $q\bar{q} \to Q\bar{Q}$ rises rapidly at low Q_0. The term, $f_{gap}^{q\bar{q}\to Q\bar{Q}}$, even with the small assumed probability $p^{q\bar{q}\to Q\bar{Q}} = 0.2$ thus explains the difference of the dashed curves in Fig. 5.11. We note that the shape of the solid curves for $gg \to Z' \to Q\bar{Q}$ in Fig. 5.11 corresponds to the largest amount of radiation

among the resonance processes we have studied in this chapter. This is due to the large quasi-singlet exponent $E_{11}^{(gg\to Q\bar{Q})}$, compared to other exponents.

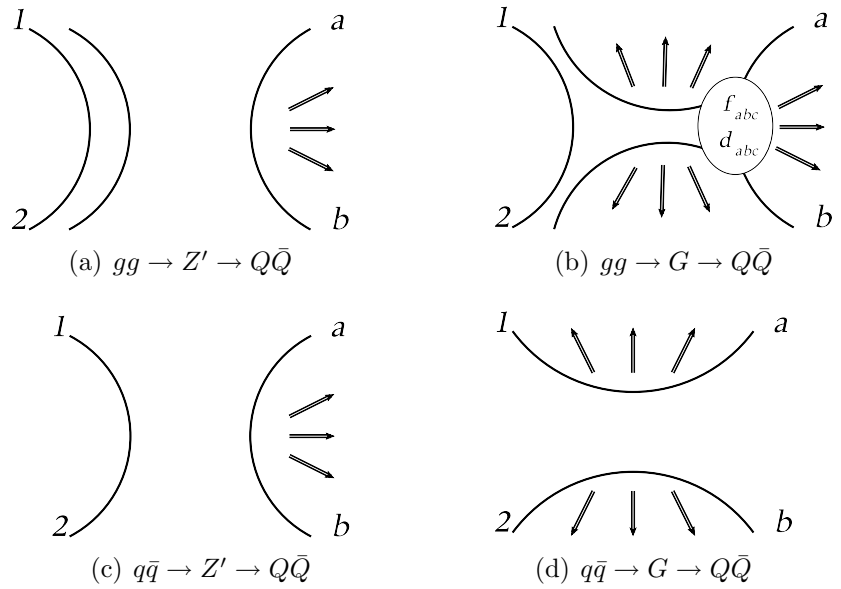

(a) $gg \to Z' \to Q\bar{Q}$ (b) $gg \to G \to Q\bar{Q}$

(c) $q\bar{q} \to Z' \to Q\bar{Q}$ (d) $q\bar{q} \to G \to Q\bar{Q}$

Figure 5.14: Color dipole configurations for resonance processes, $f_1(p_1) + f_2(p_2) \to V' \to Q(p_a) + \bar{Q}(p_b)$. Arrows in each figure represent the enhanced direction of radiation.

The above results, depending on partonic channels and the gauge content of resonances, can be understood intuitively in terms of color dipole configurations. In Fig. 5.14, the color dipole structures and the preferred directions of radiation are represented as solid curves and arrows, respectively. Each figure describes the surplus of radiation inside a dipole [146–148]. For examples, the dipole configurations in Figs. 5.14(a) and 5.14(c) allow more radiation into the $Q\bar{Q}$ region, which overlaps the gap region, while the configuration for $q\bar{q} \to G \to Q\bar{Q}$ in Fig. 5.14(d) describes enhanced radiation in the qQ and the $\bar{q}\bar{Q}$ regions that are outside the gap region. In Fig. 5.14(b), the color-(anti)symmetric couplings control the dipole configuration, which results in radiation into both the qQ and the $Q\bar{Q}$ regions. We have also predicted the least(most) amount of radiation into the gap region for $q\bar{q} \to G \to Q\bar{Q}$ ($gg \to Z' \to Q\bar{Q}$). These color dipole configurations help explain our results for the patterns of radiation, associated with the SU(3) color representation of resonances and the partonic channels involved.

At the end of Sec. 5.3, we argued that for a narrow resonance, generally

a gauge singlet, there is an additional contribution when the radiation energy scale is larger than $\sqrt{\Gamma M}$. In this limit, we expect that the color dipole configuration is further dominant since the process becomes a pure color singlet decay. This contribution is expected to be absent for an octet resonance since the width is in general large. We point out that this may result in more radiation for a very narrow singlet resonance process compared to our results in Secs. 5.5 and 5.6, leading an even more distinguishable difference from an octet resonance process. The details of this case are left for future work.

5.7 Conclusions

In this chapter, we have shown that it may be possible to determine the color SU(3) representation of resonances from new physics signals by analyzing the distribution of soft radiation into a rapidity gap. The results we have found are based on perturbative calculations of factorized partonic cross sections, and apply for ordered scales, $\Lambda_{QCD} < Q_c < \sqrt{\Gamma M} \sim p_T$ with energy flow, Q_c, resonance mass, M, and decay width, Γ. These conditions correspond to a broad width resonance process. The gap fractions for octet and singlet resonances, which we defined in Sec. 5.2.3, show different radiation patterns of energy flow. To obtain an analytical form of soft gluon emission in heavy quark pair production, the massive soft anomalous dimension matrix for rapidity gap events was introduced. The results, in general, describe more radiation for singlet than for octet resonances, which can be explained in terms of color dipole configurations. Especially, for spin-1 resonance production, involving only one partonic sub-process, we obtained a relatively large difference in radiation into the gap region between color singlet and octet resonances. The results at leading order do not require a convolution with PDFs, and are the same at the Tevatron and the LHC in this case. At the end of Sec. 5.6, we discussed the consequences of a narrow width resonance, expecting more radiation for a singlet resonance process compared to our results based on a broad resonance assumption.

In principle, following Ref. [32], given any fixed set of final-state partons, we may calculate the distribution of energy flow into any fixed region of rapidity and azimuthal angle rather than the simple rapidity gap we defined in this

chapter. This may allow not only to illuminate more distinguishable features of color flow, depending on the gauge content of resonances, but also to shed valuable light on the dynamics of QCD radiation itself.

5.8 Appendix

In general, we represent the four momentum of a particle of mass m_Q as

$$p^\mu = (m_T \cosh\eta,\, p_x,\, p_y\,, m_T \sinh\eta)\ , \tag{5.42}$$

where η is rapidity and where m_T is a transverse mass defined by

$$m_T^2 = m_Q^2 + p_x^2 + p_y^2 = m_Q^2 + p_T^2\,. \tag{5.43}$$

In the η-ϕ coordinate system of rapidity and azimuthal angle, four momentum p^μ can be written in terms of quark mass m_Q and ϕ as

$$p^\mu = \left(\sqrt{p_T^2 + m_Q^2}\cosh\eta,\, p_T\cos\phi,\, p_T\sin\phi,\, \sqrt{p_T^2 + m_Q^2}\sinh\eta\right)\ . \tag{5.44}$$

To describe the process in Eq. (5.1) with the gap geometry, shown in Fig. 5.1 at lowest order, we need five external partons of momenta

$$\begin{aligned}
p_1^\mu &= \frac{\sqrt{\hat{s}}}{2}\,(1,\,0,\,0,\,1)\ ,\\
p_2^\mu &= \frac{\sqrt{\hat{s}}}{2}\,(1,\,0,\,0,\,-1)\ ,\\
p_a^\mu &= \left(\sqrt{p_T^2 + m_Q^2}\cosh\left(\frac{\Delta\eta}{2}\right),\, p_T,\, 0,\, \sqrt{p_T^2 + m_Q^2}\sinh\left(\frac{\Delta\eta}{2}\right)\right)\ ,\\
p_b^\mu &= \left(\sqrt{p_T^2 + m_Q^2}\cosh\left(\frac{\Delta\eta}{2}\right),\, -p_T,\, 0,\, -\sqrt{p_T^2 + m_Q^2}\sinh\left(\frac{\Delta\eta}{2}\right)\right)\ ,\\
k^\mu &= k_T\,(\cosh y,\, \cos\phi,\, \sin\phi,\, \sinh y)\ ,
\end{aligned} \tag{5.45}$$

where we are working in the partonic center of mass frame, and where we fix azimuthal angles for a quark pair at $\phi_a = 0$ and $\phi_b = \pi$. Here y is rapidity of soft gluon k.

Chapter 6

The Massive Soft Anomalous Dimension Matrix

6.1 Introduction

The infrared structure of perturbative amplitudes is relevant for a variety of hard-scattering processes, including the production of heavy particles, whether charged under QCD or not, and of high-p_T jets. Infrared enhancements in these amplitudes are typically regularized by continuing to D dimensions, where they appear as poles in $\varepsilon = 2 - D/2$. Infrared poles, of course, do not appear in physical predictions for infrared safe quantities, in which they cancel after an appropriate sum over final states. Nevertheless, the all-order structure of infrared poles is of interest for exact fixed-order calculations [164], for resummations of long-distance enhancements in cross sections [165] and for supersymmetric gauge theories [166].

In this chapter, we study the dependence of infrared enhancements at two loops on the masses of external partons. Our analysis is relevant to dimensionally regularized amplitudes for $2 \to n$ processes (labelled by **f**),

$$\mathbf{f}: \quad f_1(p_1, r_1) + f_2(p_2, r_2) \to f_3(p_3, r_3) + \cdots + f_{n+2}(p_{n+2}, r_{n+2})\,, \tag{6.1}$$

where the r_i represent color indices. At fixed, nonforward angles, amplitudes of this type factorize into functions representing short-distance (hard) dynamics, collinear dynamics of external massless partons, and soft-gluon exchange be-

tween light and heavy partons. We can represent such a factorized amplitude as [31, 104]

$$\left| \mathcal{M}_{\rm f}\left(\beta_i, \frac{Q^2}{\mu^2}, \alpha_s(\mu), \varepsilon\right)\right\rangle \;=\; \prod_i J^{[i]}\left(\alpha_s(\mu),\varepsilon\right) \times \mathbf{S}_{\rm f}\left(\beta_i, \frac{Q^2}{\mu^2}, \alpha_s(\mu), \varepsilon\right) \left| H_{\rm f}\left(\beta_i, \frac{p_j}{\mu}, \frac{Q}{\mu}, \alpha_s(\mu)\right)\right\rangle , \tag{6.2}$$

in the notation of Ref. [30], where the ket $|A(\rho,\varepsilon)\rangle$ is defined by

$$|A(\rho,\varepsilon)\rangle = \sum_{L=1}^{C} A_L(\rho,\varepsilon)\ \left(c_L\right)_{\{r_i\}} , \tag{6.3}$$

with $\{c_L\}$ some basis of color tensors linking the heavy and light parton lines at short distances. The jet functions $J^{[i]}$ for incoming and outgoing lightlike partons may be defined, for example, as the square root of the corresponding elastic form factor [31]. The soft matrix $\mathbf{S}_{\rm f}$, which is the subject of study here, describes the infrared behavior of color exchange between the external partons. It remains after the factorization of collinear enhancements into the jet functions for those external partons that are massless, and in general mixes the color components found at short distance. We do not introduce jet functions for massive partons here. The resummation of collinear logarithms associated with high-p_T massive partons can be treated by factorization as well [167], but this is not a goal of this chapter.

6.2 The massive soft anomalous dimension matrix at two loops

The soft matrix is determined entirely by a matrix of anomalous dimensions [104], through

$$\mathbf{S}_{\rm f}\left(\beta_i, \alpha_s(\mu), \varepsilon\right) = \mathrm{P}\ \exp\left[-\int_0^{\mu} \frac{d\tilde{\mu}}{\tilde{\mu}} \mathbf{\Gamma}_{S_{\rm f}}\left(\beta_i\cdot\beta_j, \bar{\alpha_s}\left(\tilde{\mu},\varepsilon\right)\right)\right] , \tag{6.4}$$

where the velocities β_i are lightlike for light partons, $\beta_l^2 = 0$, and may be scaled to unit length for heavy particles, $\beta_h^2 = 1$. Integrals in the exponent are carried

out in $D > 4$, using the D-dimensional running coupling, $\bar{\alpha}_s(\tilde{\mu}, \varepsilon)$. Equation (6.4), along with corresponding expressions for the jet functions, determines the infrared pole structure to all orders in perturbation theory for processes involving the wide-angle scattering of any number of massless *and* massive partons [31, 104, 140].

The determination of the anomalous dimension matrix for an arbitrary process with massless and massive partons is equivalent to the renormalization of a set of color tensors that link the corresponding product of Wilson lines at a point [140, 168]. Each Wilson line follows the velocity β_i of the corresponding parton, without recoil, from this point to infinity, either from the initial state or into the final state. These composite operators mix under renormalization in general, leading to the matrix structure shown in Eq. (6.4). The one-loop anomalous dimensions for gluons and for both massless and massive quarks have been known for some time [140, 169]. At two loops, the matrices for any $2 \to n$ process with *massless* lines satisfy the relation [28]

$$\mathbf{\Gamma}^{(2)}_{S_{\rm f}}(\beta_i) = \frac{K}{2}\,\mathbf{\Gamma}^{(1)}_{S_{\rm f}}(\beta_i)\,, \tag{6.5}$$

with $\mathbf{\Gamma}^{(i)}_{S_{\rm f}}$ the coefficient of $(\alpha_s/\pi)^i$, and with $K = C_A(67/18 - \zeta(2)) - 10T_F n_F/9$. This is exactly the relation satisfied by the expansion of the cusp anomalous dimension [170], which generates the leading, double poles in the elastic form factor [103, 171, 172].

Examples of the diagrams involved in the calculation of the two-loop anomalous dimension are shown in Fig. 6.1. In momentum space, the propagators and vertices from Wilson lines are given by eikonal expressions [140]. The corresponding two-loop corrections to the anomalous dimensions are found in the usual way [28] from the two-loop UV single poles of these diagrams after one-loop renormalization.

The result (6.5) for massless partons is a consequence of the vanishing of the single poles of those two-loop "3E" diagrams in which color is exchanged coherently between three eikonal lines in the figures. The arguments of Ref. [28] do not, however, generalize directly to massive Wilson lines, with velocity vectors $\beta_i^2 \neq 0$. While an analytic determination of $\Gamma^{(2)}_S$ would, of course, be desirable, numerical determination is also of interest, and is certainly adequate

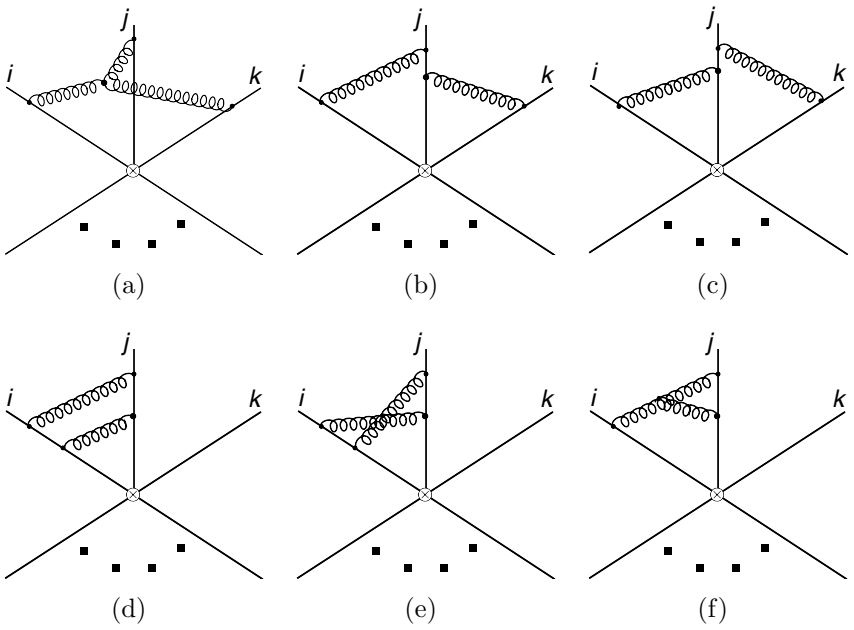

Figure 6.1: Diagrams whose ultraviolet poles determine the soft anomalous dimension at two loops. The crossed vertex represents the point at which the Wilson lines are linked. The straight lines represent eikonal propagators. Referring to the number of Wilson lines linked by gluons, in the text we refer to these as 3E diagrams (a-c) and 2E diagrams (d-f).

to determine how far Eq. (6.5) generalizes to the production of massive particles. We provide the necessary analysis below, and show that when the β_i^2 are nonzero, Eq. (6.5) no longer holds. A generalization of Eq. (6.5), however, given by Eq. (6.31) below, does holds for two-to-two processes for special momentum configurations.

Much of our analysis will be carried out in position, rather than momentum space. In the following, we will take every parton as massive, and use the scale invariance of Wilson lines to set $\beta_i^2 = 1$. Because we are calculating renormalization constants, we can carry out our analysis in Euclidean space. Indeed, a numerical result in Euclidean space is adequate to establish that the matrix does not follow Eq. (6.5) in Minkowski space. Otherwise, analytic continuation through Wick rotation would imply that the same result would hold in Euclidean space as well.

We begin with the diagram, Fig. 6.1a, in which three eikonal lines are coupled by gluons that are linked at a three-gluon coupling [28]. In the configuration space evaluation of this diagram, we must integrate the position of the three-gluon vertex over all space. The three propagators each have one end fixed at this vertex and the other end fixed at a point $\lambda_i \beta_i$ along the ith Wilson line. Each parameter λ_i is integrated from the composite vertex to infinity. This diagram vanishes in Minkowski space for massless Wilson lines [28].

Suppressing color factors, we represent the 3E diagram Fig. 6.1a as

$$F_{3g}^{(2)}(\beta_I) = \int d^D x \prod_{i=1}^{3} \int_0^\infty d\lambda_i V(x, \beta_I) \,. \tag{6.6}$$

Here $\beta_I = \{\beta_1, \beta_2, \beta_3\}$ denotes the set of three massive velocities of the lines to which the gluons attach, while the propagators and numerator factors of the integrand are given by a sum over six terms,

$$V(x, \beta_I) = \sum_{i,j,k=1}^{3} \epsilon_{ijk} v_{ijk}(x, \beta_I) \,. \tag{6.7}$$

Each of these terms involves the derivative of one of the propagators, according

to the usual gauge theory rules for the three-vector coupling,

$$v_{ijk}(x,\beta_I) \;=\; -i(g\mu^\varepsilon)^4 \beta_i\cdot\beta_j\,\Delta(x-\lambda_j\beta_j)\,\Delta(x-\lambda_k\beta_k)\,\beta_k\cdot\partial_x\Delta(x-\lambda_i\beta_i)\,, \tag{6.8}$$

where Δ represents the position-space scalar propagator,

$$\Delta(x-\lambda_i\beta_i) = -\,\frac{\Gamma(1-\varepsilon)}{4\pi^{2-\varepsilon}}\frac{1}{(x-\lambda_i\beta_i)^{2(1-\varepsilon)}}\,. \tag{6.9}$$

We work in Feynman gauge. The contribution of this (scaleless) diagram to the anomalous dimension matrix is found from the residue of its simple ultraviolet pole. We note that all diagrams found from products of Wilson lines are scaleless overall, and are *defined* by their renormalization constants [28].

At fixed x, for massive eikonals the λ integrals in Eq. (6.6) are all finite in four dimensions. After these integrals are carried out, the β_i-dependence enters only through the combination

$$\zeta_i \equiv \frac{\beta_i\cdot x}{\sqrt{x^2}}\,, \tag{6.10}$$

and we can write

$$F_{3g}^{(2)}(\beta_I,\varepsilon) = \mathcal{N}(\varepsilon)\int d^Dx\sum_{i,j,k=1}^{3}\epsilon_{ijk}\gamma_{ijk}(\sqrt{x^2},\zeta_I,\varepsilon)\,, \tag{6.11}$$

where $\mathcal{N}(\varepsilon)$ absorbs overall factors that are finite in the limit $\varepsilon=0$. To simplify our notation, in the following we normalize F_{3g} so that $\mathcal{N}(\varepsilon)=1$. We recall that we have used the scale invariance of eikonal lines to set $\beta_I^2=1$, and that I represents the set i,j,k. Each term γ_{ijk} is now given by

$$\gamma_{ijk}(\sqrt{x^2},\zeta_I,\varepsilon) \;=\; \beta_i\cdot\beta_j\,f(x,\beta_j,\varepsilon)\,f(x,\beta_k,\varepsilon)\beta_k\cdot\partial_x\,f(x,\beta_i,\varepsilon)\,, \tag{6.12}$$

where the functions $f(x,\beta,\varepsilon)$ are simply the integrals of the x-dependent fac-

tors of the propagators,

$$f(x,\beta,\varepsilon) \;=\; \int_0^\infty d\lambda\, \frac{1}{(x^2 - 2\lambda\beta\cdot x + \lambda^2)^{1-\varepsilon}}\,. \tag{6.13}$$

After a change of variables to $\lambda' \equiv \lambda/\sqrt{x^2}$, the dependence on the variables x^2 and ζ_i factorizes,

$$\begin{aligned} f(x,\beta_i,\varepsilon) &= \frac{1}{\left(\sqrt{x^2}\right)^{1-2\varepsilon}} \int_0^\infty d\lambda'\, \frac{1}{(1 - 2\lambda'\zeta_i + \lambda'^2)^{1-\varepsilon}} \\ &\equiv \frac{1}{\left(\sqrt{x^2}\right)^{1-2\varepsilon}}\; g(\zeta_i,\varepsilon)\,. \end{aligned} \tag{6.14}$$

For the full expression, we also need the gradient of this function, which can be written as

$$\begin{aligned} \partial_x^i\, f(x,\beta,\varepsilon) &= \frac{1}{\left(\sqrt{x^2}\right)^{2-2\varepsilon}} \left[(2\varepsilon - 1)\frac{x^i}{\sqrt{x^2}}\, g(\zeta,\varepsilon) \right. \\ &\quad \left. +\; \left(-\,\frac{x^i\zeta}{\sqrt{x^2}} + \beta^i \right)\, \frac{\partial g(\zeta,\varepsilon)}{\partial\zeta} \right]. \end{aligned} \tag{6.15}$$

We note that this derivative is necessary to produce an overall x^{-4} fall-off at infinity and a singularity at $x = 0$, corresponding to logarithmic infrared and ultraviolet behaviors.

We next substitute the expressions for the functions f in (6.14) and their gradients (6.15) into Eq. (6.12) for the terms γ_{ijk}, to find

$$\begin{aligned} \gamma_{ijk}(\sqrt{x^2},\zeta_I,\varepsilon) &= g(\zeta_j,\varepsilon)g(\zeta_k,\varepsilon)\, \frac{\beta_i\cdot\beta_j}{\left(\sqrt{x^2}\right)^{4-6\varepsilon}} \\ &\times \left[(2\varepsilon - 1)\zeta_k g(\zeta_i,\varepsilon) + (-\zeta_k\zeta_i + \beta_i\cdot\beta_k)\, \frac{\partial g(\zeta_i,\varepsilon)}{\partial\zeta_i} \right]. \end{aligned} \tag{6.16}$$

In this expression, the first term in the square brackets is symmetric in the pair (i,j) and the third is symmetric in the pair (j,k). The full nonvanishing

contribution to Eq. (6.11) is thus simply

$$F_{3g}^{(2)}(\beta_I,\varepsilon) \;=\; -\int d^Dx \sum_{i,j,k=1}^{3} \epsilon_{ijk}\, \frac{\zeta_k\zeta_i\,\beta_i\cdot\beta_j}{\left(\sqrt{x^2}\right)^{4-6\varepsilon}} g(\zeta_j,\varepsilon)g(\zeta_k,\varepsilon)\; \frac{\partial g(\zeta_i,\varepsilon)}{\partial\zeta_i}\,. \tag{6.17}$$

Using the freedom to reintroduce dependence on the $\sqrt{\beta_i^2}$ by demanding scale invariance, we can use this result in both Minkowski and Euclidean space to identify and isolate the ultraviolet pole. It is now straightforward to show two important results that follow from the antisymmetries built into Eq. (6.17).

First, working in Minkowski space, we can readily confirm the vanishing of F_{3g} for arbitrary massless β_i. In this case, the function remains scale-invariant in the β_i, although of course we cannot rescale by $\beta_i^2 = 0$. Nevertheless, the explicit form of $g(\zeta,\varepsilon)$ is

$$g(\zeta,\varepsilon) = \frac{1}{2\varepsilon}\frac{1}{\zeta} \qquad (\beta^2=0)\,, \tag{6.18}$$

which, using $\zeta(dg/d\zeta) = -g$, immediately gives a vanishing integrand in Eq. (6.17) by antisymmetry. It is interesting to note that, unlike the discussion in momentum space in Ref. [28], this proof of the vanishing of the three-gluon diagram, $F_{3g}^{(2)}$, Fig. 6.1a, does not require a change of variables.

In fact, the vanishing of Fig. 6.1a extends to the case where only two of the three lines are massless [173]. Taking for definiteness $\beta_1^2 = \beta_2^2 = 0$ with $\beta_3^2 \neq 0$, and using Eq. (6.18) in Eq. (6.17), we find

$$\begin{aligned} F_{3g}^{(2)}(\beta_I,\varepsilon) \;=\; & -\int d^Dx\, \frac{1}{\left(\sqrt{x^2}\right)^{4-6\varepsilon}} \\ & \times \left(g(\zeta_3,\varepsilon) + \zeta_3\frac{\partial g(\zeta_3,\varepsilon)}{\partial\zeta_3}\right)\left(\frac{\beta_1\cdot\beta_3}{\zeta_1} - \frac{\beta_2\cdot\beta_3}{\zeta_2}\right)\,. \end{aligned} \tag{6.19}$$

In this case, we follow [28] and make a change of variables, using the light-like directions $\beta_{1,2}$ to define light-cone coordinates. To be specific, if we choose $\chi_1 = \zeta_1/\beta_1\cdot\beta_3$ and $\chi_2 = \zeta_2/\beta_2\cdot\beta_3$, we derive an integrand that is manifestly antisymmetric in χ_1 and χ_2. We note that the momentum space method of [28] also applies directly to the case when two of the three Wilson lines are

massless, although this was not pointed out explicitly there. In both cases, the relevant change of variables exchanges two lightlike directions. This approach does not show that diagrams with a single massless line vanish identically, and indeed this seems unlikely, given that in this case there is only a single lightlike direction.

Our second main result is that for both massive and massless Wilson lines the function $\Gamma^{(2)}_{3g}(\beta_i\cdot\beta_j)$ vanishes when any pair of the invariants are equal, say, $\beta_1\cdot\beta_2 = \beta_1\cdot\beta_3$. We can show this by changing variables in Euclidean space from x_i to $r = \sqrt{x^2}$ and the $\zeta_i = \beta_i\cdot x/\sqrt{x^2}$. A straightforward calculation gives a form in which the overall scalelessness of the diagram is manifest in the radial integral,

$$\begin{aligned} F^{(2)}_{3g}(\beta_I,\varepsilon) &= -\int \frac{dr}{r^{1-4\varepsilon}} \int \frac{d\zeta_1 d\zeta_2 d\zeta_3}{\sqrt{K(\zeta_I)}} \\ &\quad\times \sum_{i,j,k=1}^{3} \epsilon_{ijk}\,\zeta_k\zeta_i\,\beta_i\cdot\beta_j\; g(\zeta_j,\varepsilon)g(\zeta_k,\varepsilon)\;\frac{\partial g(\zeta_i,\varepsilon)}{\partial\zeta_i}\,. \end{aligned} \tag{6.20}$$

Defining $w_j \equiv \beta_1\cdot\beta_j$, $\xi_j \equiv \zeta_j - w_j\zeta_1$, and $z_3 \equiv [\beta_2\cdot\beta_3 - w_2w_3]/\sqrt{1-w_2^2}$, the explicit form of $K(\zeta_I)$ for arbitrary w_2 and w_3 is

$$\begin{aligned} K(\zeta_I) &= -(1-w_2^2)\xi_3^2 - (1-w_3^2)\xi_2^2 + 2\xi_2\xi_3 z_3\sqrt{1-w_2^2} \\ &\quad +(1-\zeta_1^2)(1-w_2^2)(1-z_3^2-w_3^2)\,. \end{aligned} \tag{6.21}$$

The function $K(\zeta_I)$ is symmetric under the interchange of ζ_2 and ζ_3 when $w_2 = w_3$. We easily check that when $w_2 = w_3$ the remaining integrand in Eq. (6.20) is antisymmetric under the exchange of ζ_2 and ζ_3. The variables ζ_2 and ζ_3 are exchanged by a reflection in the two-sphere defined by any fixed value of ζ_1 about the axis specified by the projection of $\beta_2+\beta_3$ into this two-sphere. The integration region of ζ_2 and ζ_3 is therefore also symmetric. We conclude that the integral over ζ_2 and ζ_3 in Eq. (6.20) vanishes when $\beta_1\cdot\beta_2 = \beta_1\cdot\beta_3$. This relation holds as well in Minkowski space, which can be reached by analytic continuation at fixed ratios of the inner products $\beta_1\cdot\beta_2/\beta_1\cdot\beta_3$.

We do not have here an analytic form for the residue of the UV pole of $F^{(2)}_{3g}$ for generic values of the invariants $\beta_i\cdot\beta_j$. A numerical analysis of Eq. (6.17), however, is particularly straightforward in Euclidean space. For this purpose,

it is convenient to use D-dimensional polar coordinates, r, Ω_{D-1}. The single overall ultraviolet pole in the scaleless integral (6.17) appears at $r = 0$, and the remaining three angular integrals at $\varepsilon = 0$ determine the residue of the pole in $\overline{\rm MS}$ renormalization. These can be carried out readily, using the elementary form of the function $g(\zeta, 0)$ in Eq. (6.14),

$$g(\zeta, 0) = \frac{\pi - \arccos\zeta}{\sqrt{1-\zeta^2}}\,. \tag{6.22}$$

In Fig. 6.2, we show a plot of the residue of the UV pole of $F_{3g}^{(2)}$ for $\beta_1 \cdot \beta_3 = 0.5$ in the $\beta_1 \cdot \beta_2 / \beta_2 \cdot \beta_3$-plane, suppressing the surface where the integral is negative for clarity. Notice the lines of zeros at $\beta_1 \cdot \beta_2 = \beta_2 \cdot \beta_3$ and at $\beta_1 \cdot \beta_2 = 0.5$ and $\beta_2 \cdot \beta_3 = 0.5$. The peak towards $\beta_1 \cdot \beta_2 \to 1$ reflects an additional singularity in the integrand when two velocities are parallel.

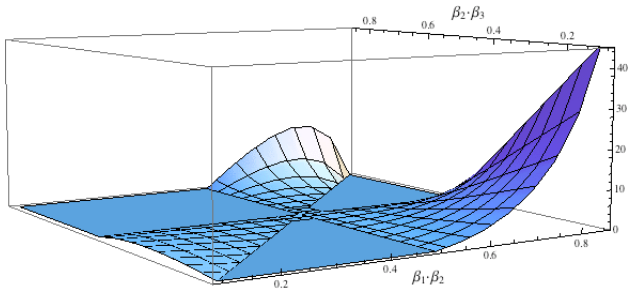

Figure 6.2: Plot of the integral in (6.17) for $\beta_1 \cdot \beta_3 = 0.5$.

We now turn to the remaining 3E "double-exchange" diagrams, Fig. 1b,c. These diagrams are given by four λ integrations, two of which are along the β_j line. For example, Fig. 1b may be written in the notation introduced above as

$$\begin{aligned} M_b \;\; = \;\; & C_{1b}\, \overline{\mathcal{N}}(\varepsilon)\, (\beta_i \cdot \beta_j)\, (\beta_j \cdot \beta_k) \int_0^\infty d\lambda_{j,a} \int_0^{\lambda_{j,a}} d\lambda_{j,b} \\ & \times f(\lambda_{j,a}\beta_j, \beta_i, \varepsilon)\, f(\lambda_{j,b}\beta_j, \beta_k, \varepsilon)\,, \end{aligned} \tag{6.23}$$

where the functions f are defined as in Eq. (6.14) with $x = \lambda_{j,c}\beta_j$ and with $c = a, b$. $\overline{\mathcal{N}}(\varepsilon)$ absorbs overall factors that are finite in the limit $\varepsilon = 0$. In the following we set $\overline{\mathcal{N}}(\varepsilon) = 1$. We have kept the overall color factor, represented by C_{1b}. The variables $\zeta_i = \beta_i \cdot x/\sqrt{x^2}$, are independent of the scale of x in Eq. (6.23), so that all dependence on the $\lambda_{j,c}$ variable is in the overall factor of $x^2 = \lambda_{j,c}^2$, giving

$$M_b \;=\; C_{1b}\,(\beta_i\cdot\beta_j)\,(\beta_j\cdot\beta_k)\int_0^\infty d\lambda_{j,a}\int_0^{\lambda_{j,a}} d\lambda_{j,b}\,\frac{g(\beta_i\cdot\beta_j,\varepsilon)\,g(\beta_k\cdot\beta_j,\varepsilon)}{(\lambda_{j,a}\lambda_{j,b})^{1-2\varepsilon}}\,. \tag{6.24}$$

The exchange diagrams contribute to two color structures, symmetric and antisymmetric with respect to the generators T_a and T_b on line β_j that are linked by gluon exchange to the lines β_i and β_k, respectively. Combining Fig. 6.1b and c, we thus write

$$M_b(\beta_I,\varepsilon) + M_c(\beta_I,\varepsilon) = M_{b+c}^{(A)}(\beta_I,\varepsilon) \;+\; M_{b+c}^{(S)}(\beta_I,\varepsilon)\,. \tag{6.25}$$

The first, antisymmetric, combination has the same color factor as the three gluon diagram, Fig. 6.1a, discussed above. It is given by

$$\begin{aligned} M_{b+c}^{(A)}(\beta_I,\varepsilon) \;=\; & \frac{1}{2}\,[C_{1b} \;-\; C_{1c}]\;(\beta_i\cdot\beta_j)\,(\beta_j\cdot\beta_k) \\ & \times\left(\int_0^\infty d\lambda_{j,a}\int_0^{\lambda_{j,a}} d\lambda_{j,b} - \int_0^\infty d\lambda_{j,b}\int_0^{\lambda_{j,b}} d\lambda_{j,a}\right) \\ & \times\frac{g(\beta_i\cdot\beta_j,\varepsilon)\,g(\beta_k\cdot\beta_j,\varepsilon)}{(\lambda_{j,a}\lambda_{j,b})^{1-2\varepsilon}}\,, \end{aligned} \tag{6.26}$$

where the difference in color factors in square brackets produces a commutator for the color matrices on the β_j line. Clearly, the integrals in parenthesis are identical and cancel. This result applies to arbitrary masses for the Wilson lines. As in the massless case, only the symmetric contribution of the double exchange diagrams survives and contributes to the soft matrix. As described in Ref. [28], however, the symmetric contribution to the soft matrix at two loops is already generated by the exponential of the one-loop anomalous dimension in Eq. (6.4).

The reasoning above has a significant phenomenological application to $2 \to 2$ production processes. Using Wick rotation, the vanishing of 3E diagrams after one-loop renormalization when pairs of invariants are equal applies to $2 \to 2$ processes involving the production of pairs of heavy quarks from light quarks or gluons. In particular, we consider Wilson line velocities corresponding to momentum configurations with $t = (p_1 - p_3)^2 = (p_1 - p_4)^2 = u$ in Eq. (6.1) with $n = 2$ [174]. Note that because it is trivial to reintroduce β_i^2-dependence, the result applies as well to the limit where one or more line becomes massless.

Of special interest are the anomalous dimension matrices that enter pair production: the 2×2 matrix for $q\bar{q} \to Q\bar{Q}$ and the 3×3 matrix for $gg \to Q\bar{Q}$. At one-loop, these matrices are diagonal in their s-channel singlet-octet bases at $u = t$ [140]. Specifically, the off-diagonal elements of these $\Gamma_S^{(1)}$ are all proportional to $\ln(u/t)$. One- and two-loop diagrams contributing to these anomalous dimension matrices are illustrated by Fig. 6.3, where the single eikonal lines represent incoming light partons (quark pairs or gluons) and the double lines heavy quark pairs. At $u = t$, the off-diagonal zeros in $\Gamma_S^{(1)}$ directly reflect cancellation between pairs of diagrams such as those in Fig. 6.3a and b.

To illustrate the pattern of cancellation, we continue the notation above and write the amplitude, M_D corresponding to eikonal diagram D as the product of a color factor and a velocity-dependent factor,

$$M_D^{(n)} = C_D \, F_D^{(n)}(\beta_I) \, . \tag{6.27}$$

In these terms, the vanishing of matrix elements that describe the mixing of color singlet-octet tensors in $\Gamma_S^{(1)}$ follows from identities relating the two diagrams,

$$F_{2a}^{(1)}(\beta_I) = F_{2b}^{(1)}(\beta_I) \, , \tag{6.28}$$

$$C_{2a} = -C_{2b} \, , \tag{6.29}$$

which are easily verified at one-loop for $u = t$. We have shown above that at two loops with $u = t$, 3E diagrams like Fig. 6.3c vanish independently of their color structure, leaving only 2E diagrams and the color-symmetric parts of 3E exchange diagrams at two loops. This suggests that at two loops the same

pattern of cancellation may persist for $\Gamma_S^{(2)}$. This is indeed the case, as we now explain.

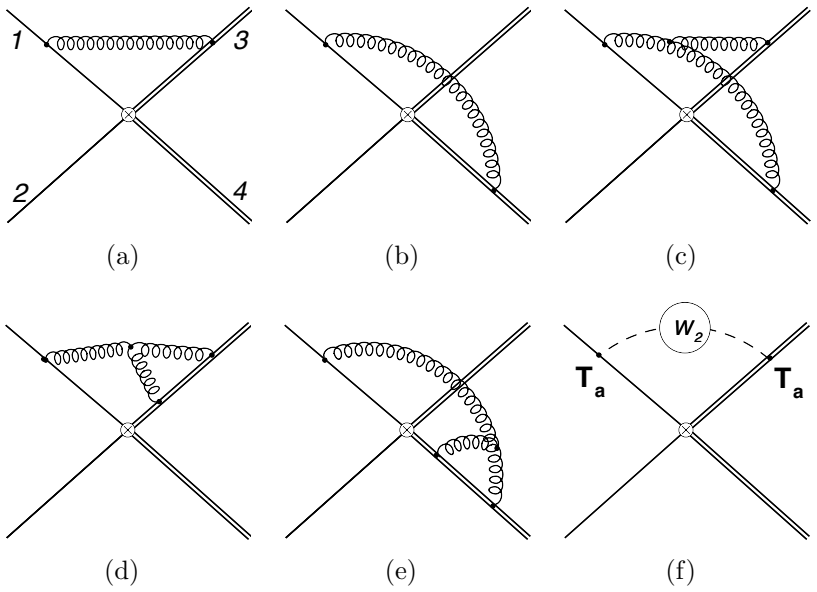

Figure 6.3: One-loop 2E diagrams (a,b) that cancel at $u = t$. (c) representative 3E diagram for this process. Diagrams (d,e) are two-loop diagrams that cancel. Diagram f represents the color structure of the webs.

At one-loop, the expansion of Eq. (6.4) in terms of one-loop anomalous dimensions can be thought of as the sum of contributions from each gluon-exchange diagram. Expanding the one-loop form of Eq. (6.4) to order α_s^2, we generate all color-symmetric contributions of two-loop ladder diagrams, corresponding for example to the color-symmetric contributions of Fig. 6.1d and e above. The sum of all 2E diagrams is thus easily rewritten in terms of the expansion of Eq. (6.4) in terms of $\Gamma_S^{(1)}$, plus two-loop contributions that involve commutators of generators on one or more of the Wilson lines.

Examples of diagrams with antisymmetric color structure, which do not correspond to the expansion of the one-loop anomalous dimensions, are Figs. 6.1f and 6.3d and e, and the color-antisymmetric part of Fig. 6.1e. These diagrams contribute only their antisymmetric combinations of color generators to $\Gamma_S^{(2)}$, and are thus proportional to C_A times a one-loop color factor. Figure 6.3f is a schematic representation of the color structure of such diagrams and of their contributions to the two-loop anomalous dimension matrices.

We note that exactly as for the massless case in Ref. [28], all 2E diagrams

are generated from an exponential of "webs" [175]. Webs are themselves 2E diagrams that are two-particle irreducible under cuts of the Wilson lines, starting with single-gluon exchange. The contributions of two-loop webs are precisely the antisymmetric color structures that we have just identified.

As we have observed, Eq. (6.29) holds for the color factors of Fig. 6.3a and b. The same relation then holds for the web contributions of Fig 6.3d and e, because they are proportional to the same color structure as the one-loop diagrams, as illustrated in Fig. 6.3f. Therefore, whenever the identity for velocity factors, Eq. (6.28), holds at two loops, this pair of two-loop diagrams cancels. The 2E diagrams of Fig. 6.3a and b, however, can depend only on the invariants formed from the two eikonal velocities in question, so that at $u = t$,

$$F_{2a}^{(2)}(\beta_I) = F_{2b}^{(2)}(\beta_I) \quad (u = t) \ . \tag{6.30}$$

This relation will hold as well for diagrams associated with crossed ladders, as in Fig. 6.1e, and other diagrams with color-antisymmetric contributions, including those with self-energies of the exchanged gluon and vertex corrections on the massive eikonal. As a result, cancellations between pairs of 2E diagrams that occur at one-loop recur at two. For $2 \to 2$ kinematic configurations with $u = t$, then, we have in place of Eq. (6.5) the relation

$$\mathbf{\Gamma}_{S_{\rm f}}^{(2)}(\beta_I) = D(\beta_I)\, \mathbf{\Gamma}_{S_{\rm f}}^{(1)}(\beta_I) \quad (u = t)\,, \tag{6.31}$$

where $D(\beta_I)$ is a matrix that is diagonal in the s-channel singlet-octet basis. For massless two-loop cases, the matrix $D(\beta_I)$ is proportional to the identity, and we recover a special case of Eq. (6.5). More generally, however, the integrals of the 2E webs depend on masses. We will give explicit results elsewhere. In any case, the relation (6.31) applies for scattering at ninety degrees in the center of mass, including the limiting case of production at rest ($\hat{s} = 4m_Q^2$), of particular relevance to threshold resummation for the total cross section for heavy quark production [176]. A subset of these diagrams have been analyzed very recently in [141].

For massless particles, as noted in [28] it is certainly natural to generalize the result Eq. (6.5) for lightlike partons to all orders. This possibility has been explored recently in Refs. [177]. The result that we have found here, that

Eq. (6.5) does not apply to arbitrary massive kinematics, suggests that the zero-mass case is indeed special. We believe this should encourage the search for a symmetry or principle underlying the relation, Eq. (6.5).

6.3 Conclusions

We have shown that for products of massive Wilson lines, one- and two-loop soft anomalous dimensions are generally not proportional. We have noted, however, that diagrams that link two massless with one massive line through the three-gluon coupling vanish by a variant of the reasoning for three massless lines. We have also shown that diagrams that link a single massless line with two massive lines cancel for the case of two-to-two production processes at threshold, and when $u = t$, that is, for production at ninety degrees in the center of mass system. For these momentum configurations, the two-loop anomalous dimension matrix is diagonal in the same color basis as the one-loop, although they are not related by a simple proportionality as in the massless case. The color-antisymmetric parts of exchange diagrams linking three eikonal lines cancel independently of masses. We carried out a numerical evaluation of the three-gluon diagram in Euclidean space, but the qualitative conclusions of this chapter extend to Minkowski space. Whatever the field-theoretic origin of the results described above for massive and massless partons, the renormalization of the composite operators that link Wilson lines will be relevant to the analysis of light-parton jets, heavy quarks and potential new, strongly interacting particles at the Tevatron and the LHC.

Bibliography

[1] M. Gell-Mann, Phys. Lett. **8**, 214 (1964).

[2] R. P. Feynman, Phys. Rev. Lett. **23**, 1415 (1969).

[3] C. G. . Callan and D. J. Gross, Phys. Rev. Lett. **22**, 156 (1969).

[4] J. D. Bjorken and E. A. Paschos, Phys. Rev. **185**, 1975 (1969).

[5] H. D. Politzer, Phys. Rev. Lett. **30**, 1346 (1973).

[6] D. J. Gross and F. Wilczek, Phys. Rev. Lett. **30**, 1343 (1973).

[7] O. W. Greenberg, Phys. Rev. Lett. **13**, 598 (1964).

[8] M. Y. Han and Y. Nambu, Phys. Rev. **139**, B1006 (1965).

[9] H. Fritzsch, M. Gell-Mann and H. Leutwyler, Phys. Lett. B **47**, 365 (1973); S. Weinberg, Phys. Rev. Lett. **31**, 494 (1973).

[10] G. 't Hooft, Nucl. Phys. B **33**, 173 (1971); G. 't Hooft, Nucl. Phys. B **35**, 167 (1971); G. 't Hooft and M. J. G. Veltman, Nucl. Phys. B **44**, 189 (1972).

[11] M. A. Nowak, M. Rho and I. Zahed, *Singapore, Singapore: World Scientific (1996) 528 p.*

[12] M. Creutz, *Cambridge, Uk: Univ. Pr. (1983) 169 P. (Cambridge Monographs On Mathematical Physics).*

[13] T. Schafer and E. V. Shuryak, Rev. Mod. Phys. **70**, 323 (1998) [arXiv:hep-ph/9610451].

[14] F. Bloch and A. Nordsieck, Phys. Rev. **52**, 54 (1937).

[15] T. Kinoshita, J. Math. Phys. **3**, 650 (1962); T. D. Lee and M. Nauenberg, Phys. Rev. **133**, B1549 (1964).

[16] G. Sterman and S. Weinberg, Phys. Rev. Lett. **39**, 1436 (1977).

[17] G. Sterman, Phys. Rev. D **17**, 2773 (1978).

[18] G. Sterman, Phys. Rev. D **17**, 2789 (1978).

[19] J. C. Collins, D. E. Soper and G. Sterman, Adv. Ser. Direct. High Energy Phys. **5**, 1 (1988) [arXiv:hep-ph/0409313]; G. Sterman, arXiv:hep-ph/0412013.

[20] J. F. Owens and W. K. Tung, Ann. Rev. Nucl. Part. Sci. **42**, 291 (1992).

[21] V. N. Gribov and L. N. Lipatov, Yad. Fiz. **15**, 781 (1972) [Sov. J. Nucl. Phys. **15**, 438 (1972)].

[22] L. N. Lipatov, Sov. J. Nucl. Phys. **20**, 94 (1975) [Yad. Fiz. **20**, 181 (1974)].

[23] G. Altarelli and G. Parisi, Nucl. Phys. B **126**, 298 (1977).

[24] Y. L. Dokshitzer, Sov. Phys. JETP **46**, 641 (1977) [Zh. Eksp. Teor. Fiz. **73**, 1216 (1977)].

[25] L. G. Almeida, S. J. Lee, G. Perez, G. Sterman, I. Sung and J. Virzi, Phys. Rev. D **79**, 074017 (2009) [arXiv:0807.0234 [hep-ph]].

[26] L. G. Almeida, S. J. Lee, G. Perez, I. Sung and J. Virzi, Phys. Rev. D **79**, 074012 (2009) [arXiv:0810.0934 [hep-ph]].

[27] I. Sung, Phys. Rev. D **80**, 094020 (2009) [arXiv:0908.3688 [hep-ph]].

[28] S. Mert Aybat, L. J. Dixon and G. Sterman, Phys. Rev. Lett. **97**, 072001 (2006) [arXiv:hep-ph/0606254]; S. Mert Aybat, L. J. Dixon and G. Sterman, Phys. Rev. D **74**, 074004 (2006) [arXiv:hep-ph/0607309].

[29] A. Mitov, G. Sterman and I. Sung, Phys. Rev. D **79**, 094015 (2009) [arXiv:0903.3241 [hep-ph]].

[30] S. Catani and M. H. Seymour, Phys. Lett. B **378**, 287 (1996) [hep-ph/9602277]; Nucl. Phys. B **485**, 291 (1997) [Err.-ibid. B **510**, 503 (1997)] [hep-ph/9605323].

[31] G. Sterman and M. E. Tejeda-Yeomans, Phys. Lett. **B552** (2003) 48 [hep-ph/0210130].

[32] C. F. Berger, T. Kucs and G. Sterman, Phys. Rev. D **65**, 094031 (2002) [arXiv:hep-ph/0110004].

[33] H. Contopanagos, E. Laenen and G. Sterman, Nucl. Phys. B **484**, 303 (1997) [arXiv:hep-ph/9604313].

[34] G. Sterman, *Cambridge, UK: Univ. Pr. (1993) 572 p*

[35] N. Kidonakis, G. Oderda and G. Sterman, arXiv:hep-ph/9805279; N. Kidonakis, G. Oderda and G. Sterman, Nucl. Phys. B **531**, 365 (1998) [arXiv:hep-ph/9803241].

[36] C. F. Berger, T. Kucs and G. Sterman, Phys. Rev. D **68**, 014012 (2003) [arXiv:hep-ph/0303051].

[37] T. Sjostrand, S. Mrenna and P. Z. Skands, Comput. Phys. Commun. **178**, 852 (2008) [arXiv:0710.3820 [hep-ph]].

[38] For recent studies see *e.g*: K. Agashe *et al.*, Phys. Rev. D **77**, 015003 (2008) [arXiv:hep-ph/0612015]; B. Lillie, L. Randall and L. T. Wang, JHEP **0709**, 074 (2007) [arXiv:hep-ph/0701166].

[39] See *e.g*: K. Agashe *et al.*, Phys. Rev. D **76**, 115015 (2007) [arXiv:0709.0007 [hep-ph]]; K. Agashe, H. Davoudiasl, G. Perez and A. Soni, Phys. Rev. D **76**, 036006 (2007) [arXiv:hep-ph/0701186]; J. Hirn, A. Martin and V. Sanz, JHEP **0805**, 084 (2008) [arXiv:0712.3783 [hep-ph]].

[40] D. Benchekroun, C. Driouichi, A. Hoummada, SN-ATLAS-2001-001, ATL-COM-PHYS-2000-020, EPJ Direct 3, 1 (2001); J. Conway, *et al.*, LPC Workshop on Early Physics at CMS, UC Davis (2007); G. Brooijmans *et al.*, arXiv:0802.3715 [hep-ph]; M. Vos, talk given in the *ATLAS Flavour Tagging Meeting*, CERN (2008).

[41] G. Brooijmans, ATLAS note, ATL-PHYS-CONF-2008-008.

[42] D. Benchekroun, C. Driouichi, A. Hoummada, SN-ATLAS-2001-001, ATL-COM-PHYS-2000-020, EPJ Direct 3, 1 (2001); J. M. Butterworth, B. E. Cox and J. R. Forshaw, Phys. Rev. D **65**, 096014 (2002) [arXiv:hep-ph/0201098]; J. M. Butterworth, A. R. Davison, M. Rubin and G. P. Salam, arXiv:0809.2530 [hep-ph].

[43] M. H. Seymour, Nucl. Phys. B **513**, 269 (1998) [arXiv:hep-ph/9707338]; S. D. Ellis, J. Huston, K. Hatakeyama, P. Loch and M. Tonnesmann, Prog. Part. Nucl. Phys. **60**, 484 (2008) [arXiv:0712.2447 [hep-ph]].

[44] S. Catani, Y. L. Dokshitzer, M. Olsson, G. Turnock and B. R. Webber, Phys. Lett. B **269**, 432 (1991); S. Catani, Y. L. Dokshitzer, M. H. Seymour and B. R. Webber, Nucl. Phys. B **406**, 187 (1993); S. D. Ellis and D. E. Soper, Phys. Rev. D **48**, 3160 (1993) [arXiv:hep-ph/9305266]; Y. L. Dokshitzer, G. D. Leder, S. Moretti and B. R. Webber, JHEP **9708**, 001 (1997) [arXiv:hep-ph/9707323].

[45] G. P. Salam and G. Soyez, JHEP **0705**, 086 (2007) [arXiv:0704.0292 [hep-ph]].

[46] M. Cacciari, G. P. Salam and G. Soyez, JHEP **0804**, 063 (2008) [arXiv:0802.1189 [hep-ph]].

[47] G. Sterman, Phys. Rev. D **19**, 3135 (1979).

[48] N. Kidonakis, G. Oderda and G. Sterman, Nucl. Phys. B **525**, 299 (1998) [arXiv:hep-ph/9801268]; D. de Florian and W. Vogelsang, Phys. Rev. D **76**, 074031 (2007) [arXiv:0704.1677 [hep-ph]].

[49] M. Dasgupta and G. P. Salam, J. Phys. G **30**, R143 (2004) [arXiv:hep-ph/0312283]; C. F. Berger, Mod. Phys. Lett. A **20**, 1187 (2005) [arXiv:hep-ph/0505037]; M. Dasgupta, L. Magnea and G. P. Salam, JHEP **0802**, 055 (2008) [arXiv:0712.3014 [hep-ph]].

[50] D. E. Kaplan, K. Rehermann, M. D. Schwartz and B. Tweedie, Phys. Rev. Lett. **101**, 142001 (2008) [arXiv:0806.0848 [hep-ph]].

[51] J. Thaler and L. T. Wang, JHEP **0807**, 092 (2008) [arXiv:0806.0023 [hep-ph]].

[52] J. M. Butterworth, A. R. Davison, M. Rubin and G. P. Salam, Phys. Rev. Lett. **100**, 242001 (2008) [arXiv:0802.2470 [hep-ph]].

[53] G. Parisi, Phys. Lett. B **74**, 65 (1978).

[54] J. F. Donoghue, F. E. Low and S. Y. Pi, Phys. Rev. D **20**, 2759 (1979).

[55] R. K. Ellis, D. A. Ross and A. E. Terrano, Nucl. Phys. B **178**, 421 (1981).

[56] A. Banfi, Y. L. Dokshitzer, G. Marchesini and G. Zanderighi, JHEP **0105**, 040 (2001) [arXiv:hep-ph/0104162].

[57] F. Maltoni and T. Stelzer, JHEP **0302**, 027 (2003) [arXiv:hep-ph/0208156]; T. Stelzer and W. F. Long, Comput. Phys. Commun. **81**, 357 (1994) [arXiv:hep-ph/9401258], JHEP **0709**, 028 (2007) [arXiv:0706.2334 [hep-ph]].

[58] T. Gleisberg et al., JHEP **0402** (2004) 056 [arXiv:hep-ph/0311263].

[59] C. F. Berger and L. Magnea, Phys. Rev. D **70**, 094010 (2004) [arXiv:hep-ph/0407024].

[60] ATLAS Detector and physics performance TDR, CERN-LHCC-99-14; CMS Physics and performance TDR, Volume II: CERN-LHCC-2006-021

[61] K. Agashe, A. Belyaev, T. Krupovnickas, G. Perez and J. Virzi, Phys. Rev. D **77**, 015003 (2008) [arXiv:hep-ph/0612015].

[62] A. L. Fitzpatrick, J. Kaplan, L. Randall and L. T. Wang, JHEP **0709**, 013 (2007) [arXiv:hep-ph/0701150].

[63] U. Baur and L. H. Orr, Phys. Rev. D **76**, 094012 (2007) [arXiv:0707.2066 [hep-ph]].

[64] J. Conway, *et al.*, LPC Workshop on Early Physics at CMS, UC Davis (2007); G. Brooijmans *et al.*, arXiv:0802.3715 [hep-ph]; M. Vos, talk given in the *ATLAS Flavour Tagging Meeting*, CERN (2008).

[65] See, for example, L. March, E. Ros and B. Salvachúa, ATL-PHYS-PUB-2006-002, ATL-COM-PHYS-2005-032; L. March, E. Ros and S.G.d.l. Hoz, ATL-COM-PHYS-2006-031, ATL-PHYS-CONF-2006-007; L. March, E. Ros, B. Salvacha, ATL-Phys-PUB-2006-002; M. Vos, ATL-PHYS-PUB-2008-000, ATL-PHYS-CONF-2008-016;

[66] U. Baur and L. H. Orr, Phys. Rev. D **77**, 114001 (2008) [arXiv:0803.1160 [hep-ph]].

[67] Y. Bai and Z. Han, arXiv:0809.4487 [hep-ph].

[68] S. Fleming, A. H. Hoang, S. Mantry and I. W. Stewart, arXiv:0711.2079 [hep-ph]; S. Fleming, A. H. Hoang, S. Mantry and I. W. Stewart, Phys. Rev. D **77**, 074010 (2008) [arXiv:hep-ph/0703207]; A. H. Hoang and I. W. Stewart, arXiv:0808.0222 [hep-ph]. A. Jain, I. Scimemi and I. W. Stewart, Phys. Rev. D **77**, 094008 (2008) [arXiv:0801.0743 [hep-ph]].

[69] W. Skiba and D. Tucker-Smith, Phys. Rev. D **75**, 115010 (2007) [arXiv:hep-ph/0701247].

[70] B. Holdom, JHEP **0708**, 069 (2007) [arXiv:0705.1736 [hep-ph]].

[71] K. Agashe *et al.*, Phys. Rev. D **76**, 115015 (2007) [arXiv:0709.0007 [hep-ph]].

[72] F. Maltoni and T. Stelzer, JHEP **0302**, 027 (2003) [arXiv:hep-ph/0208156].

[73] T. Stelzer and W. F. Long, Comput. Phys. Commun. **81**, 357 (1994) [arXiv:hep-ph/9401258].

[74] J. Alwall *et al.*, JHEP **0709**, 028 (2007) [arXiv:0706.2334 [hep-ph]].

[75] T. Gleisberg et al., JHEP **0402** (2004) 056 [arXiv:hep-ph/0311263].

[76] J. Virzi, "ATLAS Transfer Function, https://twiki.cern.ch/twiki/bin/view/Atlas/TransferFunction."

[77] R. Frederix and F. Maltoni, arXiv:0712.2355 [hep-ph].

[78] V. Barger, T. Han and D. G. E. Walker, Phys. Rev. Lett. **100**, 031801 (2008) [arXiv:hep-ph/0612016].

[79] T. Han, R. Mahbubani, D. G. E. Walker and L. T. E. Wang, arXiv:0803.3820 [hep-ph].

[80] K. Agashe, H. Davoudiasl, G. Perez and A. Soni, Phys. Rev. D **76**, 036006 (2007) [arXiv:hep-ph/0701186]; B. Lillie, L. Randall and L. T. Wang, JHEP **0709**, 074 (2007) [arXiv:hep-ph/0701166]; B. Lillie, J. Shu and T. M. P. Tait, Phys. Rev. D **76**, 115016 (2007) [arXiv:0706.3960 [hep-ph]]; H. Davoudiasl, G. Perez and A. Soni, Phys. Lett. B **665**, 67 (2008) [arXiv:0802.0203 [hep-ph]].

[81] For a recent review see: T. Han, arXiv:0804.3178 [hep-ph].

[82] S. D. Ellis, Z. Kunszt and D. E. Soper, Phys. Rev. Lett. **69**, 3615 (1992) [arXiv:hep-ph/9208249].

[83] F. Hubaut, E. Monnier, P. Pralavorio, K. Smolek and V. Simak, Eur. Phys. J. C **44S2**, 13 (2005) [arXiv:hep-ex/0508061].

[84] W. Bernreuther, J. P. Ma and T. Schroder, Phys. Lett. B **297**, 318 (1992); S. Choi, FERMILAB-THESIS-1999-07; K. A. Johns [D0 Collaboration], Int. J. Mod. Phys. A **16S1A** (2001) 366; W. Bernreuther, A. Brandenburg, Z. G. Si and P. Uwer, Phys. Lett. B **509**, 53 (2001) [arXiv:hep-ph/0104096]; B. Abbott *et al.* [D0 Collaboration], Phys. Rev. Lett. **85**, 256 (2000) [arXiv:hep-ex/0002058]; T. Torma, JHEP **0111**, 055 (2001) [arXiv:hep-ph/9912281]; V. D. Barger, J. Ohnemus and R. J. N. Phillips, Int. J. Mod. Phys. A **4**, 617 (1989); G. L. Kane, G. A. Ladinsky and C. P. Yuan, Phys. Rev. D **45**, 124 (1992); G. Mahlon and S. J. Parke, Phys. Rev. D **53**, 4886 (1996) [arXiv:hep-ph/9512264]; D. Atwood, A. Aeppli and A. Soni, Phys. Rev. Lett. **69**, 2754 (1992); D. Atwood, S. Bar-Shalom, G. Eilam and A. Soni,

Phys. Rept. **347**, 1 (2001) [arXiv:hep-ph/0006032]; M. Arai, N. Okada, K. Smolek and V. Simak, Phys. Rev. D **70**, 115015 (2004) [arXiv:hep-ph/0409273]; C. Csaki, J. Heinonen and M. Perelstein, JHEP **0710**, 107 (2007) [arXiv:0707.0014 [hep-ph]]; M. M. Nojiri and M. Takeuchi, arXiv:0802.4142 [hep-ph].

[85] T. Sjostrand, S. Mrenna and P. Skands, JHEP **0605**, 026 (2006) [arXiv:hep-ph/0603175].

[86] G. P. Salam and G. Soyez, JHEP **0705**, 086 (2007) [arXiv:0704.0292 [hep-ph]].

[87] J.E. Huth *et al.*, *Proceedings of Research Directions For The Decade: Snowmass Accord 1990.*

[88] J. Pumplin, A. Belyaev, J. Huston, D. Stump and W. K. Tung, JHEP **0602**, 032 (2006) [arXiv:hep-ph/0512167]; J. Campbell and R. K. Ellis, "MCFM, A Monte Carlo for FeMtobarn processes at Hadron Colliders, http://mcfm.fnal.gov."

[89] J. Alwall *et al.*, Eur. Phys. J. C **53**, 473 (2008) [arXiv:0706.2569 [hep-ph]].

[90] M. L. Mangano, M. Moretti, F. Piccinini, R. Pittau and A. D. Polosa, JHEP **0307**, 001 (2003) [arXiv:hep-ph/0206293].

[91] S. Catani, F. Krauss, R. Kuhn and B. R. Webber, JHEP **0111**, 063 (2001) [arXiv:hep-ph/0109231].

[92] S. D. Ellis, J. Huston, K. Hatakeyama, P. Loch and M. Tonnesmann, Prog. Part. Nucl. Phys. **60**, 484 (2008) [arXiv:0712.2447 [hep-ph]]; A. Banfi, G. P. Salam and G. Zanderighi, JHEP **0707**, 026 (2007) [arXiv:0704.2999 [hep-ph]].

[93] G. Sterman, arXiv:hep-ph/0412013; I. M. Dremin, AIP Conf. Proc. **828**, 30 (2006) [arXiv:hep-ph/0510250]; T. Han, arXiv:hep-ph/0508097; G. Sterman, arXiv:hep-ph/9606312.

[94] P. Meade and L. Randall, arXiv:0708.3017 [hep-ph].

[95] A. Czarnecki and K. Melnikov, Nucl. Phys. B **544**, 520 (1999) [arXiv:hep-ph/9806244].

[96] K. G. Chetyrkin, R. Harlander, T. Seidensticker and M. Steinhauser, Phys. Rev. D **60**, 114015 (1999) [arXiv:hep-ph/9906273].

[97] C. Amsler *et al.* [Particle Data Group], Phys. Lett. B **667** (2008) 1, `http://www-pdg.lbl.gov/2008/reviews/statrpp.pdf`.

[98] M. Strassler, "Unusual Physics Signatures at the LHC," talk presented at the 2007 Phenomenology Symposium - Pheno 07, University of Wisconsin, Madison, May 7-9, 2007.

[99] L. Randall and R. Sundrum, Phys. Rev. Lett. **83**, 3370 (1999) [arXiv:hep-ph/9905221].

[100] M. Furman, Nucl. Phys. B **197**, 413 (1982).

[101] F. Aversa, P. Chiappetta, M. Greco and J. P. Guillet, Nucl. Phys. B **327**, 105 (1989), Z. Phys. C **46**, 253 (1990).

[102] N. Kidonakis and J. F. Owens, Phys. Rev. D **63**, 054019 (2001) [arXiv:hep-ph/0007268].

[103] A. Sen, Phys. Rev. D **24**, 3281 (1981).

[104] A. Sen, Phys. Rev. D **28**, 860 (1983); J. Botts and G. Sterman, Nucl. Phys. **B325**, 62 (1989).

[105] M. Derrick *et al.* [ZEUS Collaboration], Phys. Lett. B **369**, 55 (1996) [arXiv:hep-ex/9510012].

[106] S. Chekanov *et al.* [ZEUS Collaboration], arXiv:hep-ex/0612008.

[107] C. Adloff *et al.* [H1 Collaboration], Eur. Phys. J. C **24**, 517 (2002) [arXiv:hep-ex/0203011].

[108] S. Abachi *et al.* [D0 Collaboration], Phys. Rev. Lett. **76**, 734 (1996) [arXiv:hep-ex/9509013]; F. Abe *et al.* [CDF Collaboration], Phys. Rev. Lett. **80**, 1156 (1998); F. Abe *et al.* [CDF Collaboration], Phys. Rev. Lett. **74**, 855 (1995).

[109] J. D. Bjorken, Phys. Rev. D **47**, 101 (1993).

[110] G. Oderda and G. Sterman, Phys. Rev. Lett. **81**, 3591 (1998) [arXiv:hep-ph/9806530].

[111] R. B. Appleby and M. H. Seymour, JHEP **0309**, 056 (2003) [arXiv:hep-ph/0308086].

[112] A. Kyrieleis and M. H. Seymour, JHEP **0601**, 085 (2006) [arXiv:hep-ph/0510089].

[113] M. Sjodahl, JHEP **0812**, 083 (2008) [arXiv:0807.0555 [hep-ph]].

[114] M. Sjodahl, arXiv:0906.1121 [hep-ph].

[115] M. Dasgupta and G. P. Salam, Phys. Lett. B **512**, 323 (2001) [arXiv:hep-ph/0104277].

[116] M. Dasgupta and G. P. Salam, JHEP **0203**, 017 (2002) [arXiv:hep-ph/0203009].

[117] J. R. Forshaw, A. Kyrieleis and M. H. Seymour, JHEP **0608**, 059 (2006) [arXiv:hep-ph/0604094].

[118] J. R. Forshaw, A. Kyrieleis and M. H. Seymour, JHEP **0809**, 128 (2008) [arXiv:0808.1269 [hep-ph]].

[119] J. Keates and M. H. Seymour, JHEP **0904**, 040 (2009) [arXiv:0902.0477 [hep-ph]].

[120] R. B. Appleby and M. H. Seymour, JHEP **0212**, 063 (2002) [arXiv:hep-ph/0211426].

[121] J. Forshaw, J. Keates and S. Marzani, JHEP **0907**, 023 (2009) [arXiv:0905.1350 [hep-ph]].

[122] J. R. Forshaw and M. Sjodahl, JHEP **0709**, 119 (2007) [arXiv:0705.1504 [hep-ph]].

[123] A. Kulesza and L. Motyka, Phys. Rev. Lett. **102**, 111802 (2009) [arXiv:0807.2405 [hep-ph]].

[124] A. Kulesza and L. Motyka, arXiv:0905.4749 [hep-ph].

[125] B. Lillie, L. Randall and L. T. Wang, JHEP **0709**, 074 (2007) [arXiv:hep-ph/0701166].

[126] K. Agashe, H. Davoudiasl, G. Perez and A. Soni, Phys. Rev. D **76**, 036006 (2007) [arXiv:hep-ph/0701186].

[127] B. Lillie, J. Shu and T. M. P. Tait, Phys. Rev. D **76**, 115016 (2007) [arXiv:0706.3960 [hep-ph]].

[128] K. Agashe, S. Gopalakrishna, T. Han, G. Y. Huang and A. Soni, arXiv:0810.1497 [hep-ph].

[129] H. Davoudiasl, S. Gopalakrishna and A. Soni, arXiv:0908.1131 [hep-ph].

[130] S. Godfrey and T. A. W. Martin, Phys. Rev. Lett. **101**, 151803 (2008) [arXiv:0807.1080 [hep-ph]].

[131] P. Fileviez Perez, R. Gavin, T. McElmurry and F. Petriello, Phys. Rev. D **78**, 115017 (2008) [arXiv:0809.2106 [hep-ph]].

[132] S. D. Ellis, C. K. Vermilion and J. R. Walsh, arXiv:0903.5081 [hep-ph].

[133] L. T. Wang and I. Yavin, Int. J. Mod. Phys. A **23**, 4647 (2008) [arXiv:0802.2726 [hep-ph]].

[134] N. Arkani-Hamed, S. Dimopoulos and G. R. Dvali, Phys. Lett. B **429**, 263 (1998) [arXiv:hep-ph/9803315].

[135] L. Randall and R. Sundrum, Phys. Rev. Lett. **83**, 3370 (1999) [arXiv:hep-ph/9905221].

[136] D. Dicus, A. Stange and S. Willenbrock, Phys. Lett. B **333**, 126 (1994) [arXiv:hep-ph/9404359].

[137] W. Bernreuther, M. Flesch and P. Haberl, Phys. Rev. D **58**, 114031 (1998) [arXiv:hep-ph/9709284].

[138] D. Choudhury, R. M. Godbole, R. K. Singh and K. Wagh, Phys. Lett. B **657**, 69 (2007) [arXiv:0705.1499 [hep-ph]].

[139] N. Kidonakis and G. Sterman, Phys. Lett. B **387**, 867 (1996).

[140] N. Kidonakis and G. Sterman, Nucl. Phys. B **505**, 321 (1997) [arXiv:hep-ph/9705234]; N. Kidonakis, G. Oderda and G. Sterman, Nucl. Phys. **B531** (1998) 365 [hep-ph/9803241].

[141] N. Kidonakis, A. S. Vera and P. Stephens, arXiv:0802.4240 [hep-ph]; N. Kidonakis and P. Stephens, arXiv:0805.1193 [hep-ph]; N. Kidonakis, arXiv:0903.2561 [hep-ph].

[142] T. Becher and M. Neubert, Phys. Rev. D **79**, 125004 (2009) [arXiv:0904.1021 [hep-ph]].

[143] M. Beneke, P. Falgari and C. Schwinn, arXiv:0907.1443 [hep-ph].

[144] M. Czakon, A. Mitov and G. Sterman, arXiv:0907.1790 [hep-ph].

[145] A. Ferroglia, M. Neubert, B. D. Pecjak and L. L. Yang, arXiv:0907.4791 [hep-ph].

[146] Y. L. Dokshitzer, V. A. Khoze and S. I. Troian, Adv. Ser. Direct. High Energy Phys. **5**, 241 (1988).

[147] Y. L. Dokshitzer, V. A. Khoze, A. H. Mueller and S. I. Troian, *Gif-sur-Yvette, France: Ed. Frontieres (1991) 274 p. (Basics of).*

[148] R. K. Ellis, W. J. Stirling and B. R. Webber, Camb. Monogr. Part. Phys. Nucl. Phys. Cosmol. **8**, 1 (1996).

[149] A. Banfi, G. P. Salam and G. Zanderighi, JHEP **0408**, 062 (2004) [arXiv:hep-ph/0407287].

[150] G. Sterman, arXiv:hep-ph/0501270.

[151] C. F. Berger, Mod. Phys. Lett. A **20**, 1187 (2005) [arXiv:hep-ph/0505037].

[152] A. Djouadi, G. Moreau and R. K. Singh, Nucl. Phys. B **797**, 1 (2008) [arXiv:0706.4191 [hep-ph]].

[153] R. M. Harris, C. T. Hill and S. J. Parke, arXiv:hep-ph/9911288.

[154] N. Arkani-Hamed, A. G. Cohen, E. Katz and A. E. Nelson, JHEP **0207**, 034 (2002) [arXiv:hep-ph/0206021].

[155] M. Schmaltz and D. Tucker-Smith, Ann. Rev. Nucl. Part. Sci. **55**, 229 (2005) [arXiv:hep-ph/0502182].

[156] J. Boersma, Phys. Rev. D **74**, 115008 (2006) [arXiv:hep-ph/0608239].

[157] J. Boersma and A. Whitbeck, Phys. Rev. D **77**, 055012 (2008) [arXiv:0710.4874 [hep-ph]].

[158] R. S. Pasechnik, A. Szczurek and O. V. Teryaev, arXiv:0901.4187 [hep-ph].

[159] K. Hagiwara, Q. Li and K. Mawatari, JHEP **0907**, 101 (2009) [arXiv:0905.4314 [hep-ph]].

[160] L. D. Landau, Dokl. Akad. Nawk., USSR **60**, 207 (1948); C. N. Yang, Phys. Rev. **77**, 242 (1950).

[161] M. Perelstein and A. Spray, arXiv:0907.3496 [hep-ph].

[162] A. Djouadi, Phys. Rept. **459**, 1 (2008) [arXiv:hep-ph/0503173].

[163] K. Cheung and W. Y. Keung, Phys. Rev. D **71**, 015015 (2005) [arXiv:hep-ph/0408335].

[164] P. Nason, S. Dawson and R. K. Ellis, Nucl. Phys. B **303**, 607 (1988); W. Beenakker, H. Kuijf, W. L. van Neerven and J. Smith, Phys. Rev. D **40**, 54 (1989); M. Czakon and A. Mitov, arXiv:0811.4119 [hep-ph].

[165] N. Kidonakis, Int. J. Mod. Phys. A **15**, 1245 (2000) [arXiv:hep-ph/9902484].

[166] L. F. Alday and R. Roiban, Phys. Rept. **468**, 153 (2008) [arXiv:0807.1889 [hep-th]].

[167] A. Mitov and S. Moch, JHEP **0705**, 001 (2007) [arXiv:hep-ph/0612149]. T. Becher and K. Melnikov, JHEP **0706**, 084 (2007) [arXiv:0704.3582 [hep-ph]].

[168] R. A. Brandt, F. Neri and M. a. Sato, Phys. Rev. D **24**, 879 (1981).

[169] Yu. L. Dokshitzer and G. Marchesini, JHEP **0601**, 007 (2006) [arXiv:hep-ph/0509078]; M. Sjodahl, JHEP **0812**, 083 (2008) [arXiv:0807.0555 [hep-ph]]; M. H. Seymour and M. Sjodahl, JHEP **0812**, 066 (2008) [arXiv:0810.5756 [hep-ph]].

[170] G. P. Korchemsky and A. V. Radyushkin, Sov. J. Nucl. Phys. **44**, 877 (1986) [Yad. Fiz. **44**, 1351 (1986)]; G. P. Korchemsky and A. V. Radyushkin, Phys. Lett. B **171**, 459 (1986).

[171] J. C. Collins and D. E. Soper, Nucl. Phys. B **193**, 381 (1981) [Err.-ibid. B **213**, 545 (1983)].

[172] L. Magnea and G. Sterman, Phys. Rev. **D42**, 4222 (1990).

[173] This observation has also been made by E. Gardi, using a similar representation in x-space. We thank E. Gardi for this private communication.

[174] We observe that the relations $s = -t$ or $s = -u$ do not correspond to equal invariants in the sense above.

[175] G. Sterman, in *AIP Conference Proceedings Tallahassee, Perturbative Quantum Chromodynamics*, eds. D. W. Duke, J. F. Owens, New York, 1981, p. 22; J. G. M. Gatheral, Phys. Lett. **B133**, 90 (1983); J. Frenkel and J. C. Taylor, Nucl. Phys. **B246**, 231 (1984); C. F. Berger, hep-ph/0305076.

[176] R. Bonciani, S. Catani, M. L. Mangano and P. Nason, Nucl. Phys. B **529**, 424 (1998) [Erratum-ibid. B **803**, 234 (2008)] [arXiv:hep-ph/9801375]; M. Cacciari, S. Frixione, M. L. Mangano, P. Nason and G. Ridolfi, JHEP **0809**, 127 (2008) [arXiv:0804.2800 [hep-ph]]; S. Moch and P. Uwer, Phys. Rev. D **78** (2008) 034003 [arXiv:0804.1476 [hep-ph]]; M. Czakon and A. Mitov, arXiv:0812.0353 [hep-ph]; N. Kidonakis and R. Vogt, Phys. Rev. D **78** (2008) 074005 [arXiv:0805.3844 [hep-ph]].

[177] T. Becher and M. Neubert, arXiv:0901.0722 [hep-ph], arXiv:0903.1126 [hep-ph]; E. Gardi and L. Magnea, arXiv:0901.1091 [hep-ph];